

POLITECNICO DI TORINO

Department of Structural, Geotechnical and Building
Engineering

Master's degree in Civil Engineering

Final Dissertation

Dynamic response of energy dissipation devices based on bistable components



**Politecnico
di Torino**

Supervisor:

Prof. Rosario CERAVOLO

Candidate:

Pasquale CASSESE 303662

Internship Tutor:

Dr. Amadeo BENAVENT CLIMENT

Dr. Nicola TARQUE

ACADEMIC YEAR 2024 – 2025

Ai miei genitori, perchè hanno creduto in me sin dal primo giorno.

A Marianna, perché ha saputo rendere speciali questi anni.

A me stesso, per l'ambizione che mi ha sempre contraddistinto.

"Per aspera ad astra"

Abstract

In recent years, there has been a growing interest in the development and implementation of energy dissipation devices for seismic protection. These devices play a crucial role in enhancing the seismic performance of structural systems by mitigating the damaging effects of seismic excitation. This investigation presents a comprehensive numerical study on the dynamic response of energy dissipation devices based on bistable components.

The aim of this study is to investigate to which extent the performance of the structural systems can be improved by installing energy dissipation devices that are able to switch between two stable equilibrium states under dynamic loads. This switch between the two stable positions occurs at very large velocities and this can increase the amount of energy dissipated by viscous damping. This would reduce the amount of energy that the building must dissipate through plastic deformations, and thus, the damage of the main structure. This eventually will extend the nominal life and improve the overall resilience of the structure.

First, a numerical model of the energy dissipation device with bistable elements is developed with OpenSees and the interface program STKO, that allowed performing advanced non-linear dynamic simulations. By changing a series of parameters (stiffness ratios, geometric properties and material characteristics, the so-called system/design parameters), various parametric simulations were performed. The expected goal is to demonstrate the efficiency of this bistable device in dissipating seismic energy, leading to a reduction in vibration amplitudes and peak stress levels in the structure under examination. Initially, the bistable device was studied, and once the parameters that will make the latter work better have been found, they are fixed and the device is duplicated and mirrored, resulting in a tristable device. Then it is inserted into the frame portal as a diagonal element.

In conclusion, the investigation aims to demonstrate that energy dissipation devices, based on bistable components, can improve their seismic response by providing controlled energy absorption and dissipation during earthquake events. These devices are not only suitable for new constructions, but they also represent a valid solution for retrofitting existing structures, by increasing their seismic resilience and safety. Future investigations could lead to an improvement of current models, enabling the realization of more efficient devices that further enhance the resilience and nominal life of structures in seismic zones.

Contents

List of Tables	8
List of Figures	9
1 Introduction	15
1.1 Thesis structure	16
1.2 General objective	16
1.3 Specific objective	18
1.3.1 Development of a numerical model representing a bistable brace subjected to dynamic motions	19
1.3.2 Study of the parameters' influence (θ_0, k)	20
1.3.3 Development of a tristable brace	24
1.3.4 Study of the frame response with seismic loadings	27
2 State of the art in Bistability and Seismic applications	30
2.1 Bistability	30
2.1.1 Examples of Bistable structure in Dynamics	31
2.1.2 Bistable Dynamics study in Engineering Applications	34
2.1.3 Fundamental concepts	44
2.1.4 Snap-Through Instability in Metamaterials	47
2.1.5 Bistable Auxetic Metamaterials	51
2.1.6 Advanced Modelling Techniques	52
2.1.7 Challenges in implementation	52
2.2 Applications to Control structural models with seismic loading	52
2.2.1 Studies and applications	53
2.3 Future directions	58
2.4 Conclusion	58

3	Study of the bistable element	59
3.1	Development of the numerical model with OpenSees	60
3.2	Parametric analysis	67
3.2.1	$\theta_0 = 30^\circ$	69
3.2.2	$\theta_0 = 45^\circ$	89
3.2.3	$\theta_0 = 65^\circ$	109
3.2.4	$\theta_0 = 55^\circ$	129
3.2.5	$\theta_0 = 37.5^\circ$	134
3.3	Conclusions	139
4	Study of a steel frame with a tristable brace	140
4.1	Development of the numerical model with OpenSees	141
4.2	Selection and scaling of GROUNG MOTION	143
4.3	Time-history analysis and response	143
4.4	Conclusions	146
5	Conclusions	148
	Bibliography	150

List of Tables

3.1	Summary table of object properties	61
3.2	Summary of Parameter Combinations	67
3.3	Summary of Parameter Combinations	67
3.4	Summary of Parameter Combinations	67
3.5	Summary of Parameter Combinations	68
3.6	Summary of Parameter Combinations	68

List of Figures

1.1	Examples of bistable structural units, and their comprehensive analysis approach [1]	17
1.2	Bistable axial bar element: θ is the inclination angle of the rigid hinged bars in a state of equilibrium for the external load F ; u is the horizontal displacement of the middle slider, v is the vertical displacement of the flappers; L_b is length of the hinged bars; k_s is axial stiffness of the encapsulated spring; distances L_1 and L_2 and bending rigidity (EI) of the flappers determine its bending stiffness, $k_b = 12EI[(3L_1 + L_2)/L_1^3 \cdot (3L_1 + 4L_2)]$; and θ_0 is initial of angle of the hinged bars, prior to loading [1]	20
1.3	Three response types of the bistable axial bar element of Figure 1.2, realized at varying stiffness ratio k (left) and at varying initial angle θ_0 (right): bistable superplastic (SP), bistable superelastic (SE) and monostable (MS) responses. The dash lines represent unstable equilibrium solutions [1]	23
1.4	Composite bar structure, metabrace, comprised of two bistable elements of Figure 1.2 type, where initial angles of the hinged bars at zero load are θ_0 and $\pi - \theta_0$, respectively. Other design parameters are identical in two elements and the total structure potential, (Equation 1.7), is still defined by two design parameters $\{k, \theta_0\}$. All springs and elastic flappers are relaxed at zero load in the State 1 [1]	25
1.5	Sample tristable response (superelastic type) of Figure 1.4 metabrace at $k = 0.12$ and $\theta_0 = 45^\circ$. Here, k and f are given in Equation 1.5, and $x_{tot} = x_1 + x_2$, where x_1 and x_2 are from Eqs. (12 - 13) [1]	26

1.6	Examples of arrangement of multistable metabraces in the diagonal, chevron and X-type frames [1]	27
1.7	Illustration of the approach for critical forces (F_c) determination, based on the overall frame geometry and allowed superelastic displacement (u_{se}) [1]	29
2.1	Schematic of a bistable system composed of spring, mass and frame [10]	31
2.2	Dependence of (a) spring force and (b) stored potential energy on the displacement position of the inertial mass [10]	32
2.3	Stiffened model with piezoelectric sensors and actuators [11]	34
2.4	Example of composites with negative stiffness. Linearised spring-damper model for exploring the stability and frequency response of extreme high damping due to negative spring constant [13]	35
2.5	Example of composites with negative stiffness (a)Viscoelastic spring system with negative stiffness components embedded when compressional preload is assigned in the bc and bd elements (b) lattice structure assembled with the building block shown in (a) with only the ab element being viscoelastic [13]	36
2.6	Schematics of different mechanisms to achieve negative compressibility [14]	37
2.7	Three-dimensional polymer microstructures [15]	38
2.8	Energy absorption in an elastic beam [16]	39
2.9	Bistable mechanism of double curved beams which can snap between two stable configurations, under a vertical force applied in the middle [3]	40
2.10	Biholar sheet [17]	41
2.11	(a) Main mechanisms of the unit cell and design parameter. (b) 2-D concept of the reversible energy absorbing metallic unit cell consisting of the spring and snap-fit mechanism. (c) Fabrication model of the unit cell and metamaterial assembly [19]	42
2.12	Mechanical model of pedestrian-bridge interactions [20]	46
2.13	Bistable snap-through dynamics for energy harvesting [10]	47
2.14	Classification, functionalities, and potential applications of snapping mechanical metamaterials [21]	48

2.15	Beam-based structures. (a) Schematic diagram of the pre-curved beam model under central load exhibiting snap-through instability. (b and c) Force-displacement curves and energy landscapes for the typical pre-curved beam model with bistable and monostable behaviours. (d) Reusable truss-based microlattices with snap-through instability. (e) Inclined beam-based metamaterials with tailorable shear behaviour. (f) Double-strip metamaterials with a high load-bearing capacity. (g) Snap-through structures with the pre-displacement constraint [21]	49
2.16	Shell-based structures. (a) 3D pixel metamaterials with straw-like shells. (b) Multistable dome shell arrays. (c) Multistable perforated shellular metamaterials. (d) Mono-curvature cylindrical surface structure. (e) Double-curvature cylindrical surface structure. (f) Corrugated sheet with mechanical memory effect. (g) Soft-matter balloon with snap-through instability [21]	49
2.17	Origami and kirigami. (a) Bistable Miura-origami unit cell. (b) Bistable waterbomb origami unit cell. (c) Bistable Kresling origami unit cell. (d) Multi-stable stacked-origami chain. (e) Curved-crease origami unit cell. (f) Kirigami unit cell with rotating square motifs. (g) Multistable kirigami sheet with rotating triangular motifs [21]	50
2.18	Other innovative structures. (a) Multi-compatible mechanism-based structures. (b) Ring-based structures with easy snap-folding. (c) Programmable metafluids with shell buckling. (d) Biholar sheet metamaterials with transverse confinement. (e) Granular metamaterials with multistability. (f) Multi-stable metamaterials utilizing the magnet interaction. (g) Bistable tensegrity metamaterials. (h) Snap-fit metamaterials [21]	50
2.19	Bistable auxetic metamaterials (BAM). (a) A “V” shaped bistable structure. (b) Force-displacement curve. (c) Strain energy-displacement curve. (d) Schematic diagrams of the star bistability structure (SBS). (e) The re-entrant structure (RES). (f) The bistable re-entrant structure (BRES). (g) (SBS). (h) (RES). (I) (BRES) [22]	51
2.20	Quasi-zero stiffness (QZS) element. (a) Mass-spring representation. (b) Force-deformation relationships [23]	54

2.21	Two degree-of-freedom base-isolation scheme. (a) The ground vibration x is filtered by means of the RLRB non-linear damping force, and the non-linear elastic term. (b) Lumped element scheme. (c) RLRB close-up showing the rolling contact between the rigid rollers of radius R and the viscoelastic rubber layer of thickness [24]	55
2.22	Experimental setup for controlling structural models by the use of AMD [26]	57
3.1	Bistable axial bar element: θ is inclination angle of the rigid hinged bars in a state of equilibrium for the external load F ; u is horizontal displacement if the middle slider, v is vertical displacement of the flappers; L_b is length of the hinged bars; k_s is axial stiffness of the encapsulated spring; distances L_1 and L_2 and bending rigidity (EI) of the flappers determine its bending stiffness, $k_b = 12EI[(3L_1 + L_2)/L_1^3 \cdot (3L_1 + 4L_2)]$; and θ_0 is initial of angle of the hinged bars, prior to loading [1]	61
3.2	Geometry of the model	62
3.3	Boundary conditions of the model	62
3.4	List of boundary conditions of the model	63
3.5	Properties of the model	63
3.6	List of properties	64
3.7	Mesh	64
3.8	Time Series	65
3.9	Analysis	65
3.10	Displacement at $t = 0$	66
3.11	Displacement at $t(u_{max})$	66
3.12	Simulation 1: $k=0.12$	69
3.13	Simulation 1: $k=0.12$	70
3.14	Simulation 1: $k=0.12$	71
3.15	Simulation 1: $k=0.12$	72
3.16	Simulation 1: $k=0.10$	73
3.17	Simulation 1: $k=0.10$	74
3.18	Simulation 1: $k=0.10$	75
3.19	Simulation 1: $k=0.10$	76
3.20	Simulation 1: $k=0.32$	77
3.21	Simulation 1: $k=0.32$	78
3.22	Simulation 1: $k=0.32$	79
3.23	Simulation 1: $k=0.32$	80

3.24	Simulation 1: $k=0.02$	81
3.25	Simulation 1: $k=0.02$	82
3.26	Simulation 1: $k=0.02$	83
3.27	Simulation 1: $k=0.02$	84
3.28	Simulation 1: $k=0.22$	85
3.29	Simulation 1: $k=0.22$	86
3.30	Simulation 1: $k=0.22$	87
3.31	Simulation 1: $k=0.22$	88
3.32	Simulation 1: $k=0.12$	89
3.33	Simulation 1: $k=0.12$	90
3.34	Simulation 1: $k=0.12$	91
3.35	Simulation 1: $k=0.12$	92
3.36	Simulation 1: $k=0.10$	93
3.37	Simulation 1: $k=0.10$	94
3.38	Simulation 1: $k=0.10$	95
3.39	Simulation 1: $k=0.10$	96
3.40	Simulation 1: $k=0.32$	97
3.41	Simulation 1: $k=0.32$	98
3.42	Simulation 1: $k=0.32$	99
3.43	Simulation 1: $k=0.32$	100
3.44	Simulation 2: $k=0.02$	101
3.45	Simulation 2: $k=0.02$	102
3.46	Simulation 2: $k=0.02$	103
3.47	Simulation 2: $k=0.02$	104
3.48	Simulation 2: $k=0.22$	105
3.49	Simulation 2: $k=0.22$	106
3.50	Simulation 2: $k=0.22$	107
3.51	Simulation 2: $k=0.22$	108
3.52	Simulation 3: $k=0.12$	109
3.53	Simulation 3: $k=0.12$	110
3.54	Simulation 3: $k=0.12$	111
3.55	Simulation 3: $k=0.12$	112
3.56	Simulation 3: $k=0.10$	113
3.57	Simulation 3: $k=0.10$	114
3.58	Simulation 3: $k=0.10$	115
3.59	Simulation 3: $k=0.10$	116
3.60	Simulation 3: $k=0.32$	117
3.61	Simulation 3: $k=0.32$	118

3.62	Simulation 3: $k=0.32$	119
3.63	Simulation 3: $k=0.32$	120
3.64	Simulation 3: $k=0.02$	121
3.65	Simulation 3: $k=0.02$	122
3.66	Simulation 3: $k=0.02$	123
3.67	Simulation 3: $k=0.02$	124
3.68	Simulation 3: $k=0.22$	125
3.69	Simulation 3: $k=0.22$	126
3.70	Simulation 3: $k=0.22$	127
3.71	Simulation 3: $k=0.22$	128
3.72	Simulation 4: $k=0.12$	129
3.73	Simulation 4: $k=0.10$	130
3.74	Simulation 4: $k=0.32$	131
3.75	Simulation 4: $k=0.02$	132
3.76	Simulation 4: $k=0.22$	133
3.77	Simulation 5: $k=0.12$	134
3.78	Simulation 5: $k=0.10$	135
3.79	Simulation 5: $k=0.32$	136
3.80	Simulation 5: $k=0.02$	137
3.81	Simulation 5: $k=0.22$	138
4.1	Tristable element	141
4.2	Steel portal frame	142
4.3	Steel portal frame with the tristable brace element	142
4.4	Accelerogram from Calitri	143
4.5	Top nodes acceleration	144
4.7	Results	144
4.6	Top nodes displacement	145
4.8	Results	145
4.9	Top nodes acceleration without tristable brace	146
4.10	Top nodes displacement without tristable brace	146
4.11	Results	147

Chapter 1

Introduction

Over the years, seismic events have exposed various challenges not only in design but also in performance efficiency. In response, focus has been posed on updating and developing technical standards. More recently, however, attention has been given on other approaches, such as the development of innovative seismic isolation devices and energy dissipation systems designed to manage the energy generated by earthquakes. The main purpose of these systems is to absorb and dissipate the energy generated by earthquakes.

This research builds on the work of Karpov (*"On the comprehensive stability analysis of axially loaded bistable and tristable metastructures"*)[1]: approaches to the systematic analysis of intrinsically non-linear structures with multiple stable response, controlled buckling and snapping behaviour have recently attracted attention in the context of mechanical metamaterial design. Snapping bistable elements are often very efficient dampers and perform well at very low forcing frequencies. In this paper, the basic tools of metamaterial analysis are applied to macroscopic systems relevant to civil and mechanical engineering applications. Such systems consist of several bistable elements.

Following the analysis of a single snapping bistable member, combinations of two members with asymmetric properties are considered to demonstrate the robust tristable performance of the resulting structure in low-frequency or quasi-static tensile-compression loading cycles. The resulting symmetrical overall response to tension and compression has potential applications in mechanical and large-scale seismic structures.

1.1 Thesis structure

This work has been organised in following chapters:

- **Chapter 1** → this chapter introduces the motivation of this work;
- **Chapter 2** → this chapter provides an overview regarding the bistability and the applications to control structural models;
- **Chapter 3** → this chapter sets the rules for developing a bistable element with the use of OpenSees;
- **Chapter 4** → this chapter proceeds what has been accomplished in the previous chapter with the development of a tristable brace element in OpenSees;
- **Chapter 5** → this chapter presents a summary of the conclusions and considerations of the results obtained.

1.2 General objective

The greatest challenge for modern civil engineering is earthquakes, which have the potential to inflict severe damages on structures and endanger human lives. Energy-dissipative devices are the primary components of traditional seismic design strategies for absorbing and dissipating seismic energy. However, these conventional approaches often suffer from limitations such as cumulative damages, irreversible deformations and the need for extensive post-event repairs. Recent advancements in structural engineering have introduced an innovative alternative: the integration of bistable mechanisms into structural systems. This research investigates the possibilities of employing bistable mechanisms to control the response of structures subjected to earthquakes, with the aim of enhancing both energy dissipation and post-event resilience.

Bistable mechanisms are characterised by their ability to reside in two distinct stable equilibrium states under the same loading conditions. This property provides a unique combination of self-centering behaviour and efficient energy absorption. In contrast to traditional devices that primarily rely on yielding and plastic deformation, bistable elements can snap between the two stable configurations, thereby dissipating energy through controlled buckling

and rapid state transitions. The work of Karpov «On the comprehensive stability analysis of axially loaded bistable and tristable metastructures» [1] has set a robust theoretical foundation by developing a comprehensive stability analysis of axially loaded bistable and tristable metastructures. Their approach, which employs dimensionless potential energy formulations, response curves, bifurcation diagrams, and phase diagrams, offers valuable insights into how key design parameters - such as stiffness ratios and initial geometric configurations - govern the dynamic behaviour and critical load thresholds of these systems.

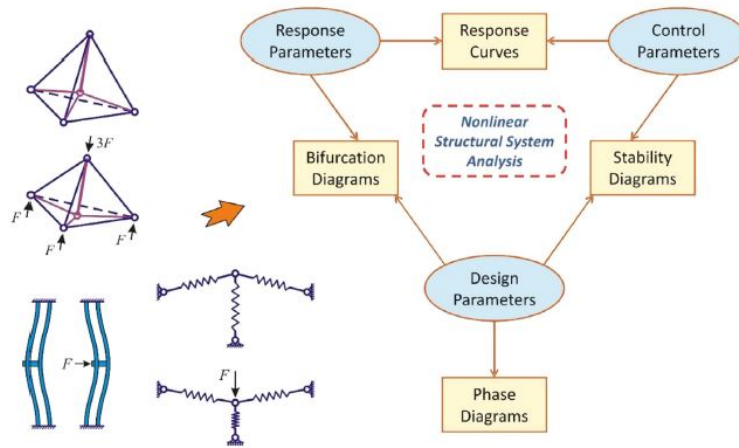


Figure 1.1: Examples of bistable structural units, and their comprehensive analysis approach [1]

The theoretical framework proposed by Karpov and co-authors begins with the formulation of the total potential energy of a bistable element, which is expressed in a dimensionless form to highlight the role of the **design parameters**. In the analysed system, a hinged bar element with elastic flappers and an encapsulated spring is used as a representative bistable unit. These two parameters determine which way this element's energy landscape changes: the **stiffness ratio** of the spring and the bending resistance of the flappers, as well as the **initial angle** of the hinged bars. By tuning these parameters, one can control the onset of non-linear responses such as snapping, controlled buckling, and even transitions to tristable behavior when combining antisymmetric pairs of elements. The detailed correlation between design parameters and system responses not only improves our comprehension of bistability in mechanical systems but also offers a direct

path for practical implementation in structural applications.

In the context of seismic design, the application of bistable mechanisms offers several significant advantages. In buildings, bracing systems that use buckling-restrained braces are meant to resist extreme loads and dissipate energy. However, these systems often suffer from issues related to premature fracture or irreversible deformations, which compromise their long-term performance.

Bistable elements, on the other hand, can provide symmetric hysteretic responses in both tension and compression. This symmetry is particularly beneficial in seismic events, where structures are subjected to complex cyclic loadings. By incorporating bistable or tristable elements into critical structural components, it is possible to achieve a controlled energy dissipation mechanism that minimizes damage and allows for rapid recovery following an earthquake. By combining two bistable elements with antisymmetric properties, Karpov et al. demonstrate the ability to achieve a testable system. A symmetric double-hysteresis loop is present in this system to efficiently dissipate energy in both loading directions, resulting in improved seismic resilience of the structure.

1.3 Specific objective

The primary objective of this work is to investigate the feasibility of integrating bistable mechanisms into structural systems as an innovative strategy for seismic control. The investigation will be structured around several important research questions:

- What are the effects of changes in stiffness ratio and initial geometry of bistable elements on critical loads and energy dissipation characteristics when subjected to seismic loading?
- What are the underlying mechanisms that govern the transition between different stability regimes (monostable, bistable, and tristable) in these systems?
- Lastly, how can these mechanisms be put into practice in the design of structures that are earthquake-resistant?

In order to address these questions, the research will adopt a multi-faceted

methodology that combines analytical modelling, numerical simulations, and experimental validation. The analytical component will build on the theoretical formulations developed by Karpov et al.[1], and extend the analysis to take into account realistic loading scenarios that represent seismic events. Advanced computational tools will be used to simulate the non-linear dynamic behaviour of structures equipped with bistable elements, allowing for a detailed assessment of performance under cyclic loads.

In addition to enhancing energy dissipation, the integration of bistable mechanisms is expected to contribute to the improved self-centering capabilities. The functionality and safety of a structure can be compromised by residual deformations following an earthquake in traditional seismic design. Bistable systems, which can return to a stable configuration when energy is lost, are a promising solution to this problem due to their inherent ability to return to a pre-defined stable configuration. By reducing the need for extensive post-event repairs, self-centering behaviour also contributes to the structure's overall resilience by maintaining its load-carrying capacity.

The potential impact of this research is significant. By developing a detailed understanding of the mechanics of bistable systems and their integration into structural designs, this study aims to provide a new paradigm in earthquake engineering. The outcomes may lead to the creation of innovative, cost-effective seismic protection systems that not only reduce damage during an earthquake but also guarantee fast recovery and continuity of structural functionality. In addition, the knowledge accumulated from this work has the potential to have broader applications beyond seismic applications, potentially influencing the design of other types of energy-dissipative systems in mechanical and civil engineering.

1.3.1 Development of a numerical model representing a bistable brace subjected to dynamic motions

In Karpov's work [1], various bistable unit cells have been discussed in the context of cyclic mechanical metamaterials (Danso and Karpov, 2016 [2]; Rafsanjani et al., 2015 [3]; Karpov et al., 2017 [4]; Klein and Karpov, 2017 [5]; Klein and Karpov, 2019 [6]). On the contrary, a bistable element to replace the usual bars, braces and other two-force members relevant to the structural engineering practice should have a slender beam-like design, as that in [Figure 1.2](#). Attention is therefore drawn to this element structure.

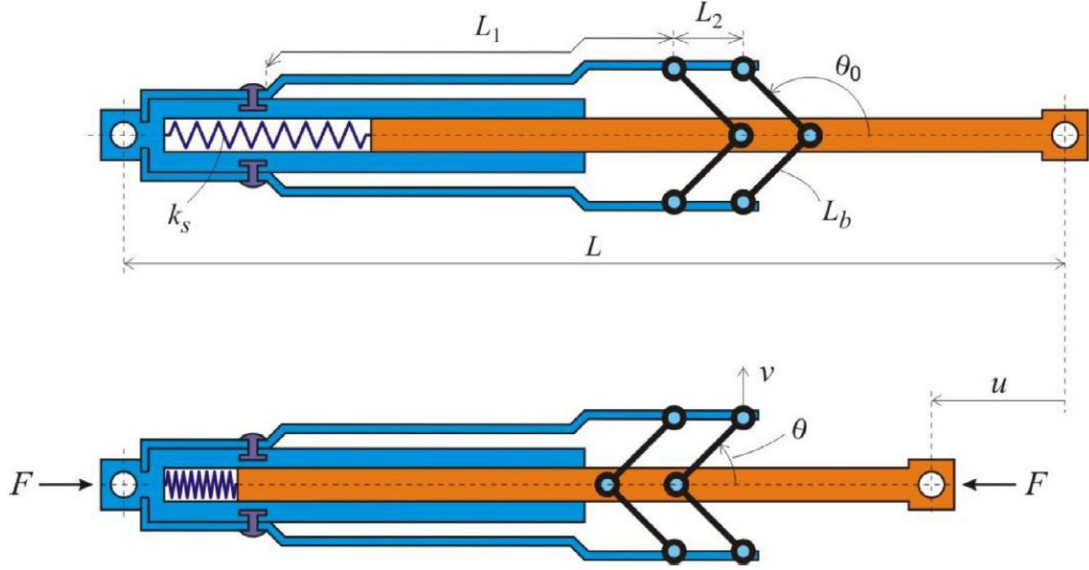


Figure 1.2: Bistable axial bar element: θ is the inclination angle of the rigid hinged bars in a state of equilibrium for the external load F ; u is the horizontal displacement if the middle slider, v is the vertical displacement of the flappers; L_b is length of the hinged bars; k_s is axial stiffness of the encapsulated spring; distances L_1 and L_2 and bending rigidity (EI) of the flappers determine its bending stiffness, $k_b = 12EI[(3L_1 + L_2)/L_1^3 \cdot (3L_1 + 4L_2)]$; and θ_0 is initial of angle of the hinged bars, prior to loading [1]

1.3.2 Study of the parameters' influence (θ_0 , k)

For a systematic discussion, Karpov used, in his work [1], the logic summarised in the diagram in Figure 1.1. Similar to metamaterials research (Danso and Karpov, 2016 [2]; Karpov et al., 2017 [4]; Klein and Karpov, 2017 [5]; Klein and Karpov, 2019 [6]), all relevant physical parameters are divided into three groups:

- (i) **system/design parameters** (describing the unit cell geometry and material properties of the basic structural element),
- (ii) **control parameters** (describing external stimuli such as mechanical or thermal loads),
- (iii) **state parameters** or **behaviour variables** (describing deformation or thermal stress states that change with and in response to

external loads).

The theoretical, numerical and experimental relationships between state and control parameters may exhibit interesting physical behaviour and properties such as double variability, negative elastic modulus, negative thermal expansion, etc. Also, a diagram that maps all possible types of physical behaviour with respect to the *design parameters* is called a **phase diagram**. A map that combines the critical values of important *design* and *control parameters* (e.g. values at the onset of a phase transition) is called a **stability diagram** (Strogatz, 1994 [7]). A plot of response versus design parameters at fixed control parameters is called a bifurcation diagram, and a map showing example responses to external stimuli for a given system parameter is called a response curve. The purpose of this comprehensive mapping is to provide a relationship between the desired interesting behaviour and the relevant system parameters that can be used in practical designs to make this behaviour possible. Such a systematic analysis can minimize or completely eliminate the trial-and-error effort that is, otherwise, inevitable in the design of non-linear structural systems.

Considering the [Figure 1.2](#), if the hinged bar and middle slider are rigid and the side flappers only deform when bending, the total potential energy function of the aforementioned bistable element is:

$$\Pi = \frac{1}{2}k_s u^2 + \frac{1}{2}k_b v^2 - Fu \quad (1.1)$$

$$u = L_b(\cos\theta_0 - \cos\theta), v = L_b(\sin\theta - \sin\theta_0) \quad (1.2)$$

where:

- θ is the inclination angle of the hinged bars in an equilibrium state of the element in response to F , the external load;
- θ_0 is the initial angle of the hinged bars, before loading;
- u is the horizontal displacement of the slider;
- v the vertical displacement of the flappers;
- L_b is the hinged bars' length;

- k_s is the axial stiffness of the spring;
- The bending stiffness of the flappers is:

$$k_b = 12EI \frac{(3L_1 + L_2)}{L_1^3 \cdot (3L_1 + 4L_2)} \quad (1.3)$$

It is important to highlight that, when $\theta = \theta_0$, k_s and k_b are relaxed.

By rescaling the potential energy (Equation 1.1) by the coefficient k_b , the dimensionless potential can be described by only four dimensionless parameters $\{\theta, f, k, \theta_0\}$:

$$U = U(\theta, f, k, \theta_0) = \frac{1}{2}kx^2 + \frac{1}{2}y^2 - fx \quad (1.4)$$

$$k = \frac{k_s}{k_b}, f = \frac{F}{k_b L_b}, x = \frac{u}{L_b} = \cos\theta_0 - \cos\theta, y = \frac{v}{L_b} = \sin\theta - \sin\theta_0 \quad (1.5)$$

Hence, the independent *design parameters* that can influence the mechanical response are two:

1. the ratio "k";
2. the initial angle " θ_0 ".

Considering Figure 1.1, there are also *control parameter(s)* and *state parameter(s)*, which are respectively "f" and " θ ".

The analysis of the response behaviour of these and similar non-linear systems is based on the first derivative of the total potential energy with respect to the *response parameters*.

$$\Phi_e(\theta, f, k, \theta_0) = \frac{\partial U}{\partial \theta} = (1 - k)\cos\theta + k\cos\theta_0 - \cot\theta\sin\theta_0 - f = 0 \quad (1.6)$$

The equilibrium set contains all equilibrium responses θ of the model (Equation 1.4) for a given external load f at a given set of *design parameters* k, θ_0 .

The solution for θ versus f from condition (Equation 1.6) can be performed numerically using methods outlined in, for example, Karpov et al. 2017 [4]; Klein and Karpov, 2017 [5]; Klein and Karpov, 2019 [6]; Strogatz, 1994 [7]), followed by equation (Equation 1.5) to calculate the corresponding equilibrium displacement x . Model (Equation 1.4) can qualitatively exhibit three different responses $x(f)$ depending on the *design parameters* k, θ_0 . The highly non-linear but monostable response is the first type. The bistable hysteretic response reversible to the initial configuration upon load removal, called superelastic bistability, is the second type. The third type is the non-reversible hysteresis requiring load reversal for returning to the original configuration; that is called superplastic bistability (Danso and Karpov, 2016 [2]; Karpov et al., 2017 [4]; Klein and Karpov, 2017 [5]; Klein and Karpov, 2019 [6]). Note that in a bivariate response, the structure has two different states, each with its own equilibrium angle against the same load. In more complex cases, the two states may exhibit different stiffnesses in addition to different equilibrium angles and displacements.

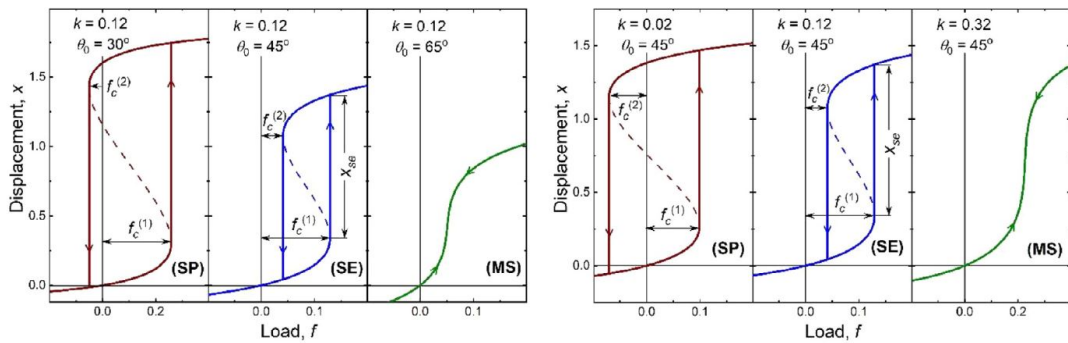


Figure 1.3: Three response types of the bistable axial bar element of Figure 1.2, realized at varying stiffness ratio k (left) and at varying initial angle θ_0 (right): bistable superplastic (SP), bistable superelastic (SE) and monostable (MS) responses. The dash lines represent unstable equilibrium solutions [1]

Interestingly, the bistable response curve in Figure 1.3 can also be seen as a bifurcation diagram where two saddle-node bifurcations are connected to each other. Therefore, the critical value of the external load at the onset of instability is an important characteristic of bistable structures that needs to be addressed in design. The response curves and bifurcation diagrams

in [Figure 1.3](#) clearly show that changes in the *system parameters* k, θ_0 can in principle lead to the desired bistable response. However, two important design questions are:

- How do the *system parameters* k, θ_0 affect the value of the critical force (f_c) at the beginning of the state transition of the structure?
- What is the acceptable range of *design parameters* k, θ_0 for the desired response type of the structure?

cannot be answered by equilibrium set analysis alone. A higher level analysis of the potential ([Equation 1.4](#)) is required to address the *design objectives* regarding the *critical force magnitude* and the *response type*.

1.3.3 Development of a tristable brace

As shown in [Figure 1.2](#) above, a thorough understanding of base bistable elements enables the design and property prediction of more complex structures composed of multiple bistable cells. It is interesting to consider a pair of antisymmetric elements all with identical properties (k, L_b), except that the initial angle of the hinged bar is θ_0 for the first element and $\pi - \theta_0$ for the second element. It is realistic to place these elements in a single telescopic rod structure, as shown in [Figure 1.4](#), where the elements are placed face to face in order to share a slider. Since the slider is not externally loaded, its displacement is an internal state parameter or internal variable of the structure. The total potential energy of the coupled structure can be written according to ([Equation 1.4](#)) as:

$$U_s(\theta_1, \theta_2, f, k, \theta_0) = \frac{1}{2}(x_1^2 + x_2^2) + \frac{1}{2}(y_1^2 + y_2^2) - f(x_1 + x_2) \quad (1.7)$$

$$x_1 = \cos\theta_0 - \cos\theta_1, y_1 = \sin\theta_1 - \sin\theta_0 \quad (1.8)$$

$$x_2 = \cos(\pi - \theta_0) - \cos\theta_2, y_2 = \sin\theta_2 - \sin(\pi - \theta_0) \quad (1.9)$$

where θ_1 and θ_2 are the inclination angles of the hinged bars in the two elements in the loaded state.

It is interesting to see the overall response of this structure to varying axial loads. The most interesting feature here is the value of the critical force at the onset of snapping. For this purpose, a numerical energy minimization method was applied to the potential (Equation 1.7) with $k = 0.12$ and different loads f varying gradually in a closed loop[1]. The solution of the previous step was the trial solution for the next value of the load. The result is an interesting symmetric double hysteresis shape as shown in Figure 1.5. This symmetry makes the structure practical for seismic applications where both tensile and compressive loads are equally expected.

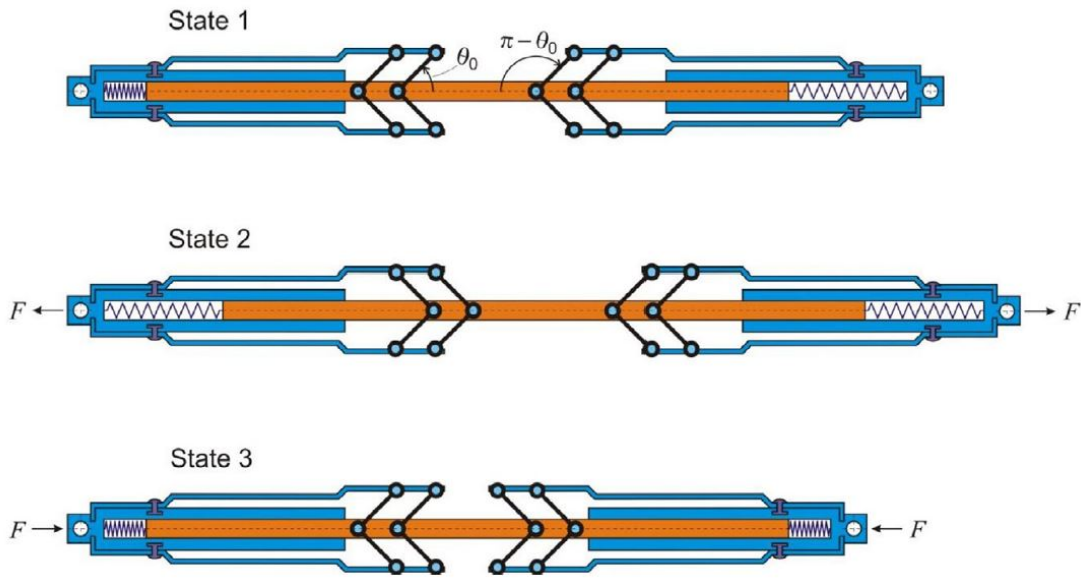


Figure 1.4: Composite bar structure, metabrace, comprised of two bistable elements of Figure 1.2 type, where initial angles of the hinged bars at zero load are θ_0 and $\pi - \theta_0$, respectively. Other design parameters are identical in two elements and the total structure potential, (Equation 1.7), is still defined by two design parameters $\{k, \theta_0\}$. All springs and elastic flappers are relaxed at zero load in the State 1 [1]

Karpov [1] noted that the *critical forces* were exactly the same as for Figure 1.2. In one cell $\theta_0 = 45^\circ$ and in the other $\theta_0 = 135^\circ$. In the first cell the critical forces are positive and represent superelasticity in tension; in the second element they are negative and represent superelasticity in compression. It can be also noted also that the area of the two hysteresis loops is the

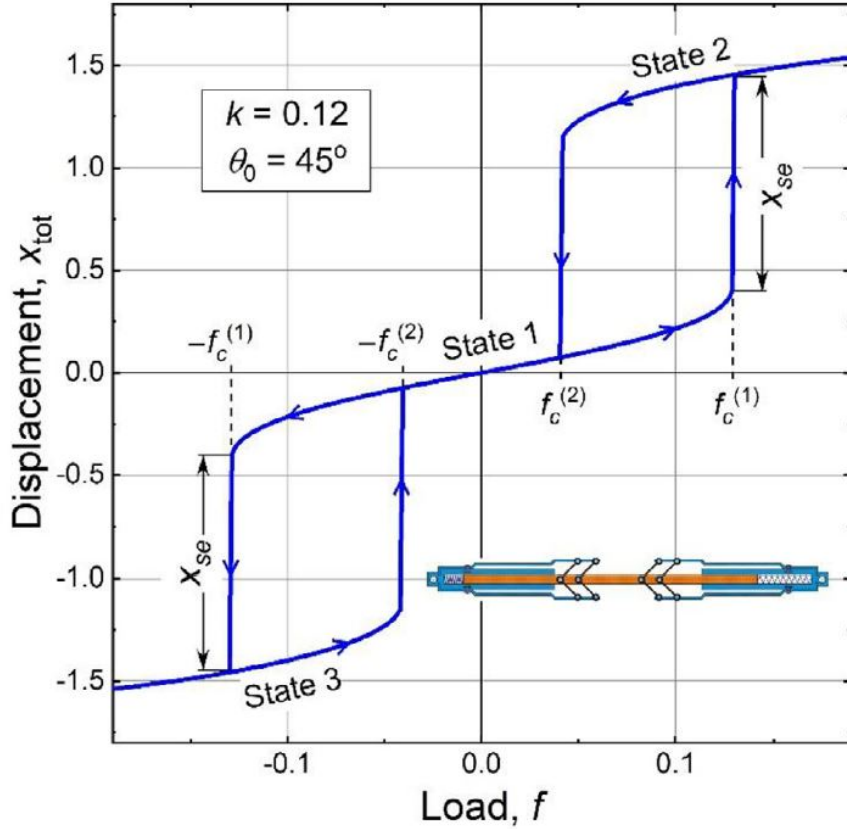


Figure 1.5: Sample tristable response (superelastic type) of Figure 1.4 metabrace at $k = 0.12$ and $\theta_0 = 45^\circ$. Here, k and f are given in Equation 1.5, and $x_{tot} = x_1 + x_2$, where x_1 and x_2 are from Eqs. (12 - 13) [1]

total work of the external forces dissipated by the structure. This energy can be directly related to another engineering metric in structural and mechanical engineering applications: seismic efficiency or damping efficiency of this axial element.

This composite structure has other important properties that make it suitable for various structural applications. In addition to the total axial elongation, the structure has an internal degree of freedom in the form of sliding displacement. The kinetic energy of external loads can be efficiently dissipated in this degree of freedom with very little viscous damping, potentially reducing acceleration in the external degrees of freedom and at the endpoints of the support. If the masses of the base (blue) and slider (orange) sections

of the meta-brace in Figure 1.2 and Equation 1.5 are denoted by M and m , the maximum acceleration and maximum velocity at both endpoints of a kinematic meta-brace are about M/m times lower than those at the right end of a two-point meta-brace during a cyclic axial load cycle. Another practical significance of this ternary structure is the relative simplicity of systematic stability analysis.

1.3.4 Study of the frame response with seismic loadings

As mentioned above, steel frames with concentrically braced diagonals can fail at the expense of diagonal braces, which can yield or buckle under extreme tension or compression during earthquakes (Wang et al., 2008 [8]). Karpov [1] proposed to replace the diagonal braces of concentric frames with hyperelastic biaxial and triaxial braces. He suggested replacing them with meta-braces of the type shown in Figure 1.2 and Figure 1.4[1]. An example of the meta brace arrangement is shown in Figure 1.6. One or two tristable elements can be used to provide diagonal or chevron support respectively; X-bracing support can be realised by two kinematic braces rotated at the midpoint of the slider. This can also be seen as an arrangement of two pairs of asymmetric bistable elements, see Figure 1.2, Figure 1.4 and Figure 1.6.

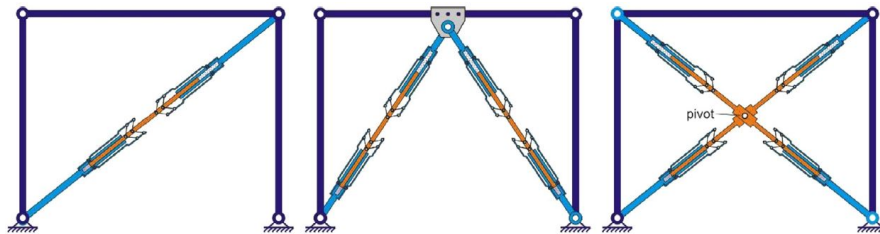


Figure 1.6: Examples of arrangement of multistable metabraces in the diagonal, chevron and X-type frames [1]

The non-linear structural system analysis discussed earlier can provide the *original dimensional parameters* $\{k_s, k_b, \theta_0, L_b, L\}$ for meta-brace fabrication, as shown in Figure 1.2 and Figure 1.4 and (Equation 1.1)-(Equation 1.5).

For this purpose, Karpov [1] highlighted some possibilities, for example:

- Select a value of L as the total relaxed length of the meta-brace to fit

the undeformed frame geometry (see [Figure 1.6](#));

- The initial angle θ_0 at which the desired (superelastic) response is obtained with a reasonable stiffness ratio k is chosen;
- The required boundary forces and superelastic displacements are then determined using an approach inspired by the capacitive design method (Saunders, 1980 [9]): a normal brace replaced by a meta-brace is normally expected to fail at some threshold force of the lateral load acting on the whole frame.

The axial force in such braces can be calculated at the onset of the expected failure of the frame. This force can be taken as the forward switching critical force $F_c^{(1)} = f_c^{(1)}k_bL_b$ of the meta-brace (see [Figure 1.7](#)). Given a new structural configuration based on certain typical rear structural loads and expected superelastic displacements of the frame, the backward switching critical force $F_c^{(2)} = f_c^{(2)}k_bL_b$ can also be obtained from standard structural analysis. Here $F_c^{(2)}$ must exceed the axial member forces in an equivalent normal frame with the same geometry as the new configuration of the frame determined by the superelastic displacement u_{se} (see [Figure 1.7](#)). The required superelastic displacement δ_{se} in the meta-brace corresponding to u_{se} is calculated using the kinematics of the given frame type calculated using the relationship

In conclusion, Karpov asserted [1] that it has been shown that tristability provides a symmetric overall response to tension and compression, which is of interest for large-scale structural applications and earthquake engineering. In conventional structural systems buckling is an undesirable instability or failure, but the elastic buckling behaviour of tristable brace elements can be considered as an advantage to increase energy dissipation capacity and reduce stresses. The stability analysis of tristable brace elements can be easily performed on the basis of bistable element analysis. In particular, it can be shown that the tristable bifurcation set is the sum of two bistable bifurcation sets with asymmetric properties. Thus, the comprehensive analysis of basic bistable mechanical elements proposed in Karpov work [1] paves the way for predicting the properties and design of more complex multi-stable structures of practical value. Although hyperelastic behaviour is probably of most practical interest, a superplastic regime (SP) with negative inverse switching forces may also be considered in the future for metaframes requiring simple a posteriori recovery treatment. The velocity-dependent damping

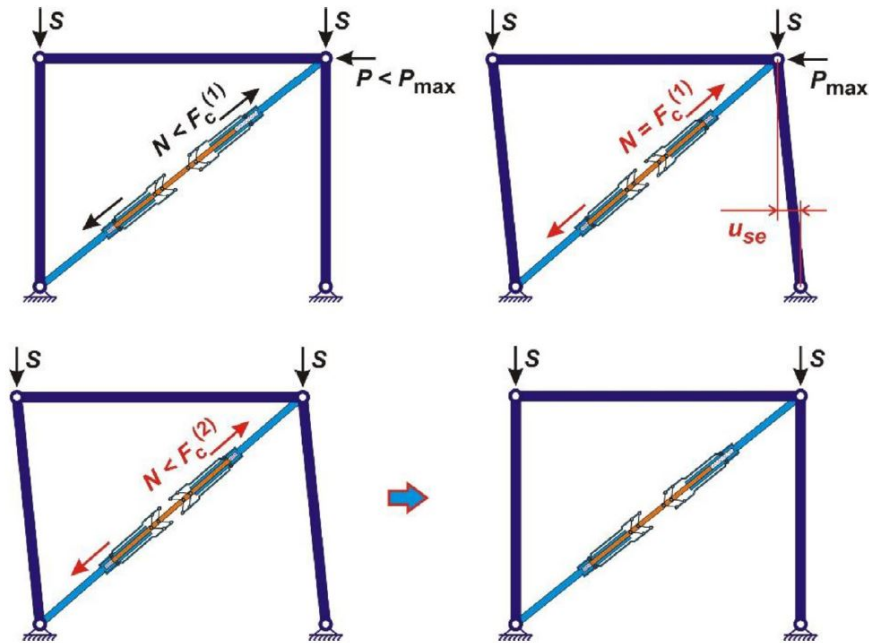


Figure 1.7: Illustration of the approach for critical forces (F_c) determination, based on the overall frame geometry and allowed superelastic displacement (u_{se}) [1]

behaviour is also of interest if the frequency of the external load reaches a significant fraction of the first mode frequency of the structure. In the design of telescopic snapper considered here and in Karpov's work [1], effective control of structural damping can be achieved by manipulating both friction and the rate of air escape through the structure.

Chapter 2

State of the art in Bistability and Seismic applications

2.1 Bistability

Bistability, which can be determined by the presence of two stable equilibrium states, is an innovative tool for structural dynamics and engineering. This property is widely observed in various mechanical, electrical, and biological systems. The bistability has been observed in natural systems, E.g., the Venusfly trap, an insectivorous plant which exhibits bistable behaviour in its trapping mechanism. The trap remains open and stable until an external stimulus, such as an insect's touch, triggers it to a closed and stable state. This example of natural bistability led researchers to explore similar mechanisms in artificial systems. Considering that the field of application is really wide, we will focus mostly on the domain of civil engineering.

The bistability concept has been broadly used in vibration control, energy harvesting and adaptive materials, and is now being considered for seismic application. In practice, the bistable systems present two stable equilibrium points separated by an unstable state. This configuration allows the system to switch between two stable states under certain conditions, often leading to unique dynamic behavior that can be used in engineering applications.

The efficient management of energy dissipation can be achieved through bistability, which has significant benefits for both new designs and retrofitted systems in seismic areas.

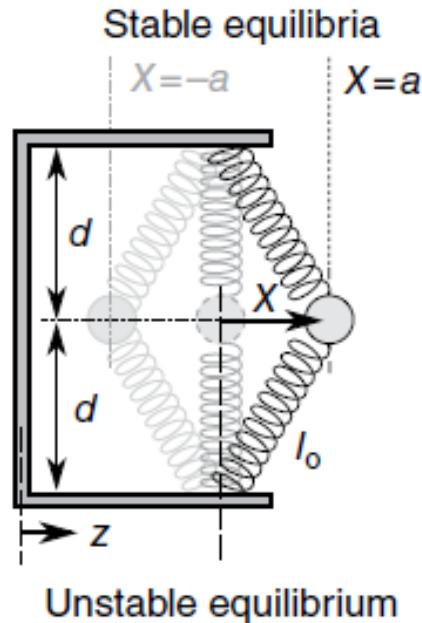


Figure 2.1: Schematic of a bistable system composed of spring, mass and frame [10]

Figure 2.1 provides a simple and clear visual of how a bistable system can be applied directly to vibration control and seismic damping systems.

2.1.1 Examples of Bistable structure in Dynamics

Bistable structures can have different designs, including mechanical springs, buckled beams and composite materials. An example is a mechanical system consisting of two identical springs connected to a mass. When the length of the undeformed spring exceeds half the span of the frame, the system is bistable [10], as we can see also in Figure 2.1. This system is characterised by a potential energy distribution with two local minima (stable state) and one local maximum (unstable state). The stable equilibrium of the structure is an arrangement of masses such that the displacement is $x = \pm a$.

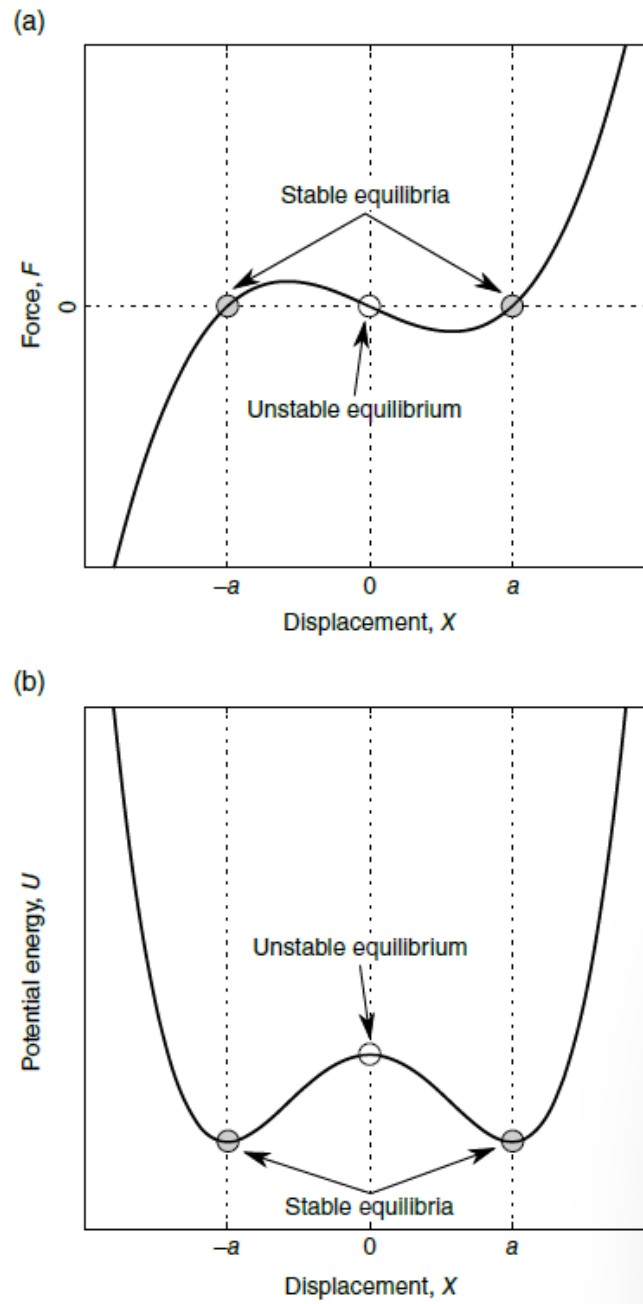


Figure 2.2: Dependence of (a) spring force and (b) stored potential energy on the displacement position of the inertial mass [10]

In Figure 2.2, it is possible to see the force $F(x)$ and the potential energy

$U(x)$ of a bistable system as functions of the mass displacement. The potential energy is determined by the following formula:

$$U = \int F dx \quad (2.1)$$

Figure 2.2 (a) shows that when the inertial mass is located in one of the equilibrium states, the total restoring force in the x direction is zero. On the other hand, Figure 2.2 (b) shows that at the unstable central configuration the inertial mass is zero, the potential energy is locally maximum, while at the neighbouring stable equilibrium, the potential energy of the system is locally minimum.

According to Hooke's law, the stiffness of a spring element is determined by spatial derivative of the restoring force dF/dx . Considering the total spring force profile at unstable equilibrium in Figure 2.2 (a), it is clear that a bistable spring has negative stiffness for this mass position. Unlike springs that resist mass motion in one direction, spring that exhibit negative stiffness across a range of displacements assist mass motion. As a result, small perturbations to an inertial mass placed in a full unstable equilibrium push the mass from a central position to one of the stable system configurations. In other word, when a perturbation is applied to a system in an unstable equilibrium state, the system transitions to one of the stable states. This is analogous to a ball rolling from the top of a hill and landing in one of two adjacent valleys. This behaviour is governed by the principle of potential energy minimization, where the system tries to minimize the sum of its potential energy [10].

The versatility of bistable systems is evident in their various applications. For example, bistable beams and plates are widely used in mechanical metamaterials to achieve a programmable mechanical response. These structures can be designed to exhibit specific bistable behaviours by tuning their geometry and material properties. Furthermore, bistable mechanisms are used in MEMS for applications such as switches, sensors and actuators where the ability to switch between stable states is a functional requirement.

One example is a composite plate to which a piezoelectric patch is attached, generating static stresses in the flattened plate configuration, and the plate maintains one of two stable equilibrium shapes with finite curvature.

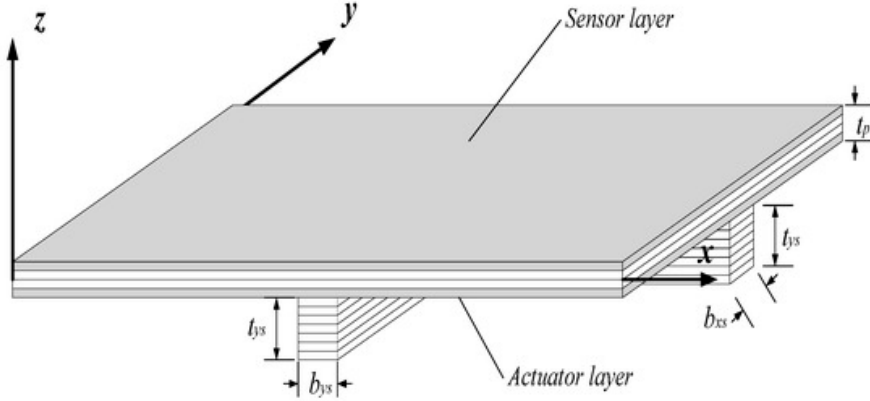


Figure 2.3: Stiffened model with piezoelectric sensors and actuators [11]

In the context of mechanical metamaterials, bistable elements can be arranged in periodic or non-periodic patterns to create materials with unique mechanical properties. For example, metamaterials composed of bistable unit cells can exhibit a negative Poisson's ratio. This auxetic behaviour is achieved by designing the unit cells to switch from one stable arrangement to another when compressed, resulting in lateral expansion [10].

2.1.2 Bistable Dynamics study in Engineering Applications

Bistable dynamics are used in various engineering applications due to their unique properties. For example, bistable systems are used in vibration control to achieve high damping capacity. The snap-through behaviour of bistable elements with large displacement transition between steady states results in large energy dissipation. This property is particularly useful in the design of damping materials and devices that can effectively damp vibrations over a wide frequency range [12].

Different researchers investigated snap through design in recent years. **Lake** has studied composites with negative stiffness that exhibit extreme mechanical damping and large stiffness [13]. The use of negative stiffness inclusions allows to overcome classical limits of the overall mechanical properties of composite materials. Two discrete viscoelastic 'spring' systems with negative stiffness are analysed to demonstrate the origin of the extreme properties and to analyse the stability and dynamics of the system: one model requires a geometrically non-linear analysis using preloading as a source of negative stiffness. Both models assume linearity of the material. Metastability is controlled by viscous elements. In the stable regime, extremely high mechanical damping can be achieved at low frequencies. In the metastable regime, a certain resonance-like response occurs. Prestressed viscoelastic systems are stable at the equilibrium point where the overall compliance is maximum and become metastable when the overall stiffness is set to a maximum. An inversion of the relationship between the magnitude and frequency of the complex modulus of elasticity is observed and the experimental observability of the singularity is discussed in relation to engineered composite materials and polycrystalline solids with metastable grain boundaries.

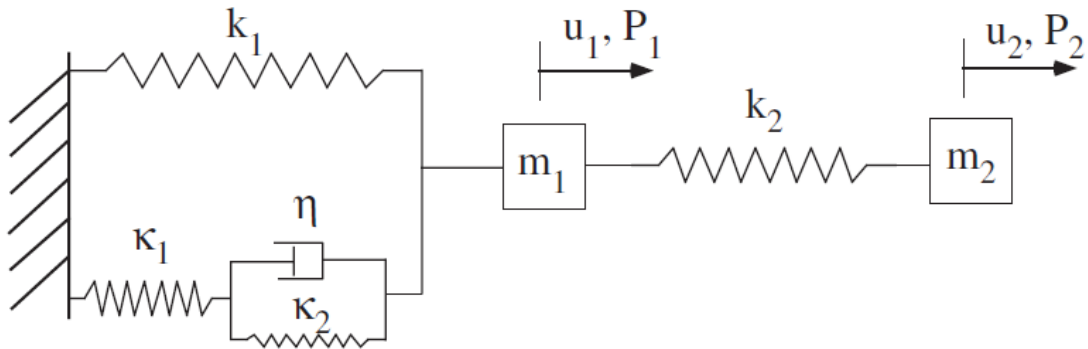
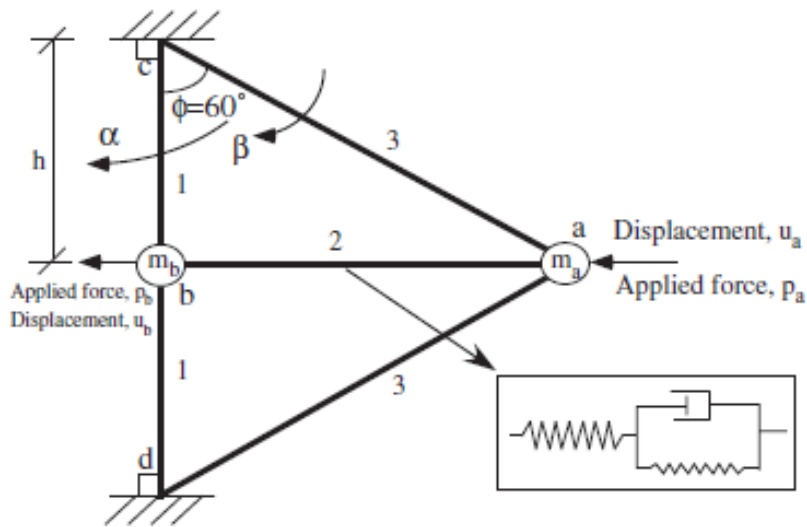
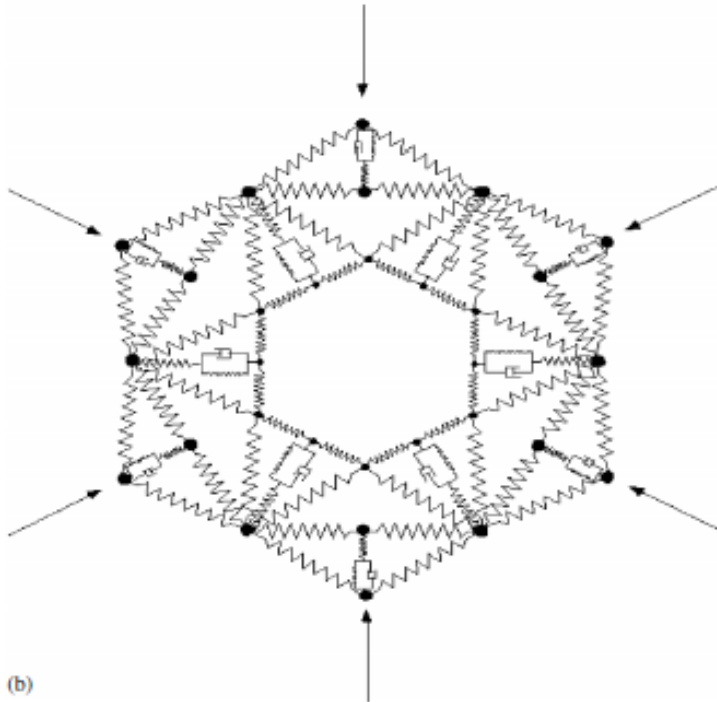


Figure 2.4: Example of composites with negative stiffness. Linearised spring-damper model for exploring the stability and frequency response of extreme high damping due to negative spring constant [13]



(a)



(b)

Figure 2.5: Example of composites with negative stiffness (a) Viscoelastic spring system with negative stiffness components embedded when compressional preload is assigned in the bc and bd elements (b) lattice structure assembled with the building block shown in (a) with only the ab element being viscoelastic [13]

Materials with negative compressibility transitions are realised on the basis of destabilisation, which is associated by **Motter** with a twisted hysteresis curve of the stress-strain relation [14].

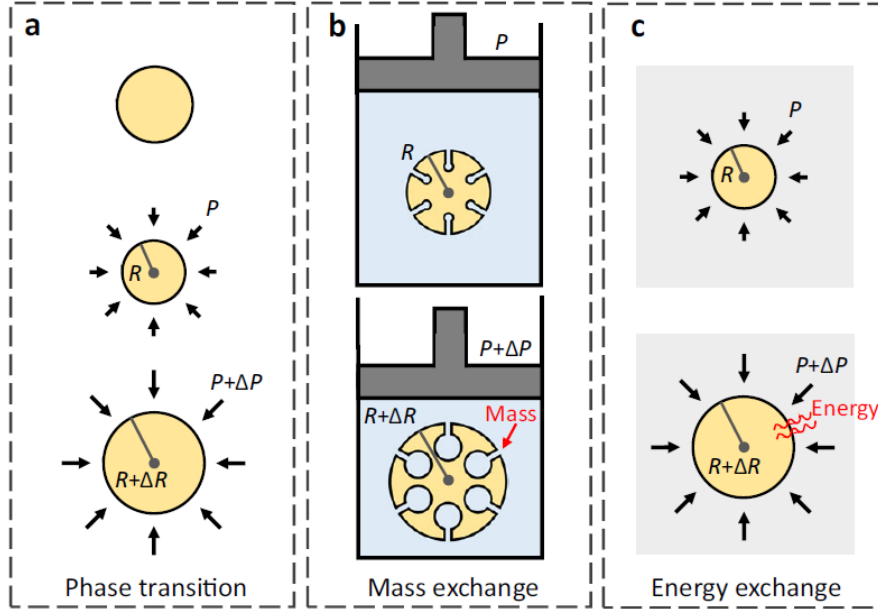


Figure 2.6: Schematics of different mechanisms to achieve negative compressibility [14]

In Figure 2.6, it is possible to see some examples about this work. In Figure 2.6 (a), the negative compressibility transition in a closed system is shown. The material radius initially decreases with increasing pressure, then, when the pressure exceeds a critical threshold, the radius suddenly increases and the material undergoes a negative compressibility transition. In Figure 2.6 (b), the negative compressibility induced by mass exchange in an open system is reported. As the piston is compressed, the hydrostatic pressure increases and the liquid (blue) penetrates further into the poroelastic material matrix (yellow). The different reactions throughout the matrix result in an increase in the effective volume of the material and negative compressibility. Finally, in Figure 2.6 (c), the negative compressibility induced by energy exchange in an open system can be observed. This energy is converted into mechanical work in the material, which expands in response to the applied pressure and becomes negatively compressible. In all panels,

R and P denote the radius and applied pressure respectively, while ΔR and ΔP show the corresponding increments.

Frenzel developed 3D polymer micro-lattices that presents self-recovering energy absorption structures based on tailored buckling elements [15]. Structures and materials that absorb mechanical impact energy typically employ either viscoelasticity or destructive modification. Based on a class of uniaxial, lightweight, geometrically non-linear mechanical micro-lattices, buckling of internal elements can be used to achieve a series of transitions allowing programmable behaviour followed by irreversible hysteric (repeatable) self-healing or multi-stability.

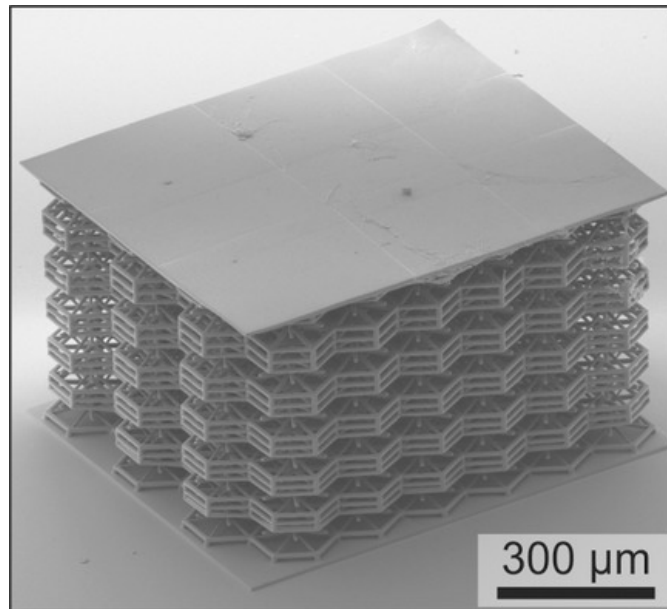


Figure 2.7: Three-dimensional polymer microstructures [15]

In [Figure 2.7](#), experiments on three-dimensional polymer microstructures are presented.

By combining 3D printing and computational methods, **Bertoldi** has designed a new class of architectural material that enables the controlled trapping of elastic energy [16]. These programmed structures contain beam elements with geometries specifically designed to allow large localised bistable deformations. When these materials are mechanically deformed, the beams are locally reconfigured to a higher energy, more stable deformation state, similar to phase transformation. The energy applied during deformation is stored in this way until a sufficient reverse force is applied to return the deformed beam to its original shape, whether through slow quasi-static loading or impact testing. The energy absorption mechanism is neither material-independent nor loading rate-independent, as it is solely due to the structural geometry of the compressed beam element.

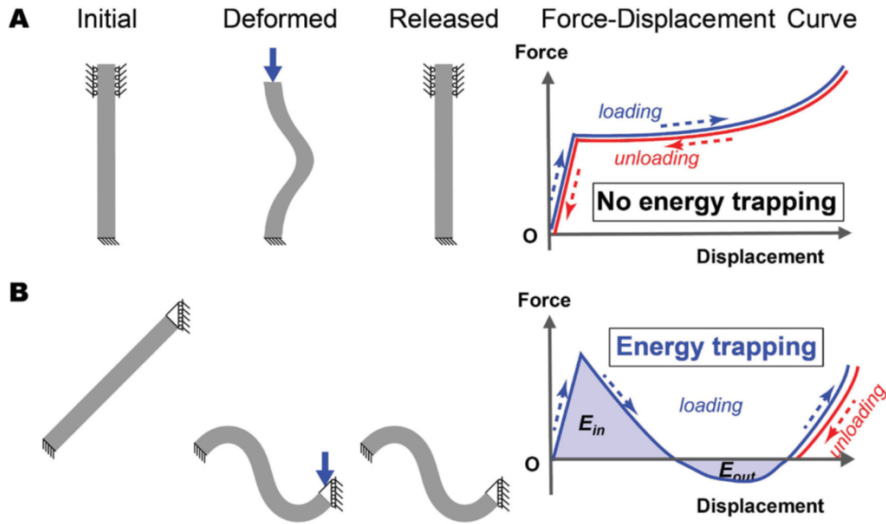


Figure 2.8: Energy absorption in an elastic beam [16]

Also **Pasini** proposed a mechanical metamaterial. This metamaterial exhibits a phenomenon of pattern switching between two different configurations by successive closure through instabilities [3]. When a normal force is applied to the centre of the double beam mechanism, the double beam mechanism enters a second steady state as it is possible to see in [Figure 2.9](#).

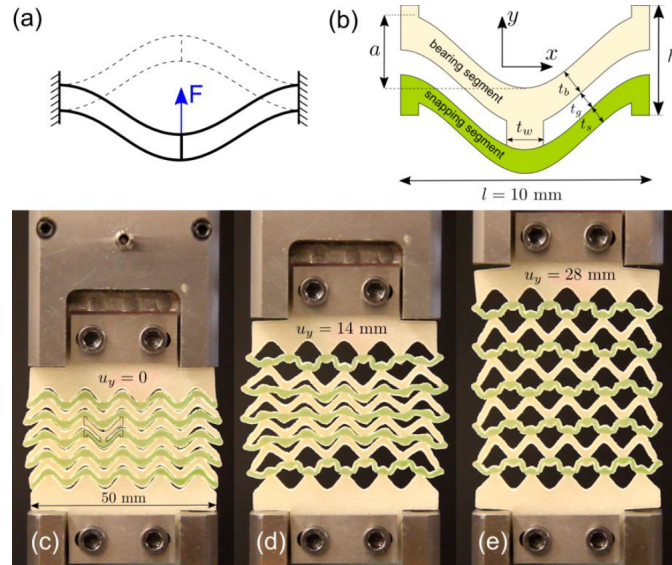


Figure 2.9: Bistable mechanism of double curved beams which can snap between two stable configurations, under a vertical force applied in the middle [3]

The clamped state at both ends is released to form a repeatable unit cell consisting of long segments with cosine connections at the two centres. When pulled along the axis of symmetry (y -axis), the lower segment bends at the critical tensile stress, transforming the pattern from a wavy structure to a rhombic structure. Depending on the amplitude of the curved segment, this transition can be smooth or discontinuous. Therefore, the amplitude of cosine-like curved segments can provide a means to tune the mechanical response of the system.

Florijn introduced a soft programmable model that exhibits monotonic, non-monotonic and hysteric behaviour under uniaxial compression with lateral constraints [17].

The main idea is illustrated in [Figure 2.10](#) by a two-hole sheet, which is a quasi-two-dimensional elastic sheet with a regular arrangement of holes of different sizes. Different hole sizes break one of the 90° rotational symmetries that exist when the hole sizes are equal. This causes differences in the polarization of the hole pattern depending on whether x or y compression is dominant.

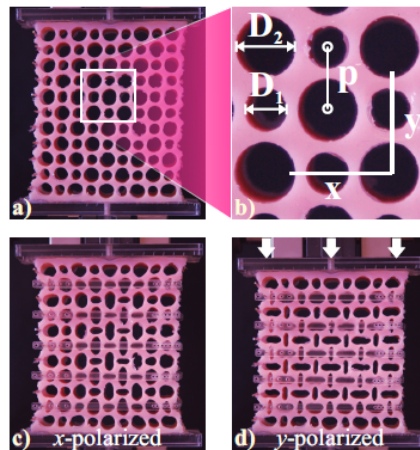


Figure 2.10: Biholar sheet [17]

Another example regards the cardiovascular stent. Based on a topology optimisation algorithm, James proposed a new design method for bistable cardiovascular stents such that a small triggering force can cause snap-through phenomenon [18].

Experimental studies confirm theoretical and numerical predictions of the bistable systems' behaviour. For example, cyclic compression tests on bistable unit cells have demonstrated their ability to transition between steady states and exhibit hysteric behaviour. These experiments (reported in [Figure 2.11](#)) are crucial for understanding the practical limits and performance of bistable systems in real applications [19].

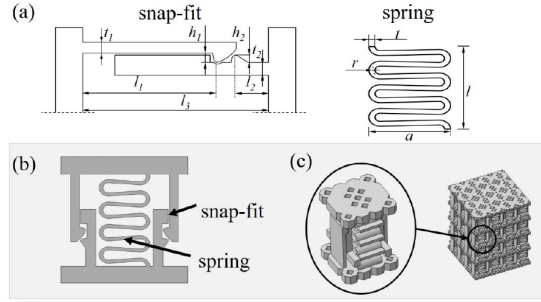


Figure 2.11: (a) Main mechanisms of the unit cell and design parameters. (b) 2-D concept of the reversible energy absorbing metallic unit cell consisting of the spring and snap-fit mechanism. (c) Fabrication model of the unit cell and metamaterial assembly [19]

Bistable structures have been successfully applied in various fields, including aerospace, civil engineering and robotics. In aerospace, bistable elements are used in adaptive structures to improve performance and reduce weight. For example, bistable composite materials can be designed to change shape in response to external stimuli, thereby improving the aerodynamics and fuel efficiency of aeroplanes.

In robotics, bistable mechanisms enable the design of soft robots with programmable and adaptive behaviour. These robots can navigate complex environments and perform tasks that require flexibility and adaptability [12][20].

Several case studies highlight the innovative use of bistable systems in advanced applications. One prominent example is the design of a metal-based mechanical metamaterial with tunable damping properties. This metamaterial consists of a unit cell that combines a spring mechanism and a snap mechanism to provide high energy dissipation and bistable behaviour. The unit cell was fabricated using additive moulding techniques such as laser powder bed melting then subjected to cyclic compression tests to evaluate its performance. The results show that metamaterials can achieve damping properties comparable to those of polymeric foams while maintaining the high environmental resistance of metals [19].

Another case study is the bistable gaits and wobbling caused by pedestrian-bridge interactions. In this study, the pedestrian-bridge interaction is analysed using an inverted pendulum model inspired by biomechanics. The results show that the interaction between the pedestrian and the bridge causes bidirectional lateral walking, which leads to large amplitude bridge wobbles. The study also investigates the role of stride length and pedestrian mass in the hysteric transitions between different types of wobble. These findings will shed light on the design of safer and more flexible pedestrian bridges [20].

Further research has explored the use of bistable elements in mechanical metamaterials to create complex pathways and continuous behaviours. By exploiting nonlinear instability and the multistability of two-state systems, researchers have developed metamaterials that can undergo controlled continuous deformation under cyclic loading. These materials can exhibit programmable behaviours such as shape changes and memory effects, making them suitable for applications in soft robotics and smart materials.

In energy harvesting, bistable systems are used to convert ambient vibration into electrical energy. The wide frequency bandwidth and high sensitivity of bistable energy harvesters make them suitable for capturing low-frequency vibrations that are difficult with conventional linear harvesters. Bistable energy harvesters can provide continuous or intermittent energy conversion depending on the excitation conditions using instantaneous dynamics [19]. For example, a bidirectional cantilever beam with piezoelectric patches can generate electrical energy when subjected to ambient vibration, providing an efficient solution for powering low-power electronic devices.

Bistable systems have also found applications in sensing and detection. The sensitivity of bistable sensors to external stimuli such as force, pressure and acceleration enables accurate detection of changes in the environment. Bistable sensors can be designed to exhibit a large output signal for small input changes, increasing their detection capability. Furthermore, the hysteric behaviour of bistable sensors provides a memory effect that is useful for monitoring and recording events over time.

As already said before, in civil engineering, bistable damping devices increase the resistance of buildings and bridges to dynamic loads such as earthquakes and wind. These devices can absorb and dissipate seismic energy and reduce

the risk of structural damage. For example, bidirectional dampers can be designed to fold from a steady state when subjected to seismic forces, thus dissipating energy and protecting structures from damage.

As far as civil engineering is concerned, the main fields of application are as follows:

- **Energy dissipation and structural damping** → Bistable devices, such as hysteric dampers, are engineered to dissipate vibrational energy under cyclic loading. Structural damage is minimized by these systems by engaging in controlled snapping transitions that effectively dissipate seismic energy over repeated cycles;
- **Seismic isolation** → Metafoundations incorporating bistable mechanisms offer improved seismic resilience. Building components are isolated by hybrid systems by redistributing seismic forces and enhancing energy absorption at critical points, which reduces stress on structural elements;
- **Adaptive metamaterials** → Snap-through curved beams or geometrically perturbed patterns are examples of mechanical metamaterials with bistable designs that display exceptional adaptability. These systems automatically adjust to varying seismic loads, ensuring structural stability even under extreme conditions;
- **Energy harvesting from seismic vibrations** → Sustainable building systems are aided by harvesters that use bistable dynamics to convert seismic energy into usable electrical power. These harvesters leverage the non-linear snapping behaviour to operate efficiently even under low-frequency vibrations.

2.1.3 Fundamental concepts

Bistable systems rely on an energy landscape characterised by potential wells separated by an energy barrier. The transition between stable states is triggered when external forces overcome this barrier. Such transitions enable adaptive responses, energy absorption and damping capabilities.

The foundational work (*Harnessing Bistable Structural Dynamics, 2017*) by **Harne** [10] focuses on how these principles can enhance vibration control and energy harvesting, highlighting their relevance to seismic applications.

Bistable systems achieve high performance through mechanical configurations (e.g., spring-mass models) and engineered metamaterials, tailored for specific operational needs.

Modelling of bistable systems involves both analytical and numerical approaches to predict their dynamic behaviour. The equations of motion of bistable systems are often nonlinear and their solution requires special techniques. For example, the equations of motion of a bistable system can be expressed in normalized form as follows:

$$\frac{d^2x}{d\tau^2} + \gamma \frac{dx}{d\tau} - x + \beta x^3 = p \cos \omega \tau \quad (2.2)$$

where $x(\tau)$ is the displacement, γ is the damping factor, β is a degree of non linearity, p is the excitation level and ω is the excitation frequency. The transient solution depends on the initial conditions of displacement and velocity:

- $x(0) = x_0$
- $\dot{x}(0) = \dot{x}_0$.

Numerical simulations complement analytical methods by providing detailed information about the response of the system under different conditions. These simulations help to identify critical parameters that affect the stability and performance of bistable systems and enable the design of optimized structures for specific applications. For example, finite element analysis (FEA) is widely used to simulate the behaviour of bistable structures under different loading conditions, providing valuable information on stress distribution, deformation patterns and energy dissipation.

Belykh showed mechanical model of pedestrian-bridge interactions [20]. The bridge is modelled as a platform of mass M with one side connected to a rigid support by elastic springs and dampers, x is the lateral position of the centre of gravity of the spring, y is the lateral vibration of the bridge and p is the lateral displacement of the footing centre of pressure.

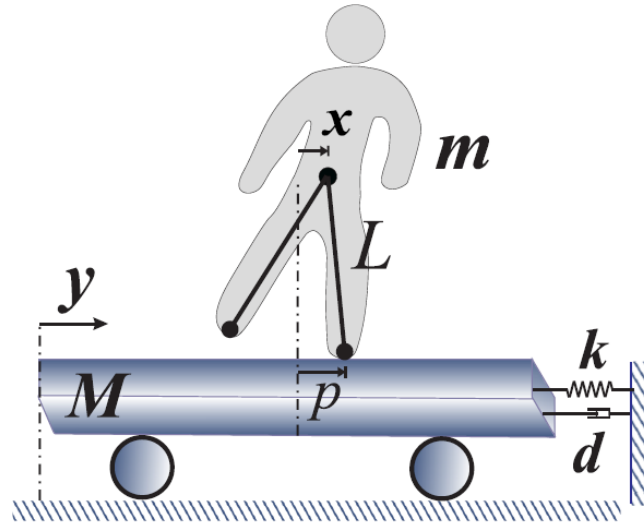


Figure 2.12: Mechanical model of pedestrian-bridge interactions [20]

Advanced modelling techniques have been developed to better understand and predict the behaviour of bistable systems. For example, multi-scale modelling approaches integrate the effects of material microstructure and macroscopic geometry to provide a comprehensive understanding of bivariate dynamics. These models capture the interactions between deformations at different scales and can predict the overall response of the system under various loading conditions.

Another advanced technique is the use of machine learning algorithms to optimise the design of bistable structures. By training machine learning models on datasets of bistable system behaviour, researchers can identify patterns and correlations not revealed by traditional modelling approaches. This enables the development of more efficient and effective bistable designs for specific applications.

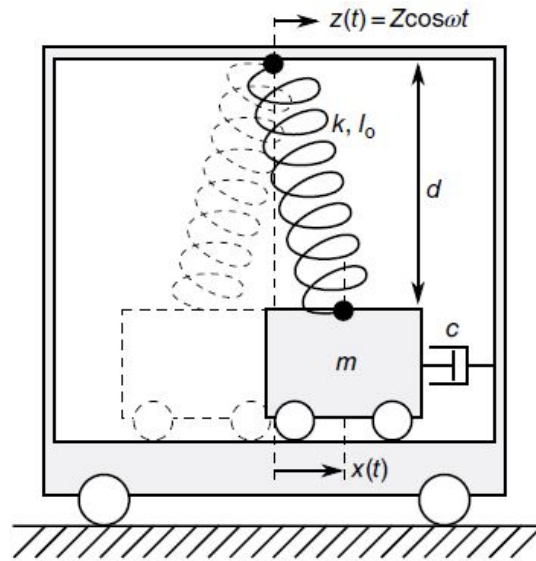


Figure 2.13: Bistable snap-through dynamics for energy harvesting [10]

This figure [Figure 2.13](#), showing the harvesting of bistable energy, can be referenced here as an example of how bistable systems adapt to dynamic forces, not only dissipating energy but converting it into usable power.

2.1.4 Snap-Through Instability in Metamaterials

Recent advances have introduced snap-through instability into the design of mechanical metamaterials, leading to the development of Snapping metamaterials. These materials exhibit rapid transitions between equilibrium states, enabling functions such as fast motion, energy modulation and bistable deformation. Snapping metamaterials have applications in robotics, sensing, energy absorption and shape reconstruction.

For example, Yan et al. [21] review design strategies and applications of snapping metamaterials, highlighting their potential to create mechanical intelligence and programmable behaviour.

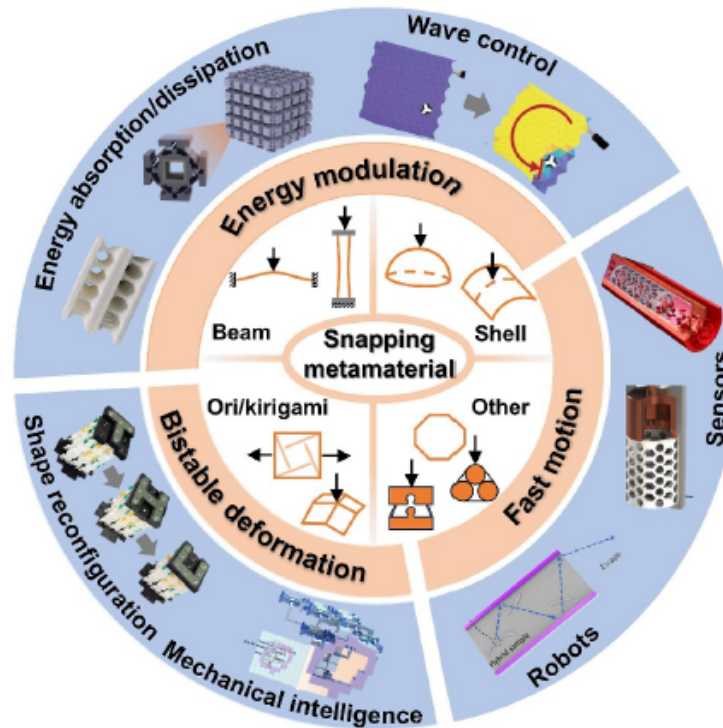


Figure 2.14: Classification, functionalities, and potential applications of snapping mechanical metamaterials [21]

As illustrated in [Figure 2.14](#), the possible typologies of snapping metamaterials are:

- Beam-based structures [Figure 2.15](#);
- Shell-based structures [Figure 2.16](#);
- Ori/Kirigami [Figure 2.17](#);
- Other innovative structures. [Figure 2.18](#);

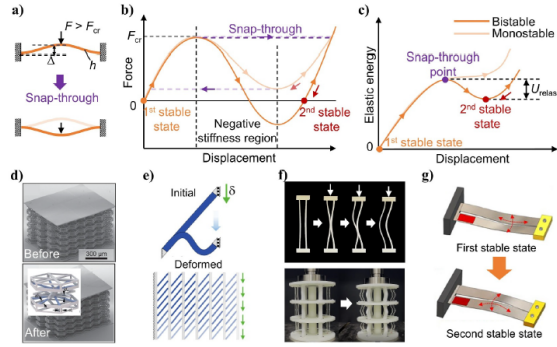


Figure 2.15: Beam-based structures. (a) Schematic diagram of the pre-curved beam model under central load exhibiting snap-through instability. (b and c) Force-displacement curves and energy landscapes for the typical pre-curved beam model with bistable and monostable behaviours. (d) Reusable truss-based microlattices with snap-through instability. (e) Inclined beam-based metamaterials with tailorable shear behaviour. (f) Double-strip metamaterials with a high load-bearing capacity. (g) Snap-through structures with the pre-displacement constraint [21]

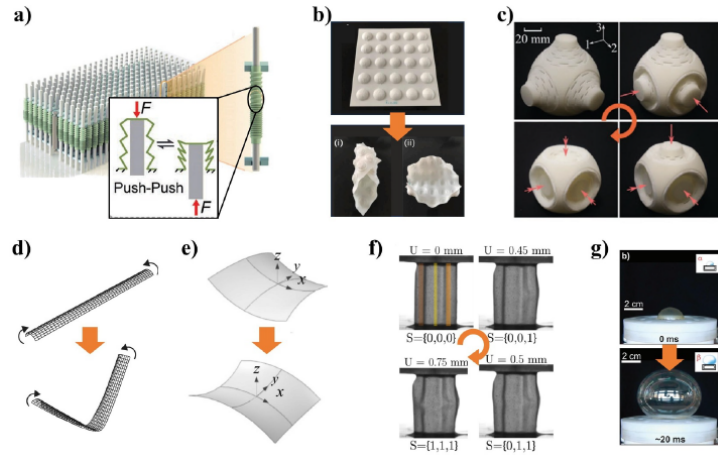


Figure 2.16: Shell-based structures. (a) 3D pixel metamaterials with straw-like shells. (b) Multistable dome shell arrays. (c) Multistable perforated shellular metamaterials. (d) Mono-curvature cylindrical surface structure. (e) Double-curvature cylindrical surface structure. (f) Corrugated sheet with mechanical memory effect. (g) Soft-matter balloon with snap-through instability [21]

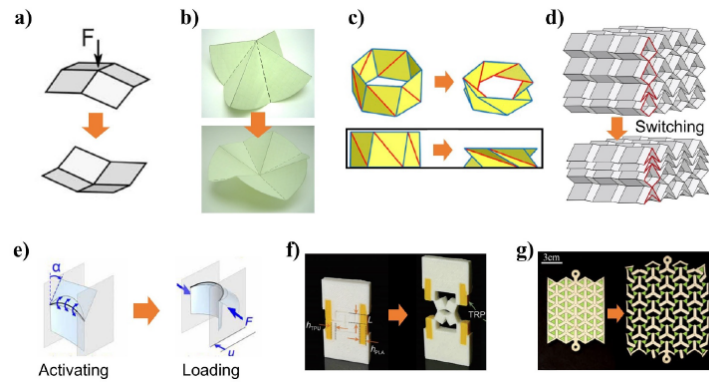


Figure 2.17: Origami and kirigami. (a) Bistable Miura-origami unit cell. (b) Bistable waterbomb origami unit cell. (c) Bistable Kresling origami unit cell. (d) Multi-stable stacked-origami chain. (e) Curved-crease origami unit cell. (f) Kirigami unit cell with rotating square motifs. (g) Multistable kirigami sheet with rotating triangular motifs [21]

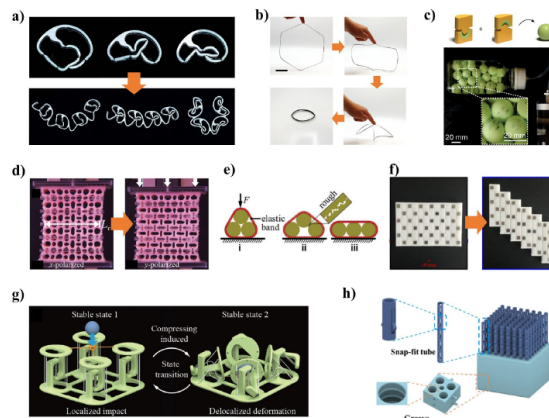


Figure 2.18: Other innovative structures. (a) Multi-compatible mechanism-based structures. (b) Ring-based structures with easy snap-folding. (c) Programmable metafluids with shell buckling. (d) Biholar sheet metamaterials with transverse confinement. (e) Granular metamaterials with multistability. (f) Multi-stable metamaterials utilizing the magnet interaction. (g) Bistable tensegrity metamaterials. (h) Snap-fit metamaterials [21]

2.1.5 Bistable Auxetic Metamaterials

Another innovative approach is the integration of bistable elements into auxiliary materials to realise bistable auxetic metamaterials (BAM). These materials combine negative Poisson’s ratio and structural bistability, allowing shape reconfiguration and geometric self-locking; Wang [22] proposed a novel 3D BAM that exhibits both bistable and auxetic behaviour. In this work, the programmable mechanical properties of BAM are demonstrated, making it suitable for applications in smart structures such as reconfigurable devices and deformable wings.

BAMs consist of a combination of bistable and auxetic elements that allow transitions between different steady states under specific loading conditions. Theoretical and numerical analyses provide insights into the deformation mechanisms and mechanical responses of BAMs and highlight their potential for advanced engineering applications. In Figure 2.19, examples of Bistable auxetic metamaterials can be seen.

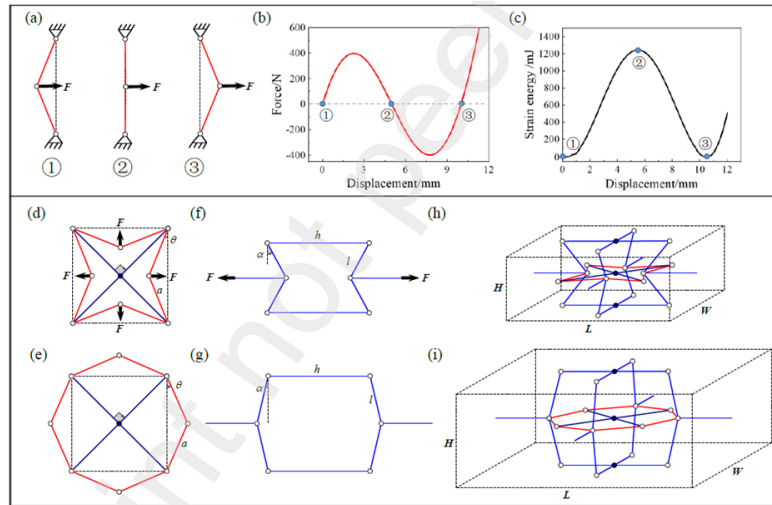


Figure 2.19: Bistable auxetic metamaterials (BAM). (a) A “V” shaped bistable structure. (b) Force-displacement curve. (c) Strain energy-displacement curve. (d) Schematic diagrams of the star bistability structure (SBS). (e) The re-entrant structure (RES). (f) The bistable re-entrant structure (BRES). (g) (SBS). (h) (RES). (I) (BRES) [22]

2.1.6 Advanced Modelling Techniques

Advanced modelling techniques have been developed to better understand and predict the behaviour of bistable systems. For example, multiscale modelling approaches integrate the effects of material microstructure and macroscopic geometry to provide a comprehensive understanding of bistable dynamics. These models capture the interactions between deformations at different scales and can predict the overall response of the system under various loading conditions.

Another advanced technique is the use of machine learning algorithms to optimise the design of bistable structures. By training machine learning models on datasets of bistable system behaviour, researchers can identify patterns and correlations not revealed by traditional modelling approaches. This enables the development of more efficient and effective bistable designs for specific applications.

2.1.7 Challenges in implementation

Despite the potential benefits, several challenges hinder the large-scale adoption of bistable systems. These include:

- **Material durability** → Long-term cycling loading may degrade bistable components, especially under extreme conditions;
- **Precision design** → Fine-tuning the energy barriers to balance responsiveness and stability is complex and application-specific;
- **Integration in large structures** → Scaling bistable devices for entire buildings requires advanced manufacturing techniques and careful alignment with structural loads.

2.2 Applications to Control structural models with seismic loading

Seismic isolation is an advanced engineering technique used in the construction of buildings and structures to reduce the effects of earthquakes and

other seismic activity. In this method, seismic isolation devices are strategically placed between the building's foundation and superstructure, effectively separating the structure from ground shaking. In this way, seismic isolation structures significantly reduce the energy transmitted to the building during an earthquake, increasing the seismic resistance and safety of the building.

2.2.1 Studies and applications

In the context of seismic isolation of small modular reactors (SMRs), Güner [23] studied the optimisation and performance of meta-foundations. In this work, a finite local resonance metafoundation with optimised resonator parameters is introduced to protect the reactor from strong earthquakes. The metafoundation has shown improved performance in both frequency and time domain, providing an effective solution for earthquake mitigation. The study emphasised the importance of optimising the dynamic properties of the resonator to achieve maximum performance. The proposed superstructure has been validated by experimental studies demonstrating its potential to improve the seismic resilience of reactors.

Two types of metafoundations are developed in this study: linear cells and quasi-zero stiffness (QZS) cells. Through a multivariate and multi-objective optimisation process, it is shown that these foundations significantly improve the seismic isolation performance compared to conventional seismic isolation solutions: The inclusion of QZS cells increases vertical flexibility, improves the energy dissipation capacity of the system and mitigates seismic shock.

The research team aimed at developing and evaluating metafoundations for seismic protection of NuScale type SMR buildings. The first type of superstructure, linear superstructure (LM), contains layers of locally resonant linear unit cells. The second type of superstructure, the QZS layered metafoundations (QM), contains single or multiple layers of QZS unit cells in addition to a layer of linear unit cells. Each QZS unit cell exhibits high static low dynamic stiffness in the vertical direction and is unstable with pre-compressed springs horizontally and vertical positive springs in parallel, as it is possible to see in [Figure 2.20](#).

In this study, the SMR is modeled using a low-fidelity model that includes the presence of internal fluid in the reactor pool. The metafoundation is designed to prevent damage in active seismic sites characterized by a safety

shutdown earthquake (SSE) level of 0.3 g. The optimisation of the resonator parameters of the upper foundation is performed using a sensitivity-based parameter grouping strategy and a hybrid grid search algorithm. The performance of the optimised metafoundation is evaluated by frequency and time-history analyses and the results are compared with rigid-based SMRs and conventional seismic isolation solutions.

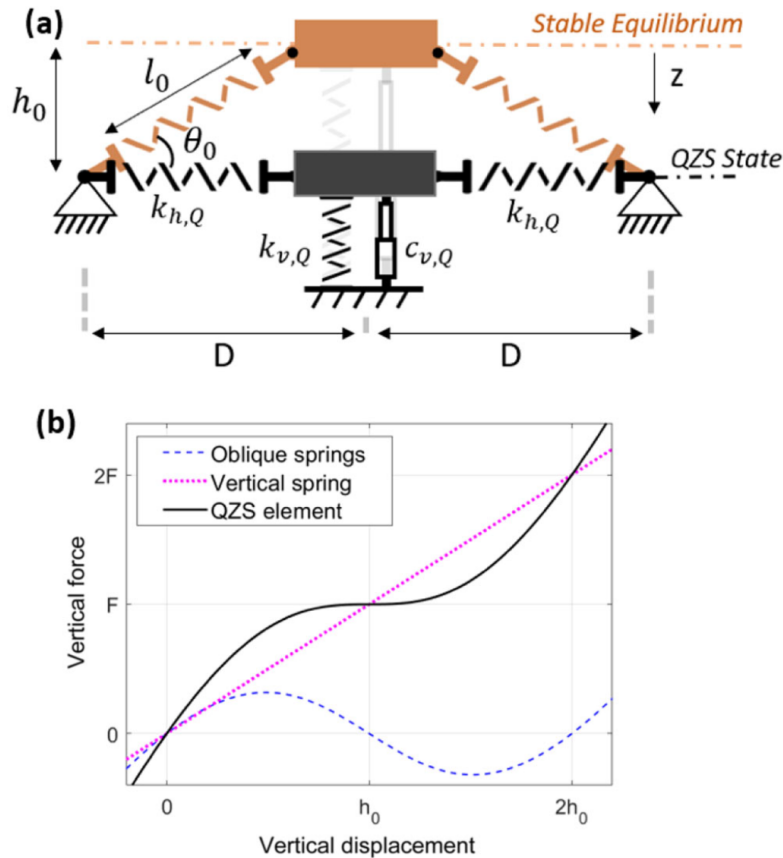


Figure 2.20: Quasi-zero stiffness (QZS) element. (a) Mass-spring representation. (b) Force-deformation relationships [23]

Recent developments in the field of seismic vibration mitigation have explored a number of innovative techniques to improve the robustness and effectiveness of structural control systems, and a study by Menga [24] investigated the use of nonlinear viscoelastic damping in rubber layer roller bearings (RLRBs) with nonlinear third-order springs. This approach has

shown superior performance in isolating loads over a wide excitation spectrum compared to conventional linear isolators and is particularly suitable for applications where the excitation spectrum is unknown.

The researchers developed a dynamic model to study a simple structure that provides seismic isolation through RLRBs consisting of rigid cylinders rolling on rigid plates with a high damping rubber coating. The system is equipped with non-linear third-order springs that provide both non-linear damping and stiffness as it is possible to see in Figure 2.21. The study found that when subjected to cyclic loading, different dynamic regimes emerge depending on whether the viscoelastic damping peak is exceeded. In this case, a sudden reduction in damping can cause weakly damped self-excited oscillations.

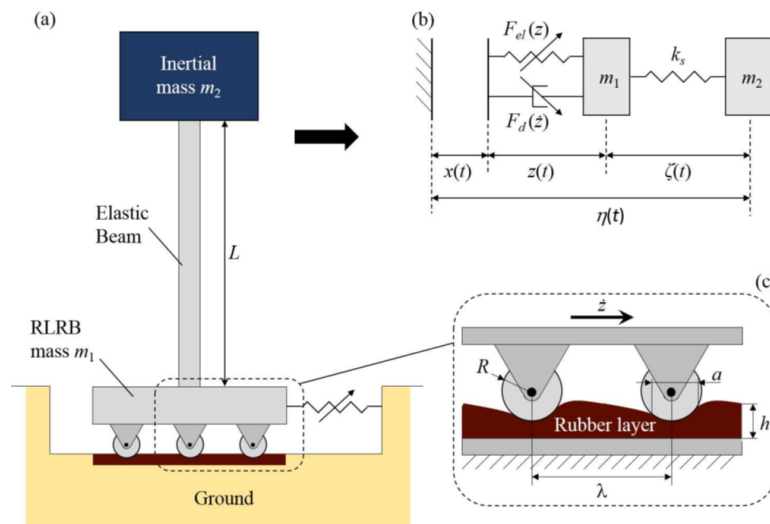


Figure 2.21: Two degree-of-freedom base-isolation scheme. (a) The ground vibration x is filtered by means of the RLRB non-linear damping force, and the non-linear elastic term. (b) Lumped element scheme. (c) RLRB close-up showing the rolling contact between the rigid rollers of radius R and the viscoelastic rubber layer of thickness [24]

To investigate the robustness of the seismic isolation performance, a series of real seismic excitations are considered in this study. The results show that tuned nonlinear RLRBs exhibit better seismic isolation performance

over a wider range of excitation spectrum compared to common linear isolators. This makes nonlinear RLRBs particularly suitable for applications such as seismic and fault engineering, where the specific excitation spectrum is known in advance and blind design based on statistical data is required. Driven by the need for adaptive and robust control systems, **Eshkevari** [25] introduces RL-Controller, a reinforcement learning framework designed for active structural control. This model-free approach uses reinforcement learning to transform classical model-based active control problems into data-driven ones; RL-Controller requires no prior knowledge of system dynamics, significantly reducing interlaminar drift under strong seismic motion by 65% on average, compared to 25% for the LQG (Linear Quadratic Gaussian) control method.

The RL-Controller framework includes attributes and features that model active structural control mechanisms in detail; the RL-Controller framework can be easily trained on a five-story reference building and when subjected to strong seismic motion, it has been shown that interlayer Drift is significantly reduced; in a comparative study with the LQG active control method, RL-Controller learns a more optimal actuator forcing strategy resulting in higher performance. The model-free algorithm is adaptive and efficient as it does not depend on a priori knowledge about the system dynamics.

This work explores the application of reinforcement learning (RL) for adaptive control in robotic systems and extends it to structural engineering. The RL framework formulates the control problem as a sequential decision process modeled by a Markov decision process (MDP). The RL controller uses neural networks to approximate the value function, process information about the current state of the system, and select actions that maximize the cumulative reward over time. This approach addresses the complexity of high-dimensional and continuous state-action spaces and is suitable for real-world structural control problems.

Finally, to complement these developments, **Chen and Chien** [26] use machine learning models, in particular multilayer perceptrons (MLP) and autoregression with exogenous inputs (ARX), to mimic the control forces generated by linear quadrature regularizers (LQR) in structures with active mass dampers (AMD). In this study, both numerical simulations and experimental validation using shake table tests are performed. The results show that both MLP and ARX models can effectively estimate the control forces, reducing the need for state estimation and improving the real-time control

performance. This machine learning approach simplifies the control process by directly using measurable responses to calculate the control forces, thus improving the overall effectiveness of the seismic control system.

The researchers applied machine learning to learn the control forces generated from LQRs with optimised weight matrices using a symbiotic biological search algorithm. A 10-story benchmark building was used to train and validate the MLP and ARX models. The MLP model is a supervised, input-to-output function learning, while the ARX model is a recurrent dynamic neural network used for time series modeling. Both models are trained to mimic the LQR control forces directly from the acceleration response and show that state estimation is not necessary to implement optimal control in real applications.

The study also includes experimental validation (in Figure 2.22 the experimental setup can be observed) through shake table tests in a laboratory environment with structural models controlled by AMD: the experimental results and structural control performance of MLP and ARX models are compared with LQR using Kalman filter. The results show that machine learning-based controllers can effectively replace traditional state feedback controllers, reducing the need for state estimation and improving the overall control performance.

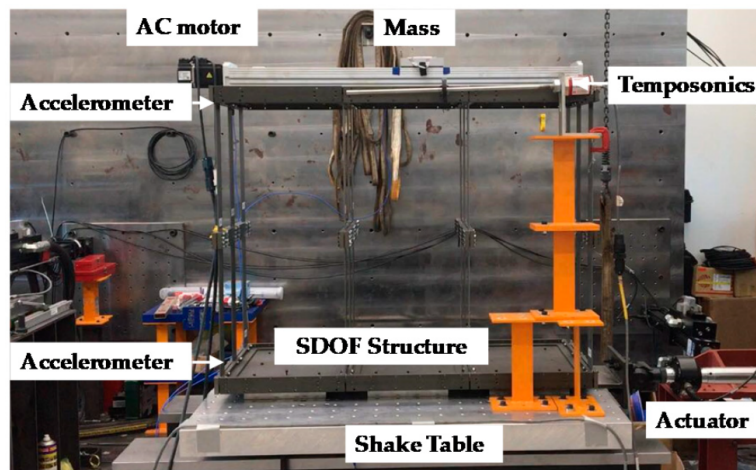


Figure 2.22: Experimental setup for controlling structural models by the use of AMD [26]

2.3 Future directions

Research is expanding into hybrid bistable systems, which combine bistable mechanisms with smart materials (such as shape-memory alloys) to create multifunctional components. The development of computational optimisation for bistable devices allows for precise modelling of energy dissipation and adaptability. The use of bistable dampers in seismic retrofitting is a promising innovation that can protect heritage structures and critical infrastructure.

Despite these advances, several challenges remain in the study and application of bistable systems. One of them is the accurate control of bistable transitions, especially in complex and dynamic environments. The development of reliable and robust control strategies is essential for the practical use of bistable systems in real-world applications. Furthermore, the long-term durability and stability of bistable elements under cyclic loading cycles must be addressed to ensure their reliability and long lifetime.

2.4 Conclusion

The unique dynamic properties of bistable structures, characterized by their ability to transition between steady states, enable innovative solutions in various engineering fields.

Bistable dynamics offer transformative possibilities for managing seismic loads. The versatility of bistability in seismic engineering is demonstrated by its ability to enable efficient energy dissipation, adaptive responses and sustainable energy solutions. Further advancements in material science and computational design are expected to unlock its full potential for widespread applications.

Chapter 3

Study of the bistable element

As established in Chapter 1, Karpov's work [1] provides a solid theoretical foundation for the understanding of bistable mechanisms, particularly in the context of energy dissipating systems in seismic design. Section 1.3 and Figure 1.2 in Section 1.2 detail the important role that bistability plays in achieving controlled energy absorption and highlight how key *design parameters* (such as stiffness ratio (k) and initial angle (θ_0)) govern the transient behaviour and the overall dynamic response of the system.

This theoretical framework not only supports the proposed innovative seismic application, but also motivates the practical development of numerical models that can accurately capture the complex behaviour of bistable elements under dynamic loading. This chapter builds directly on this theoretical foundation and extends the discussion to the field of computational analysis. The aim is to bridge the gap between the abstract and comprehensive analytical models introduced earlier and the concrete simulation-based approaches needed to validate these concepts in practical scenarios. By translating the theoretical constructs into a detailed numerical framework, the dynamic performance of bistable energy dissipators is rigorously analysed and their seismic potential is investigated.

3.1 Development of the numerical model with OpenSees

A numerical model of the energy dissipation device incorporating bistable elements is developed using OpenSees. Starting from the geometrical configuration shown in [Figure 1.2](#), the model focuses on reproducing the complex non-linear behaviour that characterises bistable systems. This application is facilitated by the STKO interface, which provides a user-friendly environment for setting up and running highly non-linear dynamic simulations. This choice of software is particularly suitable for capturing transitional events and state transitions between stable equilibrium configurations. This behaviour is central to the performance of bistable elements, as highlighted in the previous section.

The numerical model is designed to reflect the key aspects discussed in [Chapter 1](#), such as the interaction between the *design parameters* (k and θ_0) and the resulting energy landscape. By simulating various parametric conditions, it is possible to systematically investigate how these parameters affect important aspects of element response, such as the stability threshold and the degree of energy dissipation during dynamic events. This computational approach not only supports theoretical predictions, but also provides useful information to optimise bistable devices for practical seismic applications.

In addition, OpenSees and STKO can be used to incorporate advanced features such as mesh refinement and the specification of detailed boundary conditions to ensure model robustness and adaptability to different loading scenarios. Throughout the development process, repeated validation against the theoretical criteria established in [Chapter 1](#) strengthens the reliability of the numerical analysis and establishes a clear link between the conceptual and practical aspects of the study.

Moving to the development of the model, it is important to recall the reference figure for the development of the model:

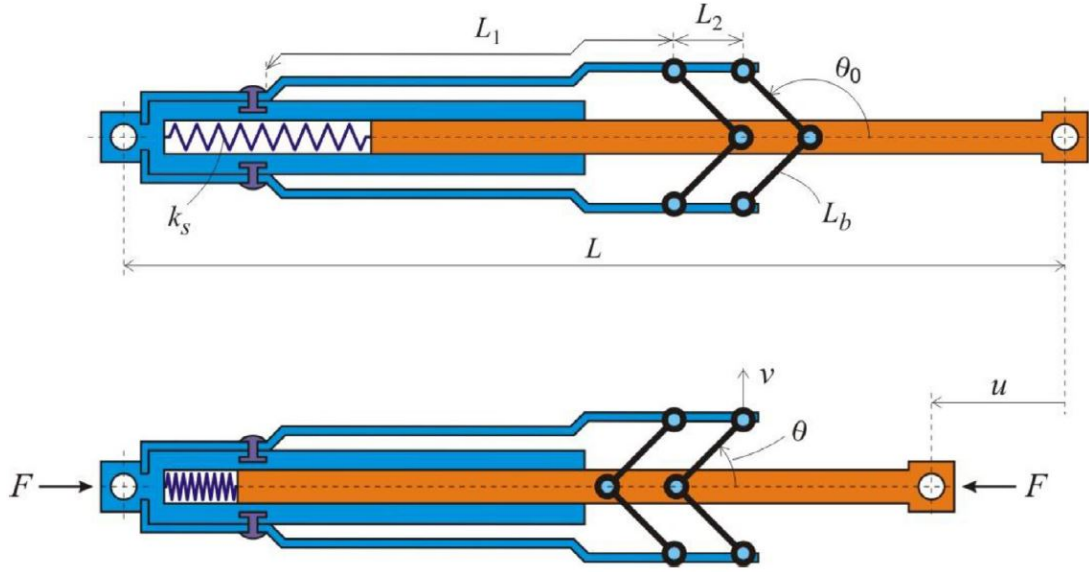


Figure 3.1: Bistable axial bar element: θ is inclination angle of the rigid hinged bars in a state of equilibrium for the external load F ; u is horizontal displacement if the middle slider, v is vertical displacement of the flappers; L_b is length of the hinged bars; k_s is axial stiffness of the encapsulated spring; distances L_1 and L_2 and bending rigidity (EI) of the flappers determine its bending stiffness, $k_b = 12EI[(3L_1 + L_2)/L_1^3 \cdot (3L_1 + 4L_2)]$; and θ_0 is initial of angle of the hinged bars, prior to loading [1]

Considering this figure (Figure 1.2), it is possible to define the following summary table (Table 3.1):

Element	Property	Value	Unit of measurement
Slider	Length	3300	[mm]
Slider	Young's Modulus	210000	[N/mm^2]
Flapper	Length L_1	2500	[mm]
Flapper	Length L_2	500	[mm]
Spring	Length	300	[mm]
Initial angle	θ_0	45	[$^\circ$]

Table 3.1: Summary table of object properties

By entering the coordinates, it was possible to create the geometry of the under examination object in STKO.

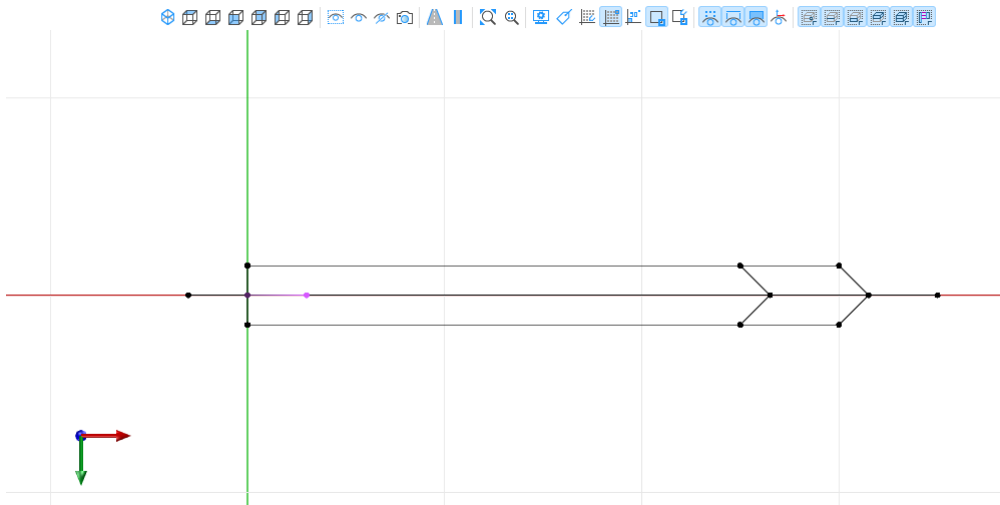


Figure 3.2: Geometry of the model

Once defined, the boundary conditions were set taking into account the behaviour of the bistable element. Below it is provided both the figure showing the points of application of the boundary conditions for the object under examination, and the visual list from STKO regarding these conditions.

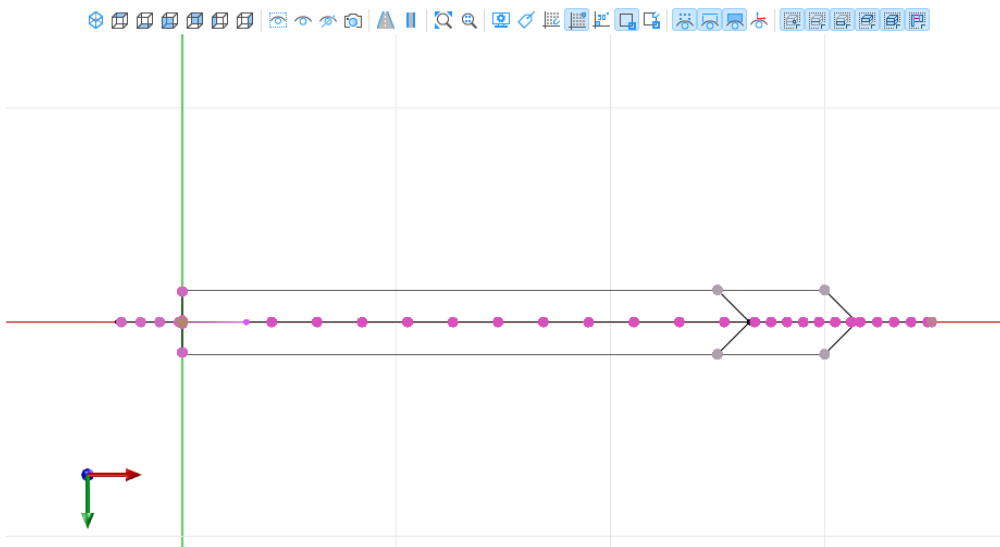


Figure 3.3: Boundary conditions of the model

▼	🔗	Conditions	
	🔗	[1] Fixed ALL	Constraints.sp.fix
	🔗	[2] Fix slider Y	Constraints.sp.fix
	🔗	[6] Fix flapper node connec...	Constraints.sp.fix
	🔗	[7] Mass on node 3	Mass.NodeMass
	🔗	[9] ground motion	Ground_Motion.groundMotion

Figure 3.4: List of boundary conditions of the model

Then, properties of the element have been defined, followed by a meshing of the model, the latter of fundamental importance in order to run the analysis.

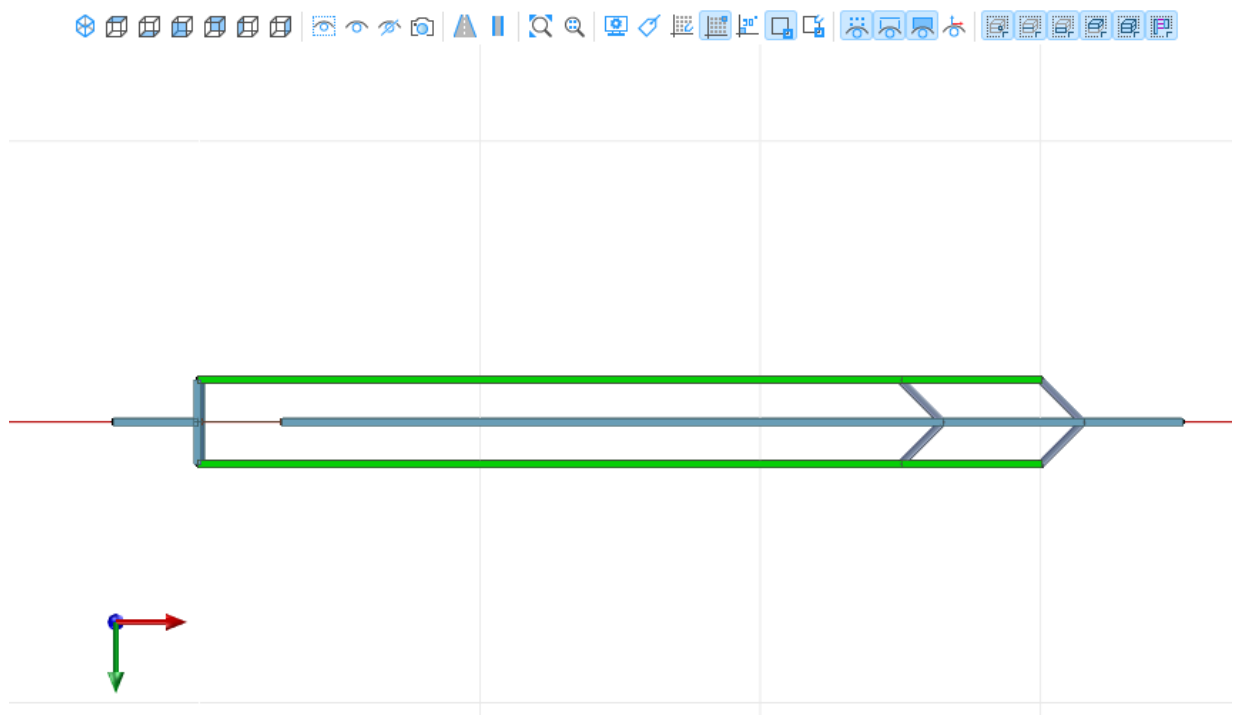


Figure 3.5: Properties of the model

<ul style="list-style-type: none"> <ul style="list-style-type: none"> Physical Properties [1] Flapper [2] Slider [3] end-spring material [5] end-spring property [6] truss stiff material [7] stiff truss <ul style="list-style-type: none"> Element Properties [1] Spring [2] Flapper [3] Truss 	<ul style="list-style-type: none"> sections.Elastic sections.Elastic materials.uniaxial.Elastic special_purpose.zeroLengthMaterial materials.uniaxial.Elastic special_purpose.truss zero_length_elements.zeroLength beam_column_elements.elasticBeamColumn truss_elements.truss
---	--

Figure 3.6: List of properties

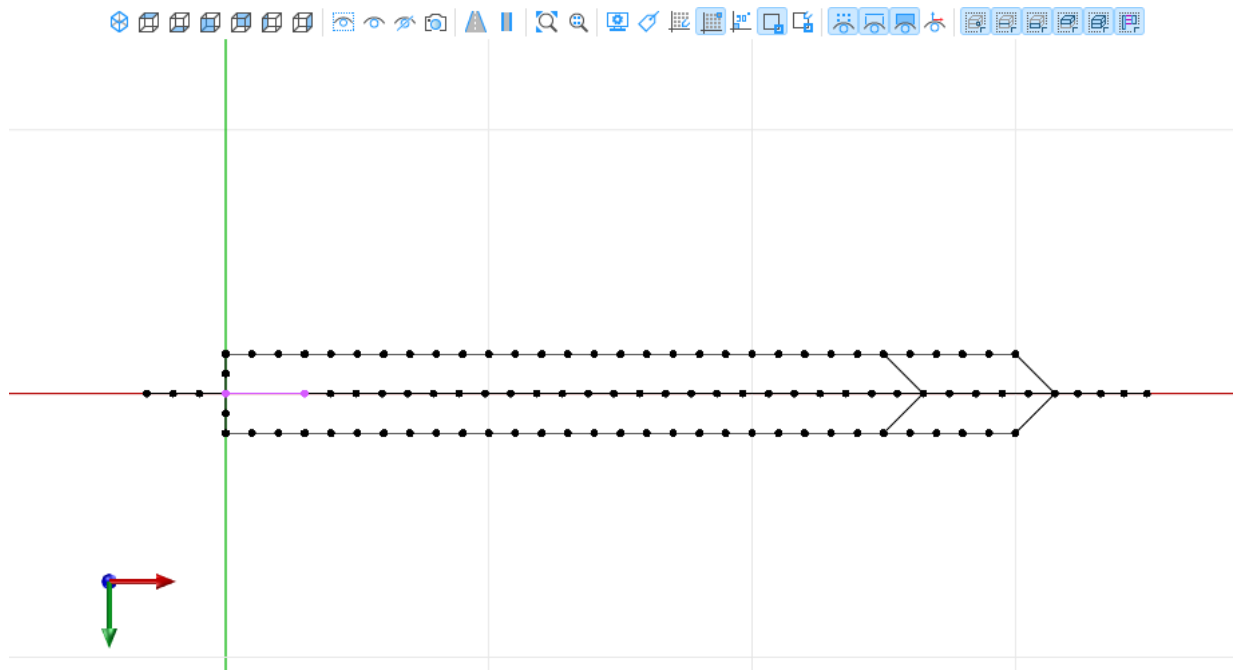


Figure 3.7: Mesh

Moreover, an acceleration history has been created and provided in order to simulate the acting of an harmonic excitation on the structure. Lastly, the analysis has been decided.

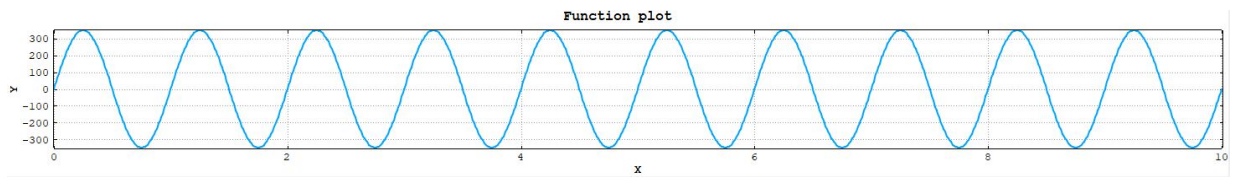


Figure 3.8: Time Series

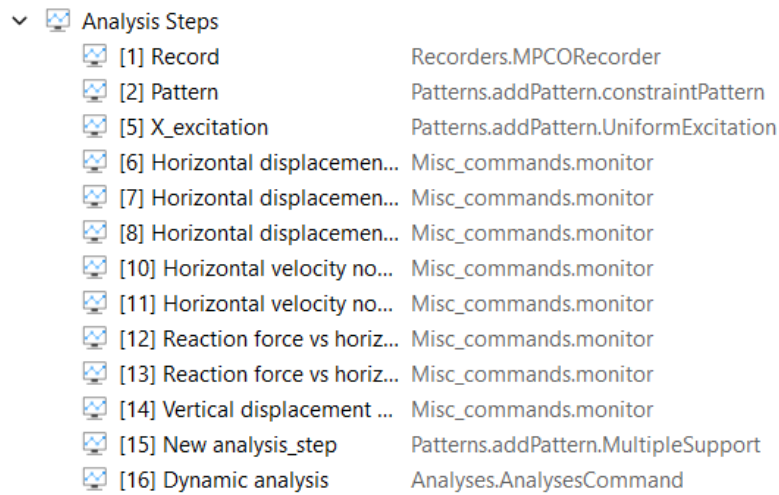


Figure 3.9: Analysis

After performing the analysis, by switching from the Pre-Processor to the Post-Processor, it is possible to observe the deformation of the element under the harmonic excitation administrated.

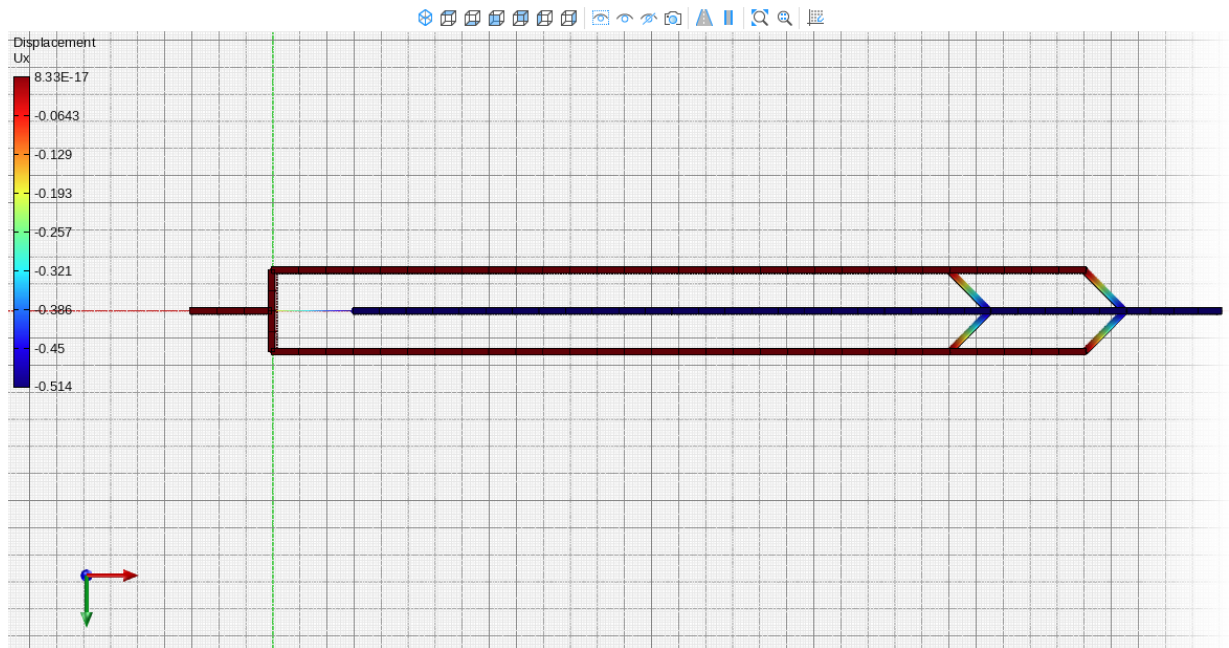


Figure 3.10: Displacement at $t = 0$

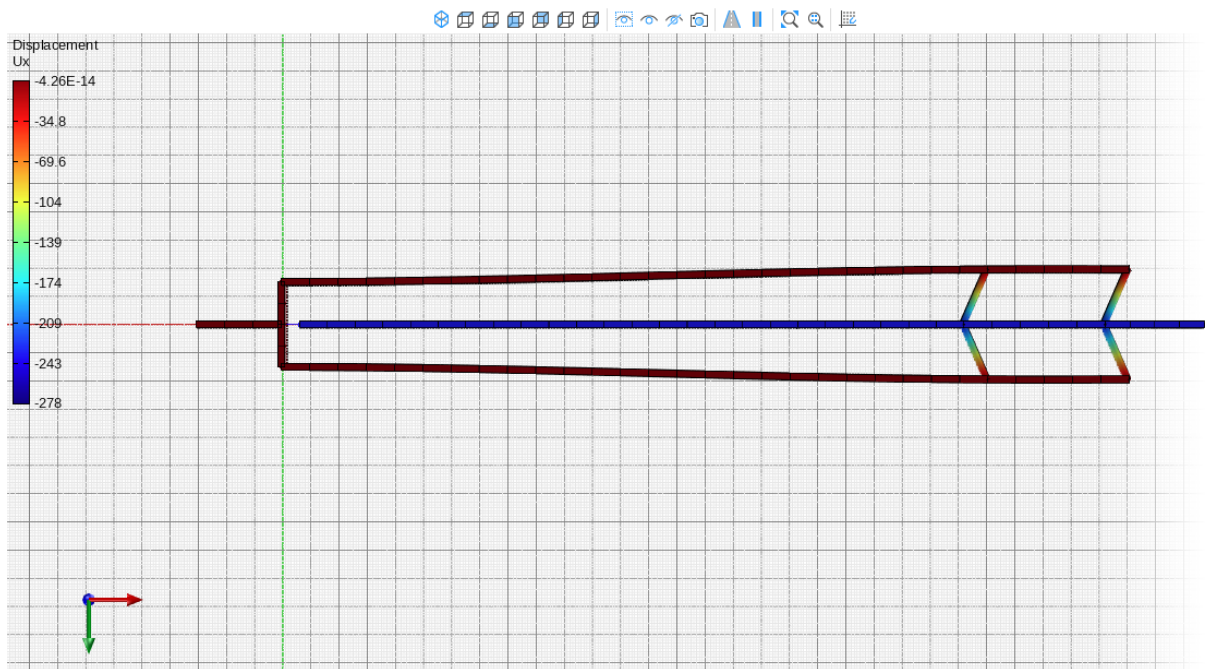


Figure 3.11: Displacement at $t(u_{max})$

3.2 Parametric analysis

With reference to Section 1.3.2, the study proceeds with a parametric analysis in which the *design parameters* (k, θ_0) are varied. It is important to recall that the parameter k is defined as the ratio of the spring stiffness to the bending stiffness, i.e. ($k = \frac{k_s}{k_b}$), while (θ_0) denotes the initial angle. For the initial configuration, an angle of ($\theta_0 = 45^\circ$) and a stiffness ratio ($k = 0.12$) were chosen. The table below summarises the various parameter combinations considered in this study.

Simulation No.	θ_0 [°]	k	k_s [kN/mm]	E_s [N/mm ²]
1	45°	0.12	5.3×10^{-4}	159.12
2	45°	0.10	4.42×10^{-4}	132.63
3	45°	0.32	1.41×10^{-3}	424.32
4	45°	0.02	8.84×10^{-5}	26.52
5	45°	0.22	9.72×10^{-4}	291.2

Table 3.2: Summary of Parameter Combinations

Simulation No.	θ_0 [°]	k	k_s [kN/mm]	E_s [N/mm ²]
1	30°	0.12	5.3×10^{-4}	159.12
2	30°	0.10	4.42×10^{-4}	132.63
3	30°	0.32	1.41×10^{-3}	424.32
3	30°	0.02	8.84×10^{-5}	26.52
5	30°	0.22	9.72×10^{-4}	291.2

Table 3.3: Summary of Parameter Combinations

Simulation No.	θ_0 [°]	k	k_s [kN/mm]	E_s [N/mm ²]
1	65°	0.12	5.3×10^{-4}	159.12
2	65°	0.10	4.42×10^{-4}	132.63
3	65°	0.32	1.41×10^{-3}	424.32
4	65°	0.02	8.84×10^{-5}	26.52
5	65°	0.22	9.72×10^{-4}	291.2

Table 3.4: Summary of Parameter Combinations

In order to calculate k_s , it is important to recall that, in order to determine

Simulation No.	θ_0 [°]	k	k_s [kN/mm]	E_s [N/mm ²]
1	55°	0.12	5.3×10^{-4}	159.12
2	55°	0.10	4.42×10^{-4}	132.63
3	55°	0.32	1.41×10^{-3}	424.32
4	55°	0.02	8.84×10^{-5}	26.52
5	55°	0.22	9.72×10^{-4}	291.2

Table 3.5: Summary of Parameter Combinations

Simulation No.	θ_0 [°]	k	k_s [kN/mm]	E_s [N/mm ²]
1	37.5°	0.12	5.3×10^{-4}	159.12
2	37.5°	0.10	4.42×10^{-4}	132.63
3	37.5°	0.32	1.41×10^{-3}	424.32
4	37.5°	0.02	8.84×10^{-5}	26.52
5	37.5°	0.22	9.72×10^{-4}	291.2

Table 3.6: Summary of Parameter Combinations

k_b , equation (Equation 1.3.2) must be used. Thus, we have:

$$k_b = 12EI \frac{(3L_1 + L_2)}{L_1^3 \cdot (3L_1 + 4L_2)} = 4.42 \times 10^{-3} kN/mm \quad (3.1)$$

Given that k has been specified, k_s can be obtained by multiplying k by k_b :

$$k_s = k \cdot k_b \quad (3.2)$$

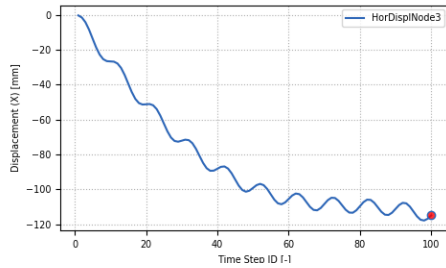
Using this equation, and considering the spring length reported in Table (Table 3.1) along with a unitary area, the Young's modulus of the spring can be determined as follows:

$$E_s = \frac{L_s \cdot k_s}{A_s} \quad (3.3)$$

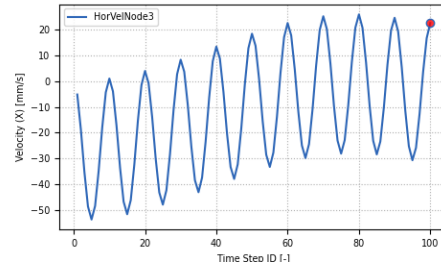
This value must then be entered into STKO to define the spring's properties. Once all of these parameters have been defined, the numerical simulation can proceed.

3.2.1 $\theta_0 = 30^\circ$

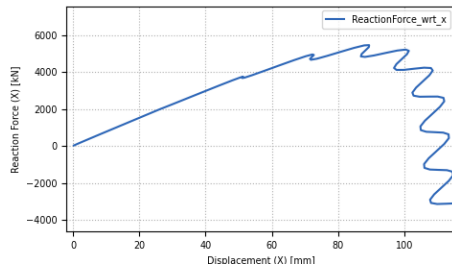
Uniform excitation, Penalty method, $k=0.12$



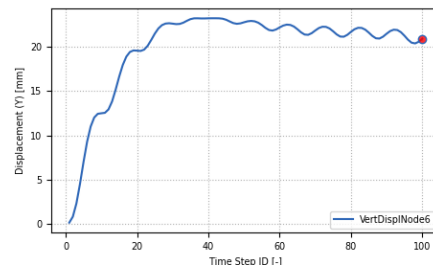
(a) Horizontal displacement of Node 3



(b) Horizontal velocity of Node 3



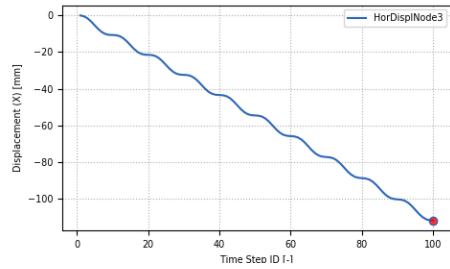
(c) Reaction force vs Displacement of Node 3



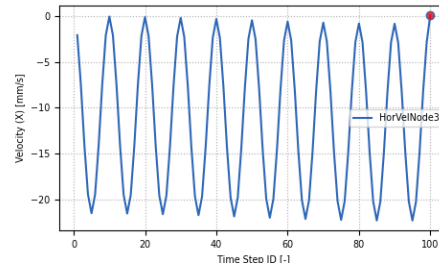
(d) Vertical displacement of Node 6

Figure 3.12: Simulation 1: $k=0.12$

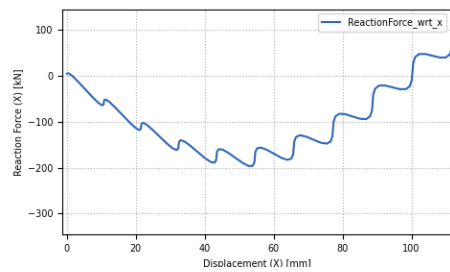
Uniform excitation, Transformation method, $k=0.12$



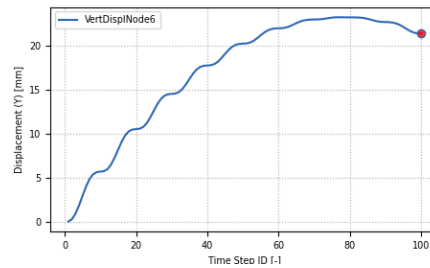
(a) Horizontal displacement of Node 3



(b) Horizontal velocity of Node 3



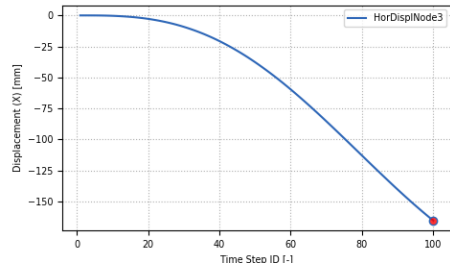
(c) Reaction force vs Displacement of Node 3



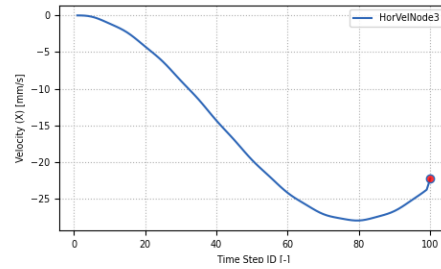
(d) Vertical displacement of Node 6

Figure 3.13: Simulation 1: $k=0.12$

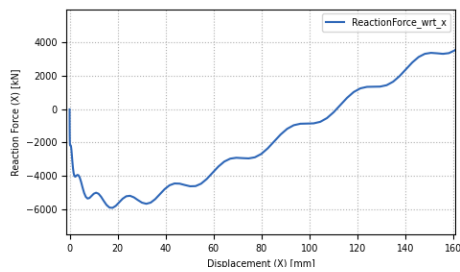
Multi-support excitation, Penalty method, $k=0.12$



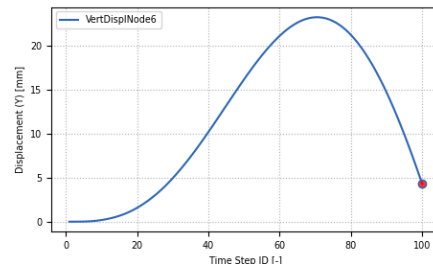
(a) Horizontal displacement of Node 3



(b) Horizontal velocity of Node 3



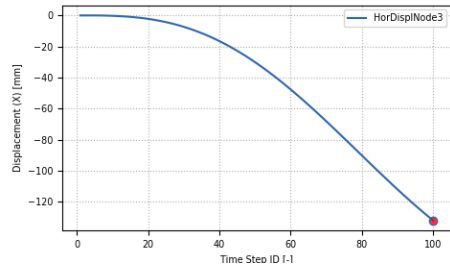
(c) Reaction force vs Displacement of Node 3



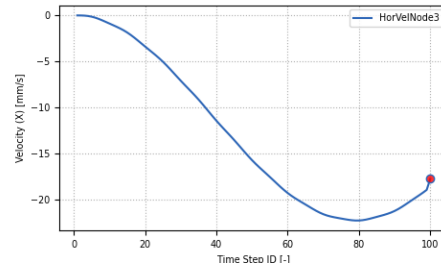
(d) Vertical displacement of Node 6

Figure 3.14: Simulation 1: $k=0.12$

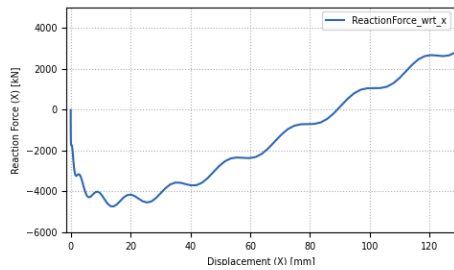
Multi-support excitation, Transformation method, $k=0.12$



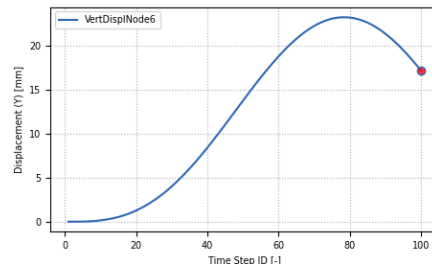
(a) Horizontal displacement of Node 3



(b) Horizontal velocity of Node 3



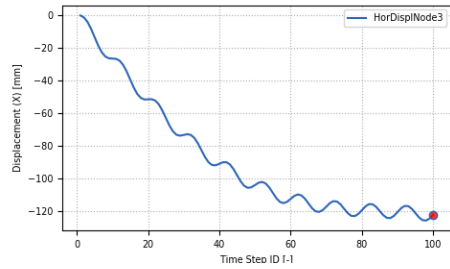
(c) Reaction force vs Displacement of Node 3



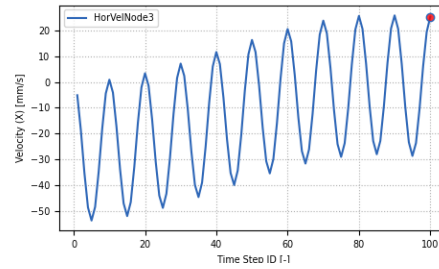
(d) Vertical displacement of Node 6

Figure 3.15: Simulation 1: $k=0.12$

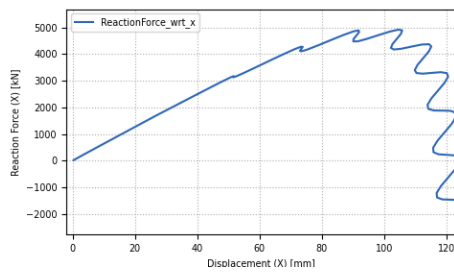
Uniform excitation, Penalty method, $k=0.10$



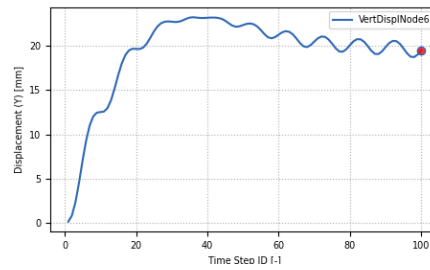
(a) Horizontal displacement of Node 3



(b) Horizontal velocity of Node 3



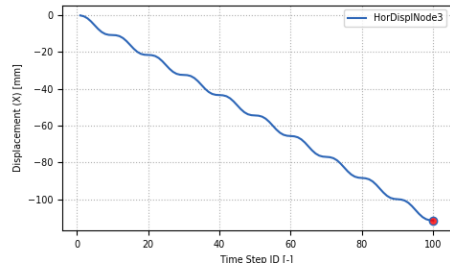
(c) Reaction force vs Displacement of Node 3



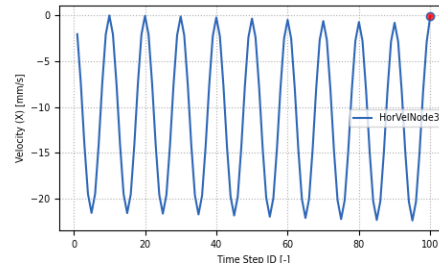
(d) Vertical displacement of Node 6

Figure 3.16: Simulation 1: $k=0.10$

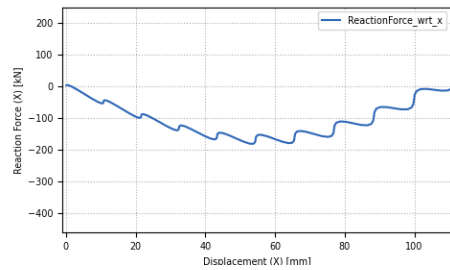
Uniform excitation, Transformation method, $k=0.10$



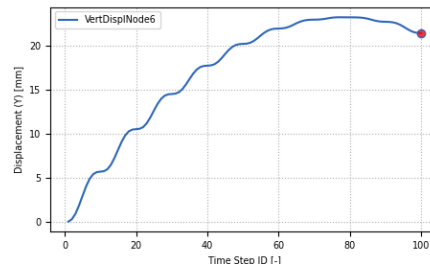
(a) Horizontal displacement of Node 3



(b) Horizontal velocity of Node 3



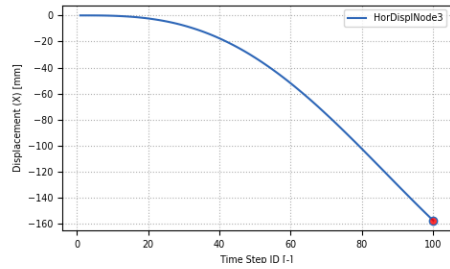
(c) Reaction force vs Displacement of Node 3



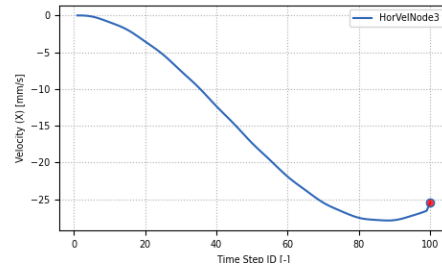
(d) Vertical displacement of Node 6

Figure 3.17: Simulation 1: $k=0.10$

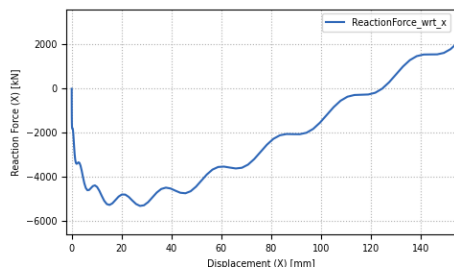
Multi-support excitation, Penalty method, $k=0.10$



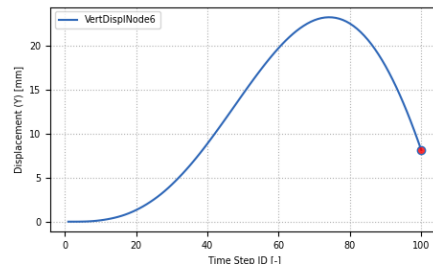
(a) Horizontal displacement of Node 3



(b) Horizontal velocity of Node 3



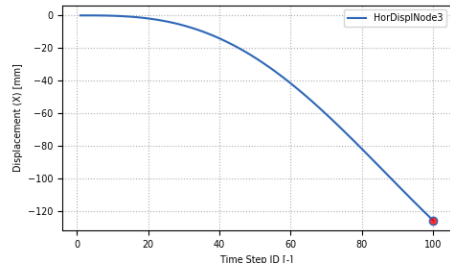
(c) Reaction force vs Displacement of Node 3



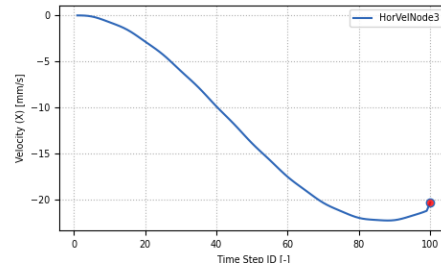
(d) Vertical displacement of Node 6

Figure 3.18: Simulation 1: $k=0.10$

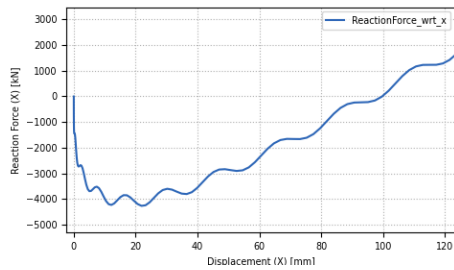
Multi-support excitation, Transformation method, $k=0.10$



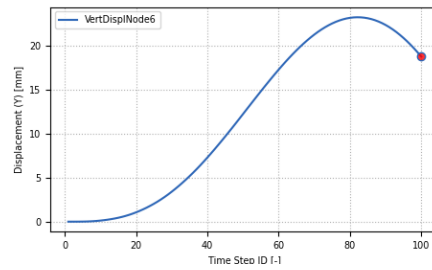
(a) Horizontal displacement of Node 3



(b) Horizontal velocity of Node 3



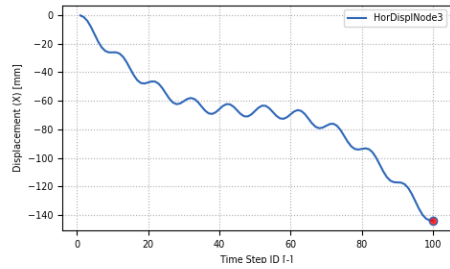
(c) Reaction force vs Displacement of Node 3



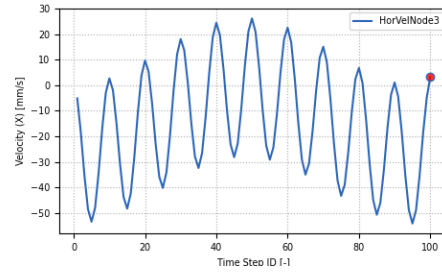
(d) Vertical displacement of Node 6

Figure 3.19: Simulation 1: $k=0.10$

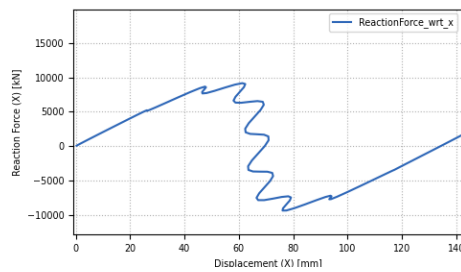
Uniform excitation, Penalty method, $k=0.32$



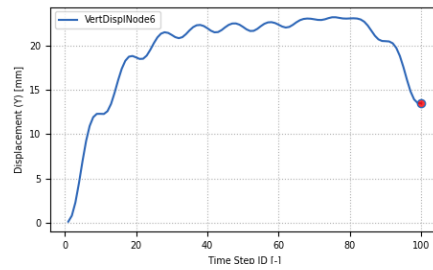
(a) Horizontal displacement of Node 3



(b) Horizontal velocity of Node 3



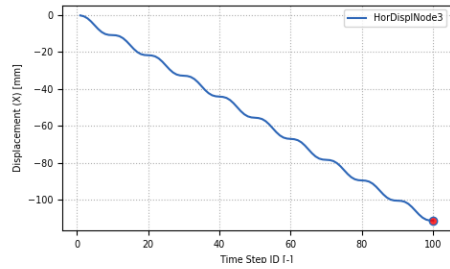
(c) Reaction force vs Displacement of Node 3



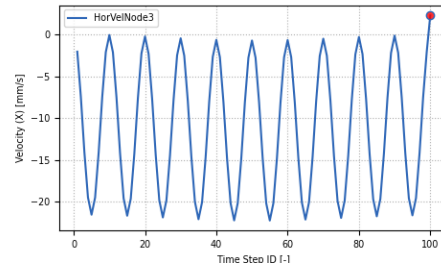
(d) Vertical displacement of Node 6

Figure 3.20: Simulation 1: $k=0.32$

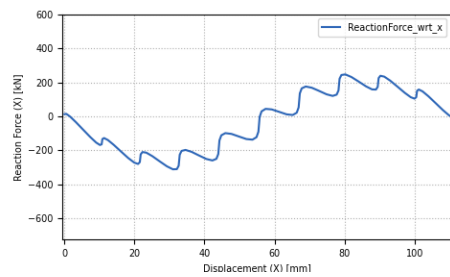
Uniform excitation, Transformation method, $k=0.32$



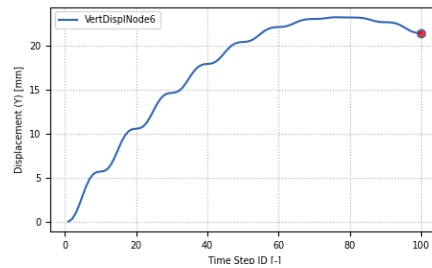
(a) Horizontal displacement of Node 3



(b) Horizontal velocity of Node 3



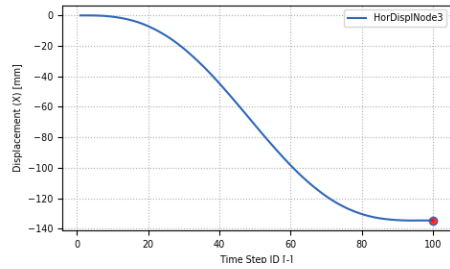
(c) Reaction force vs Displacement of Node 3



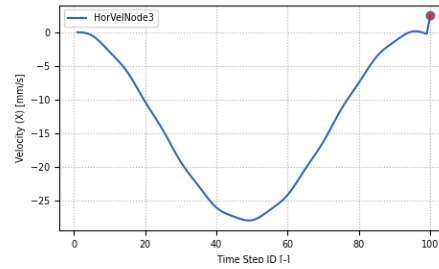
(d) Vertical displacement of Node 6

Figure 3.21: Simulation 1: $k=0.32$

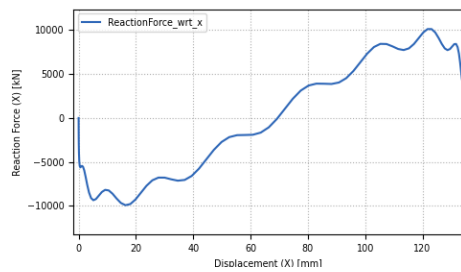
Multi-support excitation, Penalty method, $k=0.32$



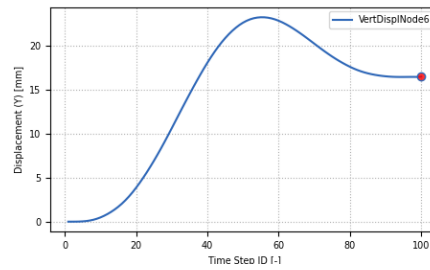
(a) Horizontal displacement of Node 3



(b) Horizontal velocity of Node 3



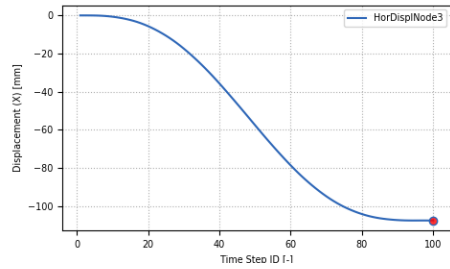
(c) Reaction force vs Displacement of Node 3



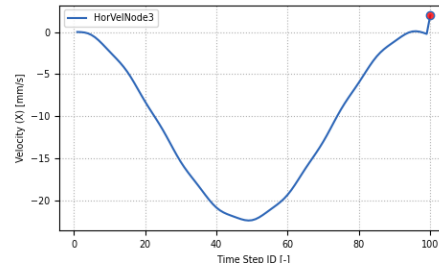
(d) Vertical displacement of Node 6

Figure 3.22: Simulation 1: $k=0.32$

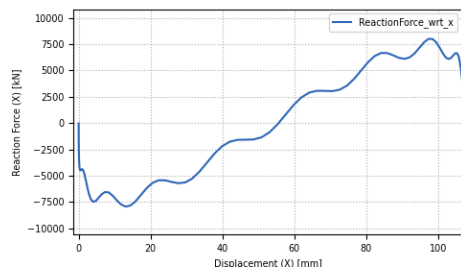
Multi-support excitation, Transformation method, $k=0.32$



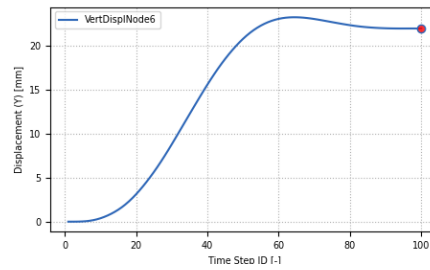
(a) Horizontal displacement of Node 3



(b) Horizontal velocity of Node 3



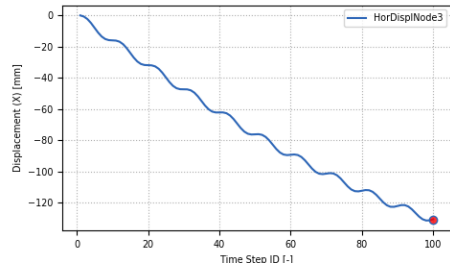
(c) Reaction force vs Displacement of Node 3



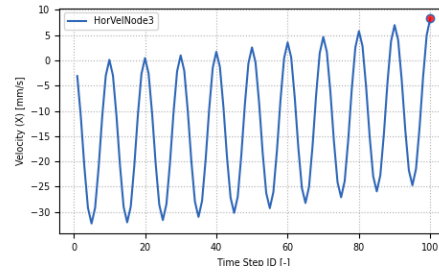
(d) Vertical displacement of Node 6

Figure 3.23: Simulation 1: $k=0.32$

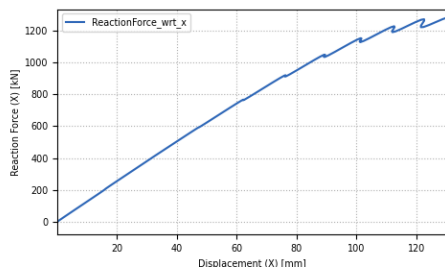
Uniform excitation, Penalty method, $k=0.02$



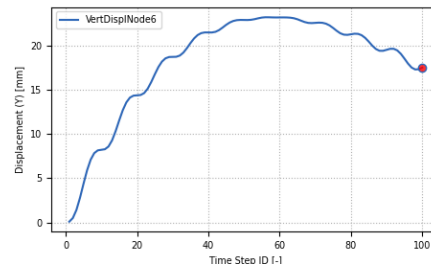
(a) Horizontal displacement of Node 3



(b) Horizontal velocity of Node 3



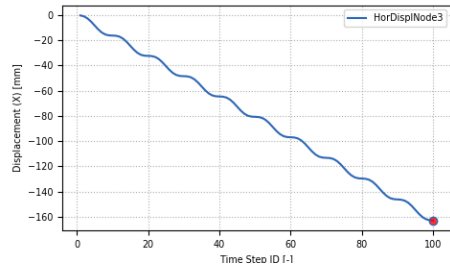
(c) Reaction force vs Displacement of Node 3



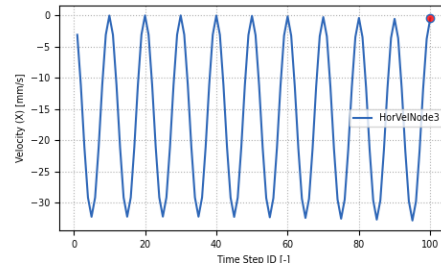
(d) Vertical displacement of Node 6

Figure 3.24: Simulation 1: $k=0.02$

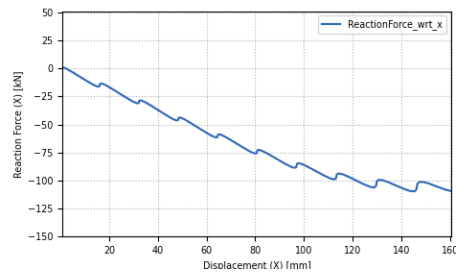
Uniform excitation, Transformation method, $k=0.02$



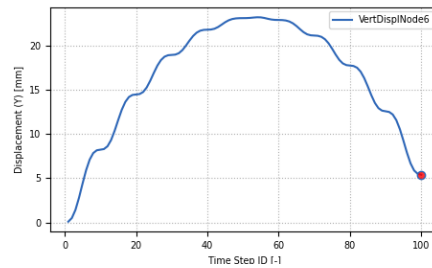
(a) Horizontal displacement of Node 3



(b) Horizontal velocity of Node 3



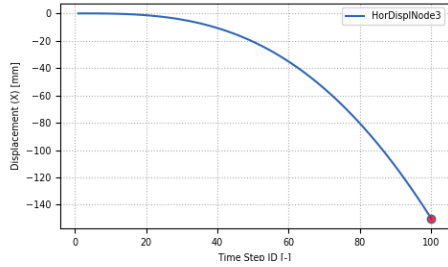
(c) Reaction force vs Displacement of Node 3



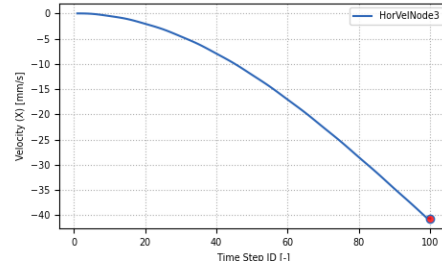
(d) Vertical displacement of Node 6

Figure 3.25: Simulation 1: $k=0.02$

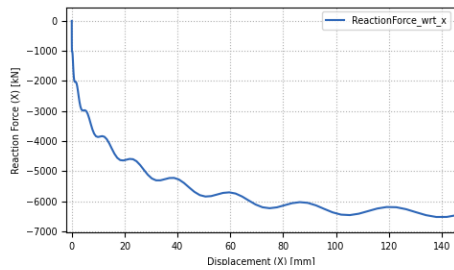
Multi-support excitation, Penalty method, $k=0.02$



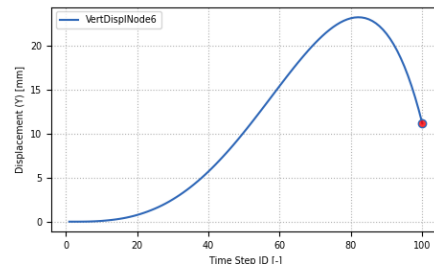
(a) Horizontal displacement of Node 3



(b) Horizontal velocity of Node 3



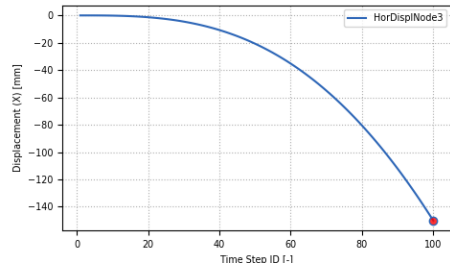
(c) Reaction force vs Displacement of Node 3



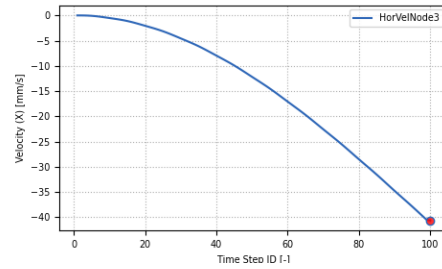
(d) Vertical displacement of Node 6

Figure 3.26: Simulation 1: $k=0.02$

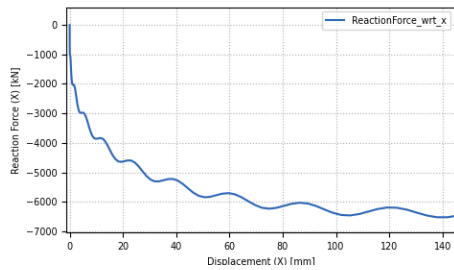
Multi-support excitation, Transformation method, $k=0.02$



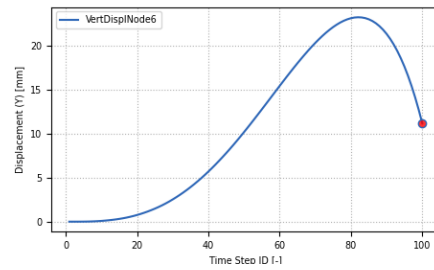
(a) Horizontal displacement of Node 3



(b) Horizontal velocity of Node 3



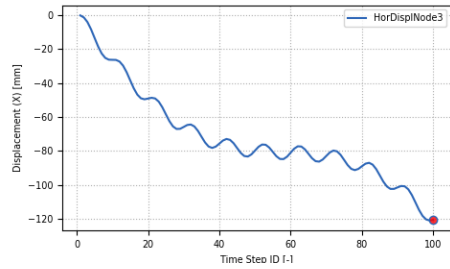
(c) Reaction force vs Displacement of Node 3



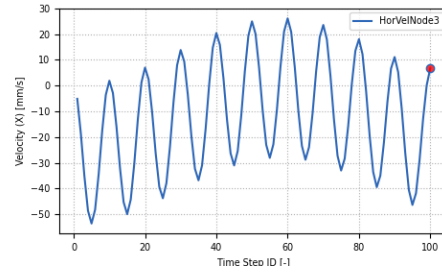
(d) Vertical displacement of Node 6

Figure 3.27: Simulation 1: $k=0.02$

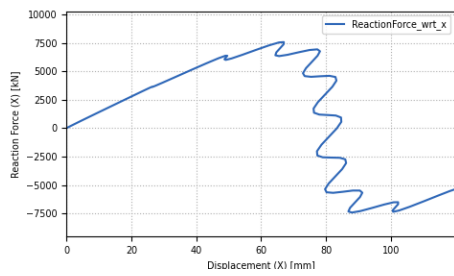
Uniform excitation, Penalty method, $k=0.22$



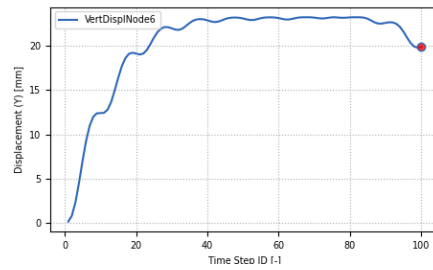
(a) Horizontal displacement of Node 3



(b) Horizontal velocity of Node 3



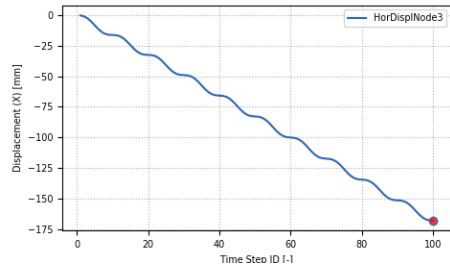
(c) Reaction force vs Displacement of Node 3



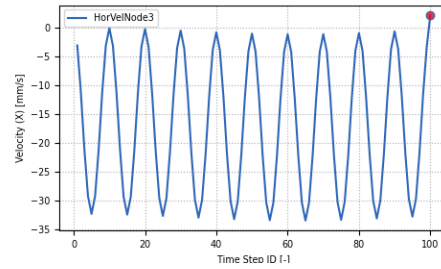
(d) Vertical displacement of Node 6

Figure 3.28: Simulation 1: $k=0.22$

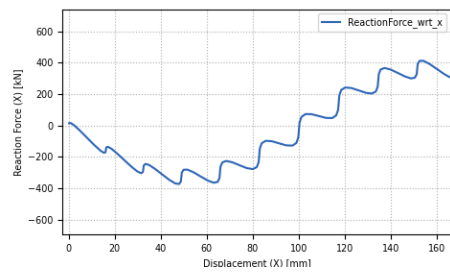
Uniform excitation, Transformation method, $k=0.22$



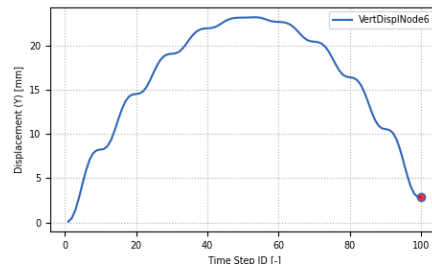
(a) Horizontal displacement of Node 3



(b) Horizontal velocity of Node 3



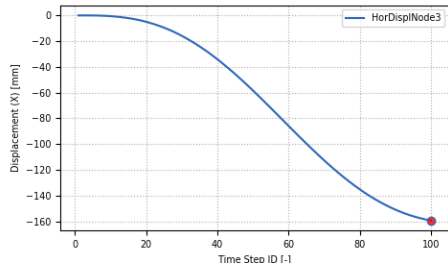
(c) Reaction force vs Displacement of Node 3



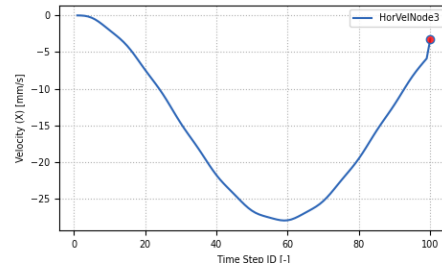
(d) Vertical displacement of Node 6

Figure 3.29: Simulation 1: $k=0.22$

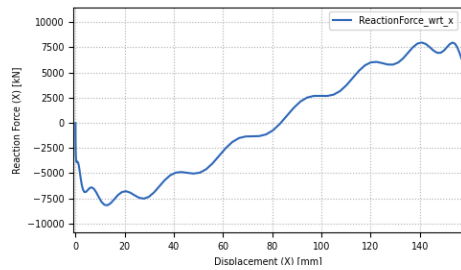
Multi-support excitation, Penalty method, $k=0.22$



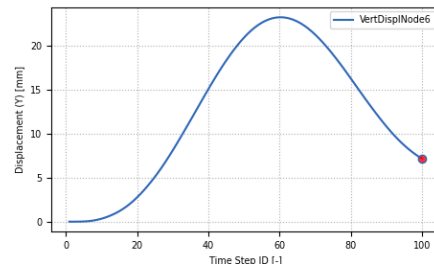
(a) Horizontal displacement of Node 3



(b) Horizontal velocity of Node 3



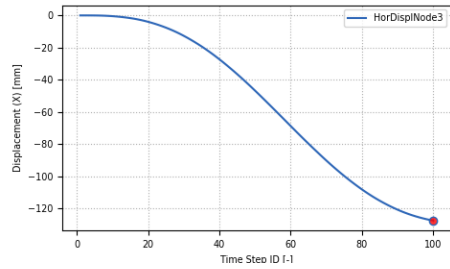
(c) Reaction force vs Displacement of Node 3



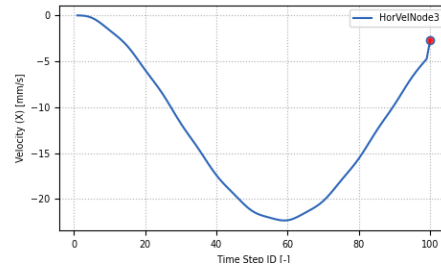
(d) Vertical displacement of Node 6

Figure 3.30: Simulation 1: $k=0.22$

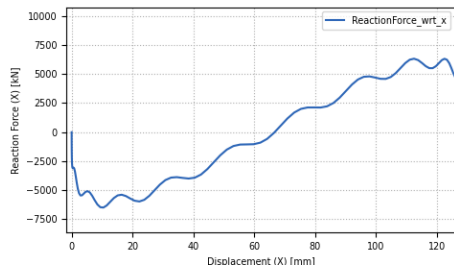
Multi-support excitation, Transformation method, $k=0.22$



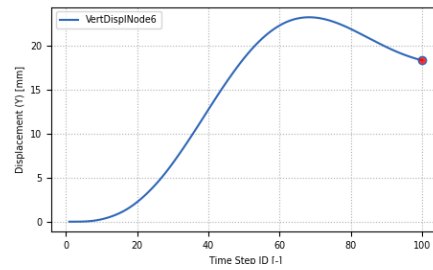
(a) Horizontal displacement of Node 3



(b) Horizontal velocity of Node 3



(c) Reaction force vs Displacement of Node 3

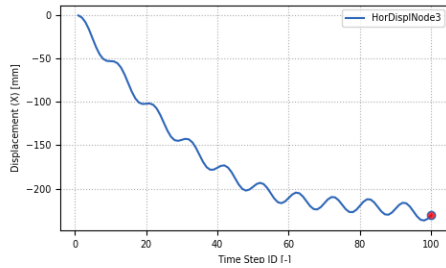


(d) Vertical displacement of Node 6

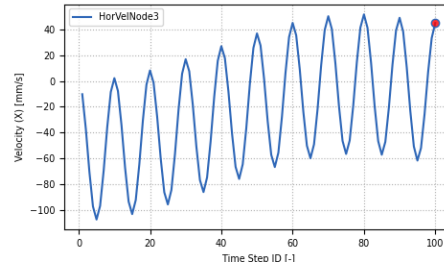
Figure 3.31: Simulation 1: $k=0.22$

3.2.2 $\theta_0 = 45^\circ$

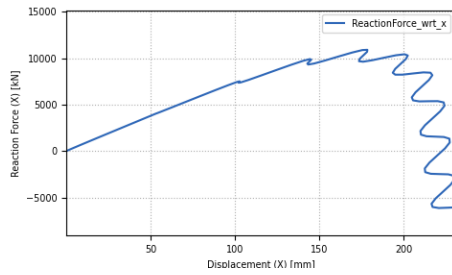
Uniform excitation, Penalty method, $k=0.12$



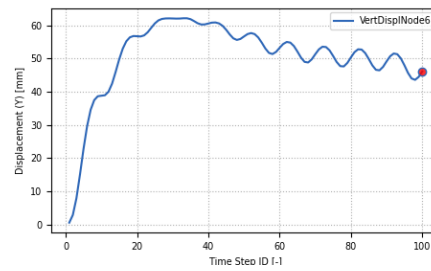
(a) Horizontal displacement of Node 3



(b) Horizontal velocity of Node 3



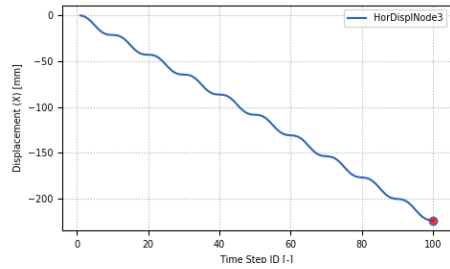
(c) Reaction force vs Displacement of Node 3



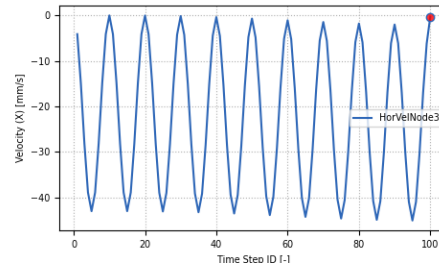
(d) Vertical displacement of Node 6

Figure 3.32: Simulation 1: $k=0.12$

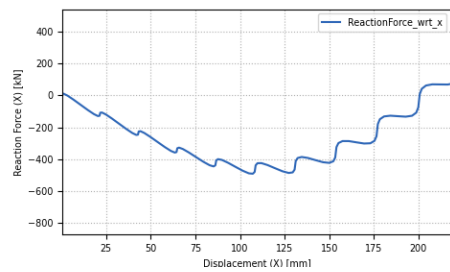
Uniform excitation, Transformation method, $k=0.12$



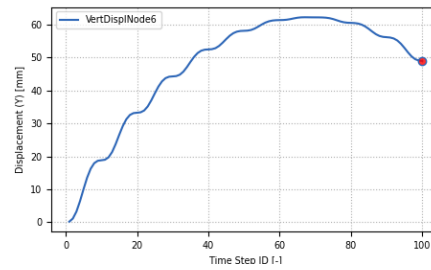
(a) Horizontal displacement of Node 3



(b) Horizontal velocity of Node 3



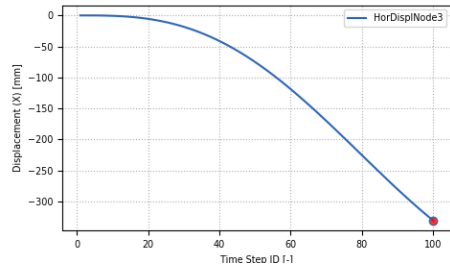
(c) Reaction force vs Displacement of Node 3



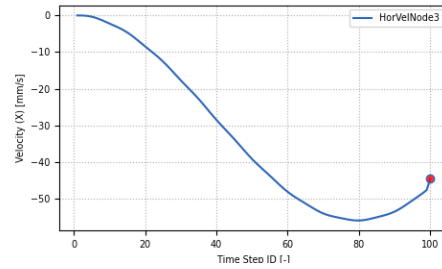
(d) Vertical displacement of Node 6

Figure 3.33: Simulation 1: $k=0.12$

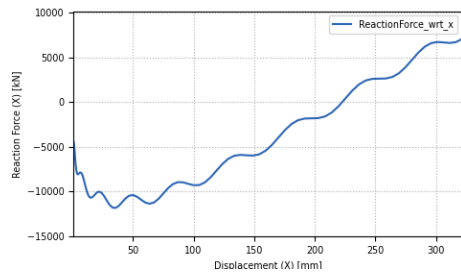
Multi-support excitation, Penalty method, $k=0.12$



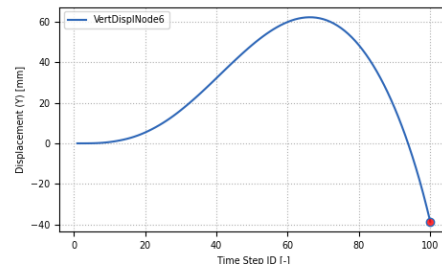
(a) Horizontal displacement of Node 3



(b) Horizontal velocity of Node 3



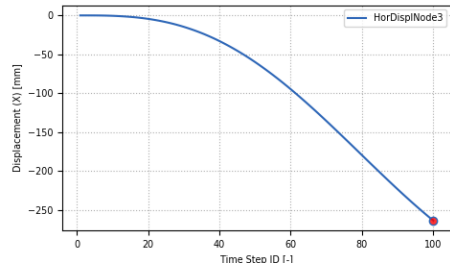
(c) Reaction force vs Displacement of Node 3



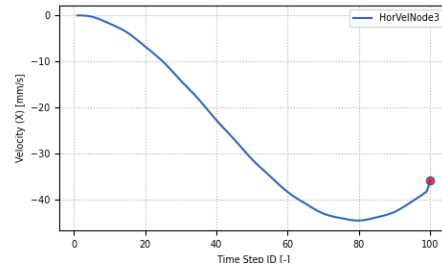
(d) Vertical displacement of Node 6

Figure 3.34: Simulation 1: $k=0.12$

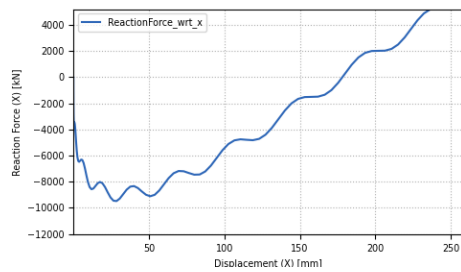
Multi-support excitation, Transformation method, $k=0.12$



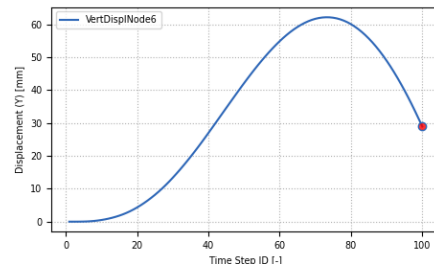
(a) Horizontal displacement of Node 3



(b) Horizontal velocity of Node 3



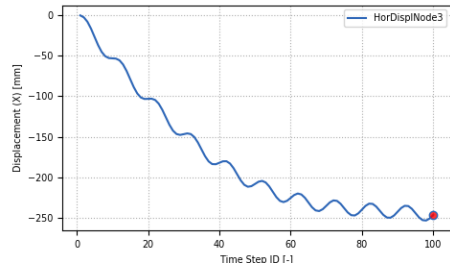
(c) Reaction force vs Displacement of Node 3



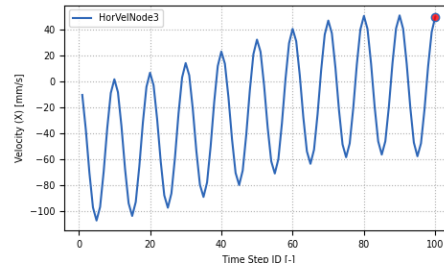
(d) Vertical displacement of Node 6

Figure 3.35: Simulation 1: $k=0.12$

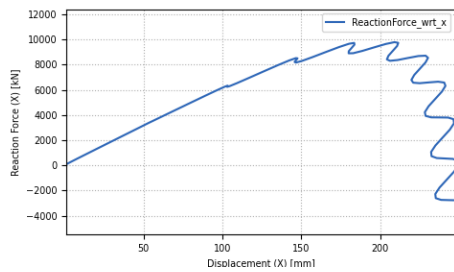
Uniform excitation, Penalty method, $k=0.10$



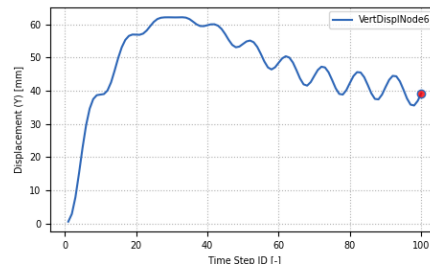
(a) Horizontal displacement of Node 3



(b) Horizontal velocity of Node 3



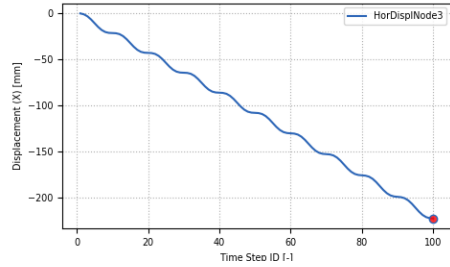
(c) Reaction force vs Displacement of Node 3



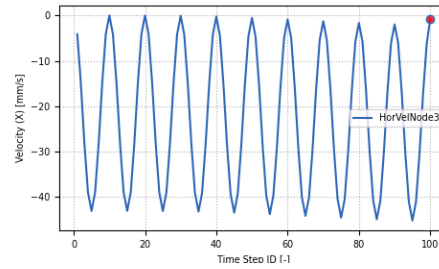
(d) Vertical displacement of Node 6

Figure 3.36: Simulation 1: $k=0.10$

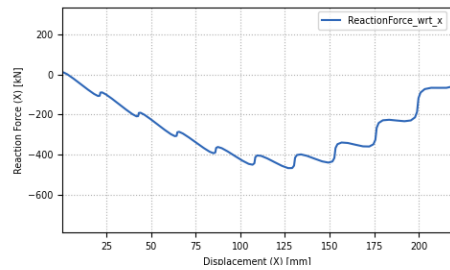
Uniform excitation, Transformation method, $k=0.10$



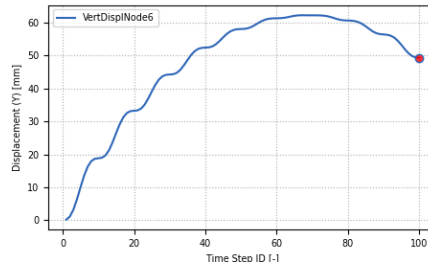
(a) Horizontal displacement of Node 3



(b) Horizontal velocity of Node 3



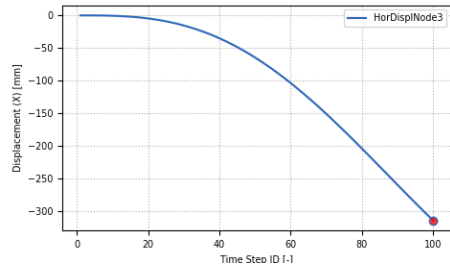
(c) Reaction force vs Displacement of Node 3



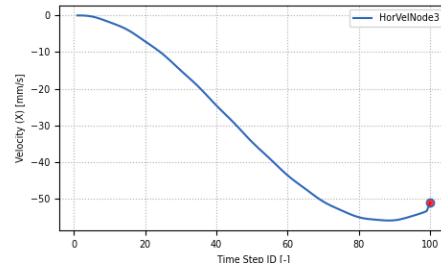
(d) Vertical displacement of Node 6

Figure 3.37: Simulation 1: $k=0.10$

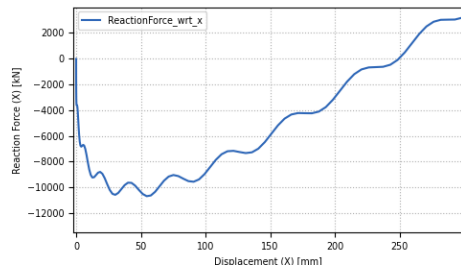
Multi-support excitation, Penalty method, $k=0.10$



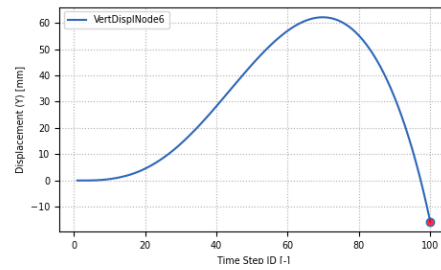
(a) Horizontal displacement of Node 3



(b) Horizontal velocity of Node 3



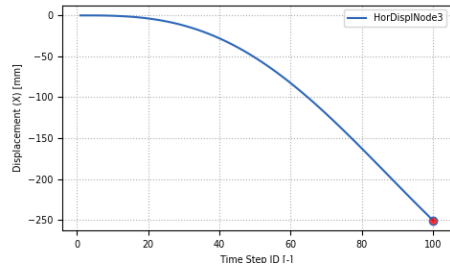
(c) Reaction force vs Displacement of Node 3



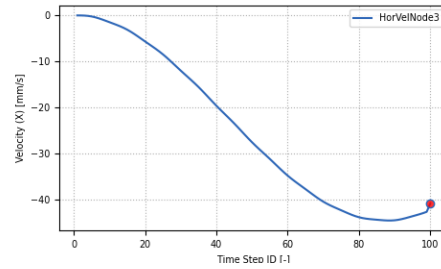
(d) Vertical displacement of Node 6

Figure 3.38: Simulation 1: $k=0.10$

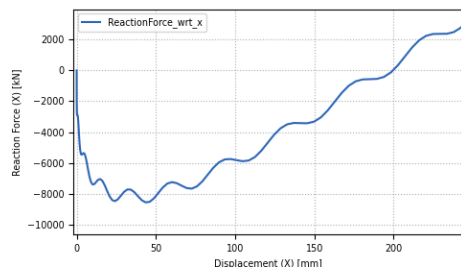
Multi-support excitation, Transformation method, $k=0.10$



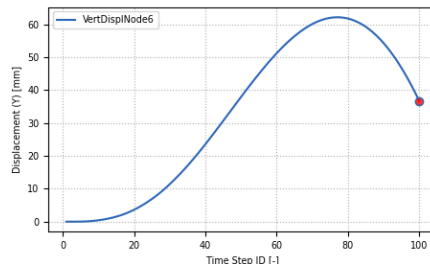
(a) Horizontal displacement of Node 3



(b) Horizontal velocity of Node 3



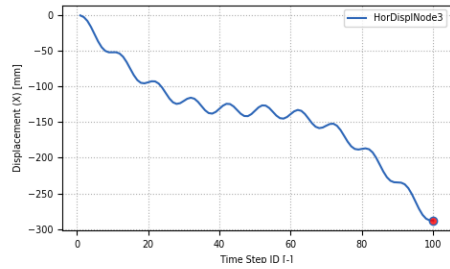
(c) Reaction force vs Displacement of Node 3



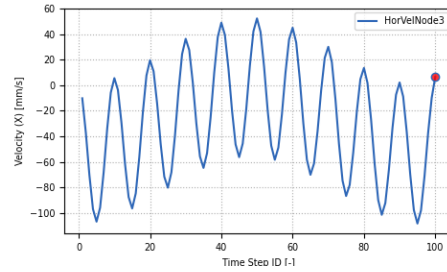
(d) Vertical displacement of Node 6

Figure 3.39: Simulation 1: $k=0.10$

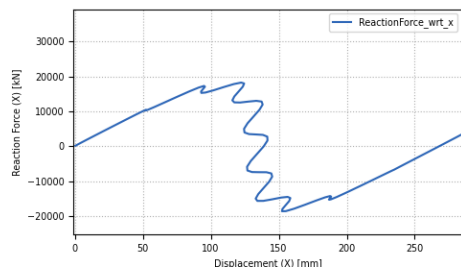
Uniform excitation, Penalty method, $k=0.32$



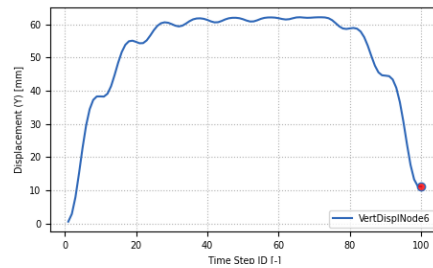
(a) Horizontal displacement of Node 3



(b) Horizontal velocity of Node 3



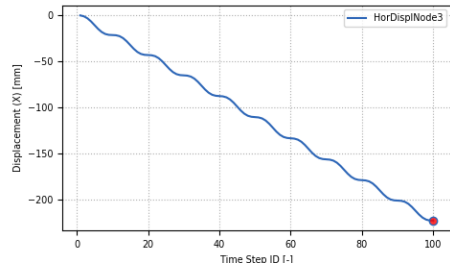
(c) Reaction force vs Displacement of Node 3



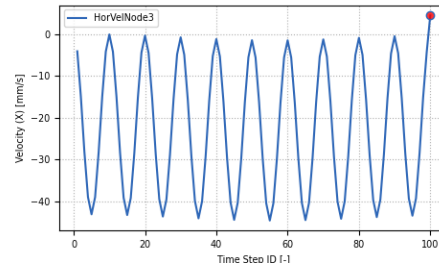
(d) Vertical displacement of Node 6

Figure 3.40: Simulation 1: $k=0.32$

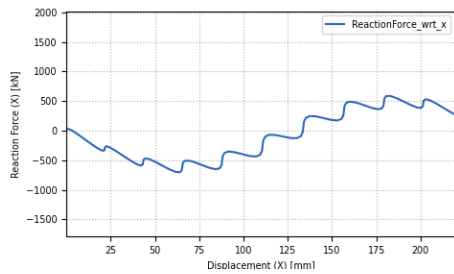
Uniform excitation, Transformation method, $k=0.32$



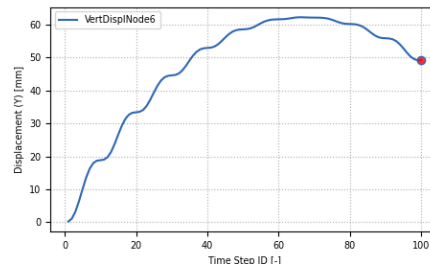
(a) Horizontal displacement of Node 3



(b) Horizontal velocity of Node 3



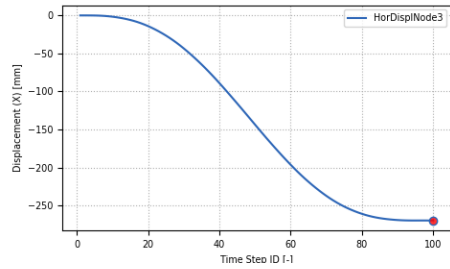
(c) Reaction force vs Displacement of Node 3



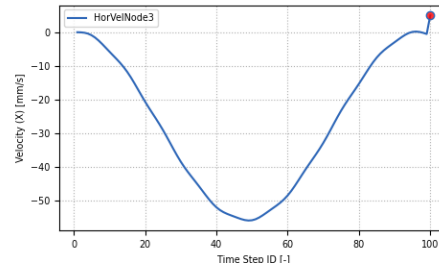
(d) Vertical displacement of Node 6

Figure 3.41: Simulation 1: $k=0.32$

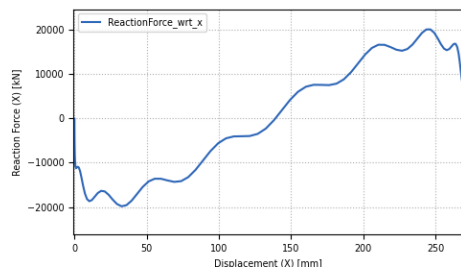
Multi-support excitation, Penalty method, $k=0.32$



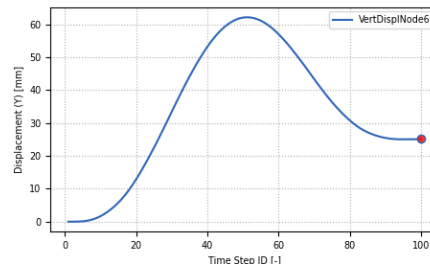
(a) Horizontal displacement of Node 3



(b) Horizontal velocity of Node 3



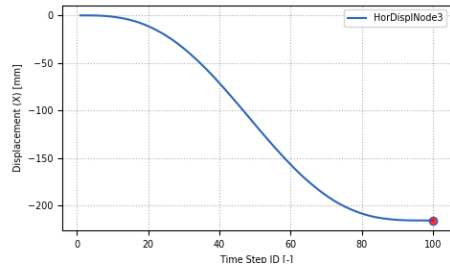
(c) Reaction force vs Displacement of Node 3



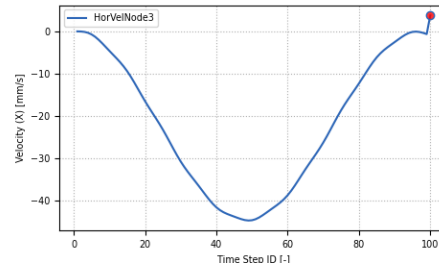
(d) Vertical displacement of Node 6

Figure 3.42: Simulation 1: $k=0.32$

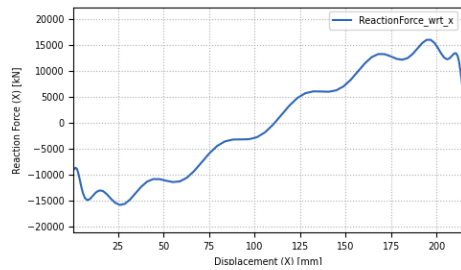
Multi-support excitation, Transformation method, $k=0.32$



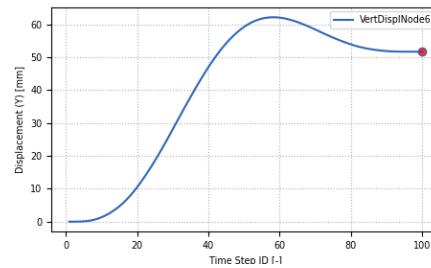
(a) Horizontal displacement of Node 3



(b) Horizontal velocity of Node 3



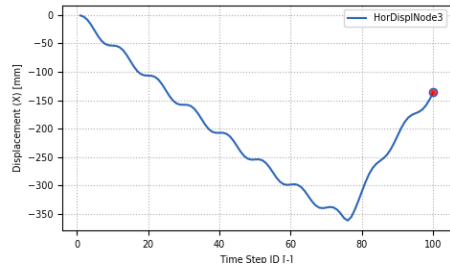
(c) Reaction force vs Displacement of Node 3



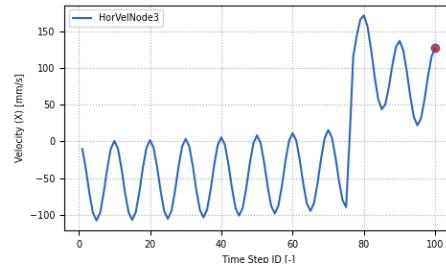
(d) Vertical displacement of Node 6

Figure 3.43: Simulation 1: $k=0.32$

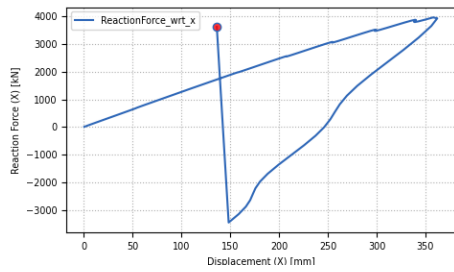
Uniform excitation, Penalty method, $k=0.02$



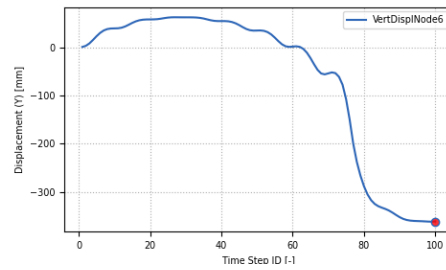
(a) Horizontal displacement of Node 3



(b) Horizontal velocity of Node 3



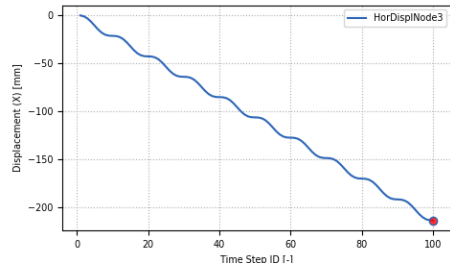
(c) Reaction force vs Displacement of Node 3



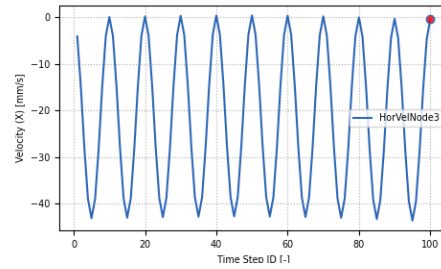
(d) Vertical displacement of Node 6

Figure 3.44: Simulation 2: $k=0.02$

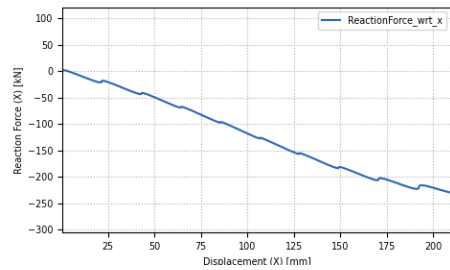
Uniform excitation, Transformation method, $k=0.02$



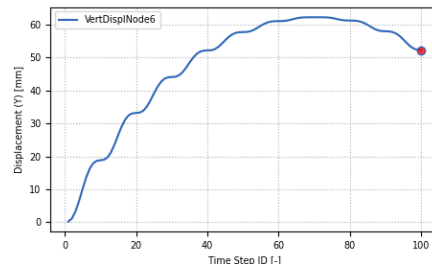
(a) Horizontal displacement of Node 3



(b) Horizontal velocity of Node 3



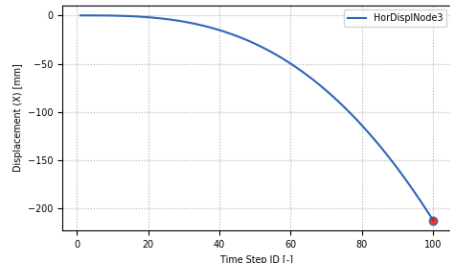
(c) Reaction force vs Displacement of Node 3



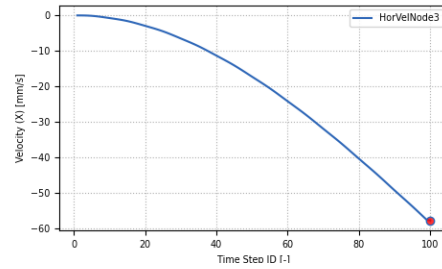
(d) Vertical displacement of Node 6

Figure 3.45: Simulation 2: $k=0.02$

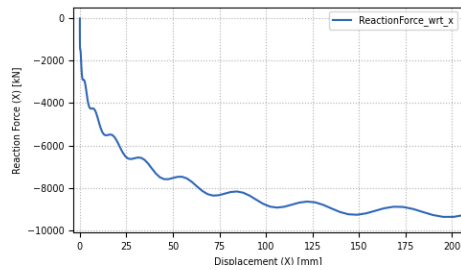
Multi-support excitation, Penalty method, $k=0.02$



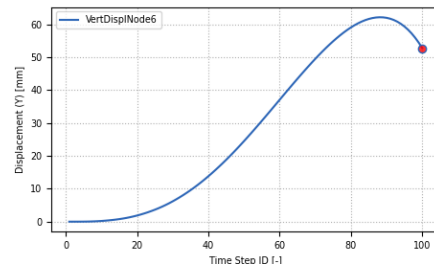
(a) Horizontal displacement of Node 3



(b) Horizontal velocity of Node 3



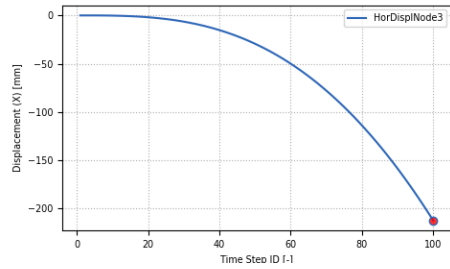
(c) Reaction force vs Displacement of Node 3



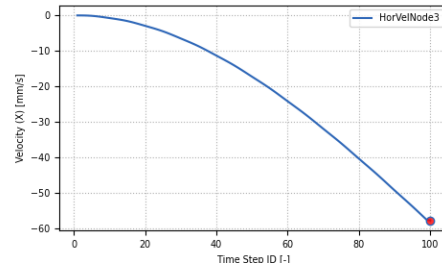
(d) Vertical displacement of Node 6

Figure 3.46: Simulation 2: $k=0.02$

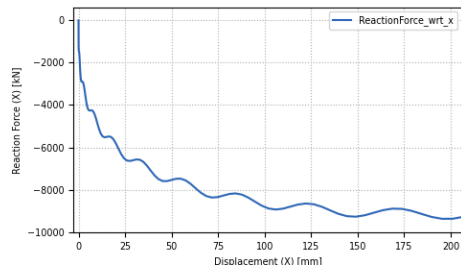
Multi-support excitation, Transformation method, $k=0.02$



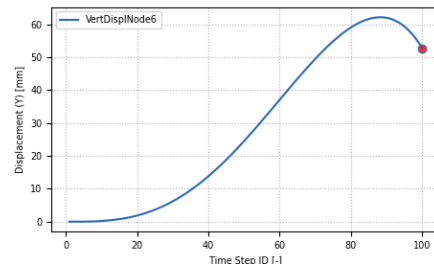
(a) Horizontal displacement of Node 3



(b) Horizontal velocity of Node 3



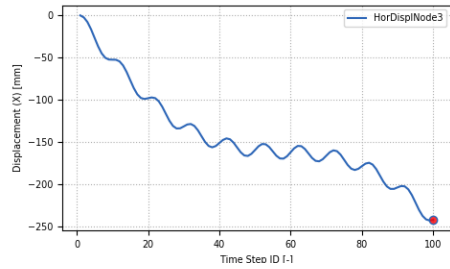
(c) Reaction force vs Displacement of Node 3



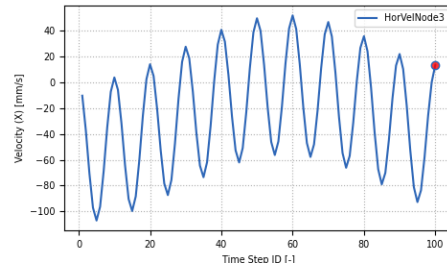
(d) Vertical displacement of Node 6

Figure 3.47: Simulation 2: $k=0.02$

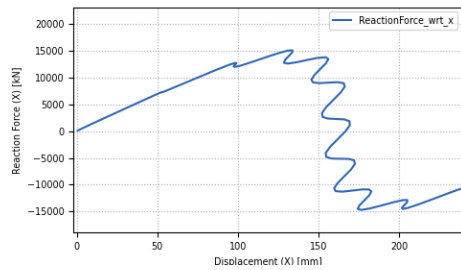
Uniform excitation, Penalty method, $k=0.22$



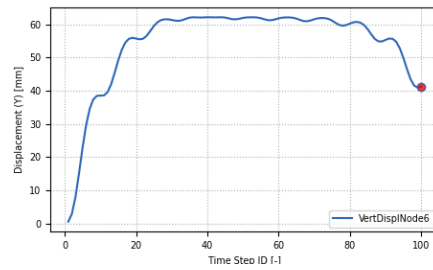
(a) Horizontal displacement of Node 3



(b) Horizontal velocity of Node 3



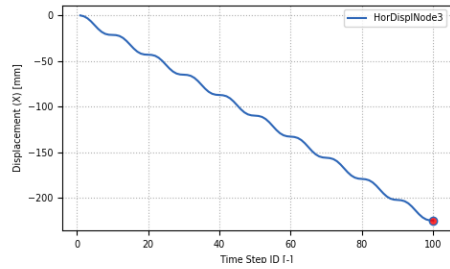
(c) Reaction force vs Displacement of Node 3



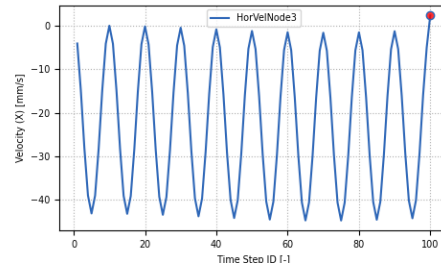
(d) Vertical displacement of Node 6

Figure 3.48: Simulation 2: $k=0.22$

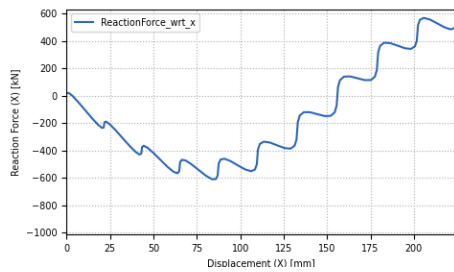
Uniform excitation, Transformation method, $k=0.22$



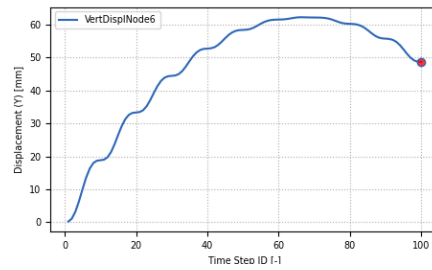
(a) Horizontal displacement of Node 3



(b) Horizontal velocity of Node 3



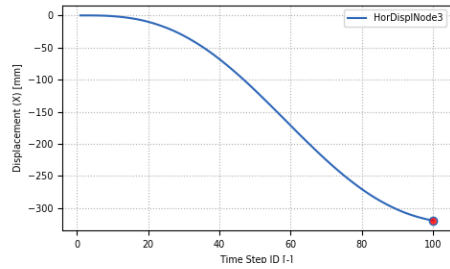
(c) Reaction force vs Displacement of Node 3



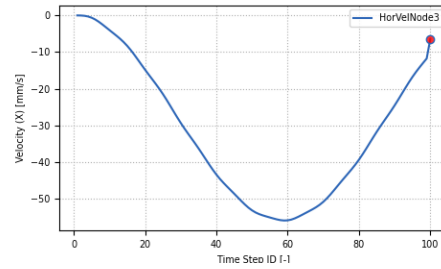
(d) Vertical displacement of Node 6

Figure 3.49: Simulation 2: $k=0.22$

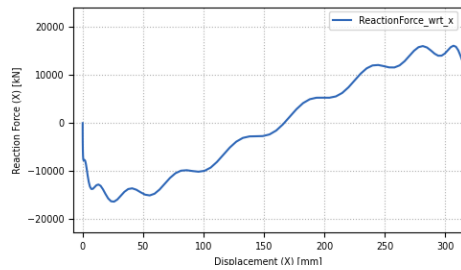
Multi-support excitation, Penalty method, $k=0.22$



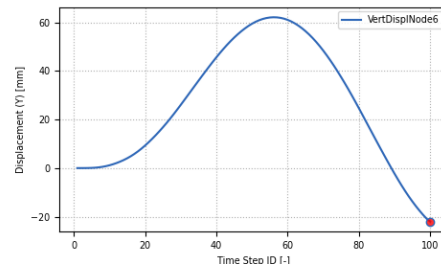
(a) Horizontal displacement of Node 3



(b) Horizontal velocity of Node 3



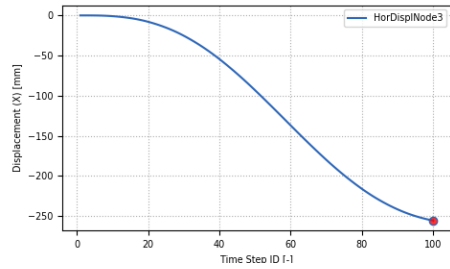
(c) Reaction force vs Displacement of Node 3



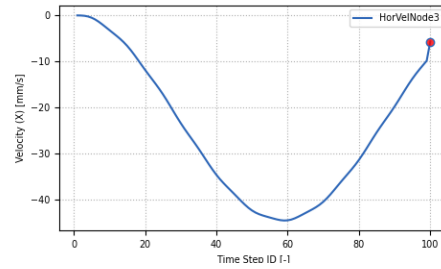
(d) Vertical displacement of Node 6

Figure 3.50: Simulation 2: $k=0.22$

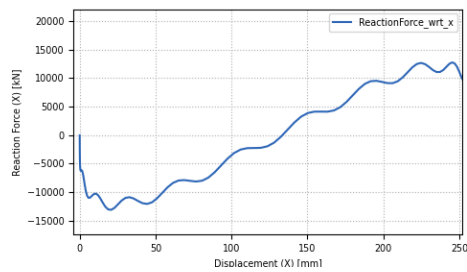
Multi-support excitation, Transformation method, $k=0.22$



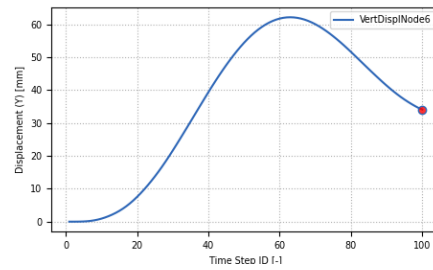
(a) Horizontal displacement of Node 3



(b) Horizontal velocity of Node 3



(c) Reaction force vs Displacement of Node 3

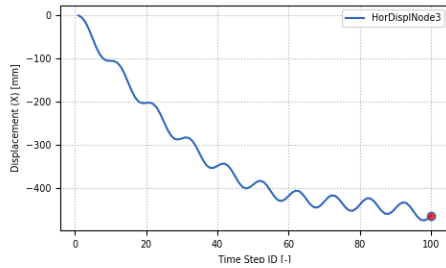


(d) Vertical displacement of Node 6

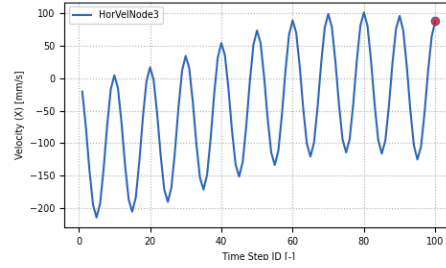
Figure 3.51: Simulation 2: $k=0.22$

3.2.3 $\theta_0 = 65^\circ$

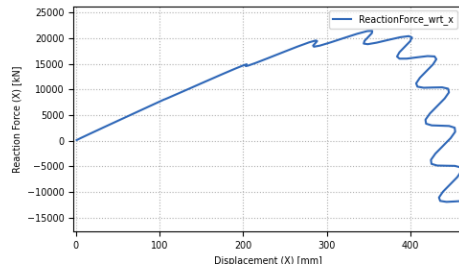
Uniform excitation, Penalty method, $k=0.12$



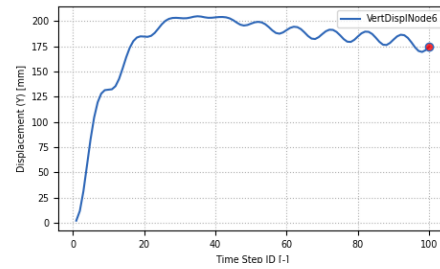
(a) Horizontal displacement of Node 3



(b) Horizontal velocity of Node 3



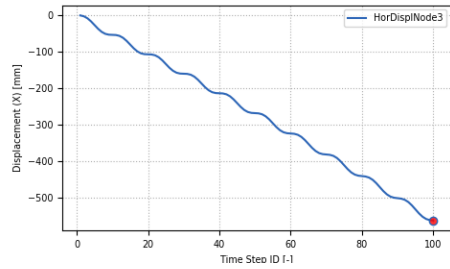
(c) Reaction force vs Displacement of Node 3



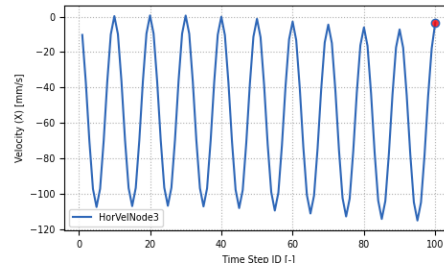
(d) Vertical displacement of Node 6

Figure 3.52: Simulation 3: $k=0.12$

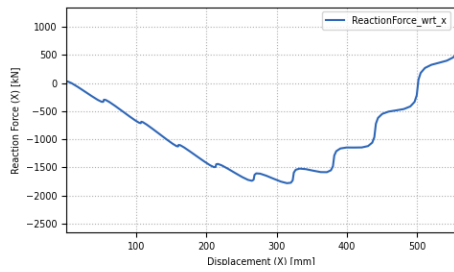
Uniform excitation, Transformation method, $k=0.12$



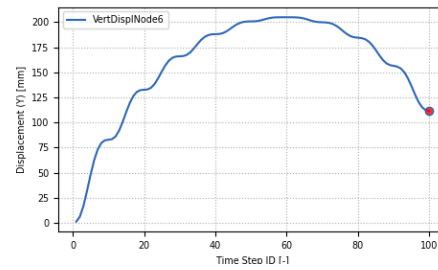
(a) Horizontal displacement of Node 3



(b) Horizontal velocity of Node 3



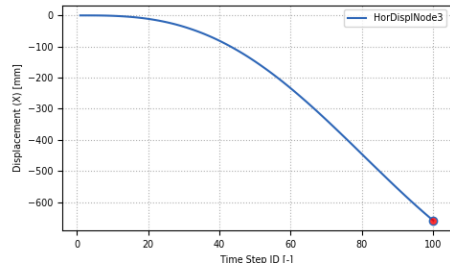
(c) Reaction force vs Displacement of Node 3



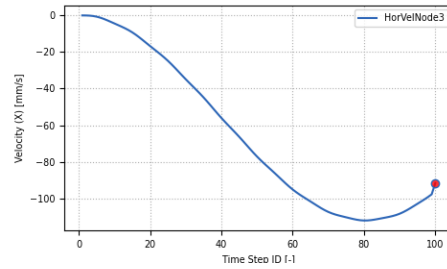
(d) Vertical displacement of Node 6

Figure 3.53: Simulation 3: $k=0.12$

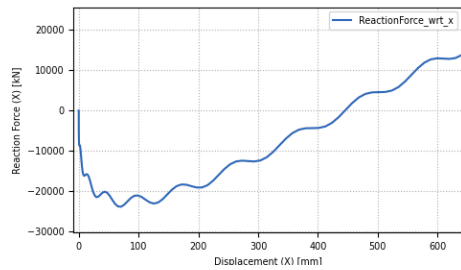
Multi-support excitation, Penalty method, $k=0.12$



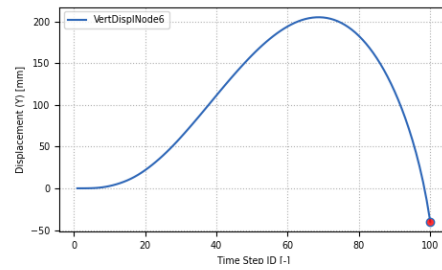
(a) Horizontal displacement of Node 3



(b) Horizontal velocity of Node 3



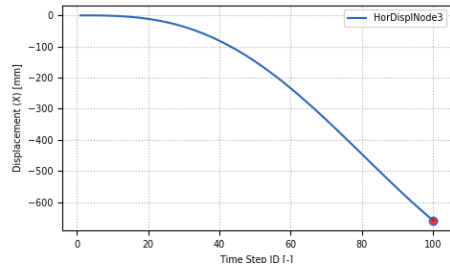
(c) Reaction force vs Displacement of Node 3



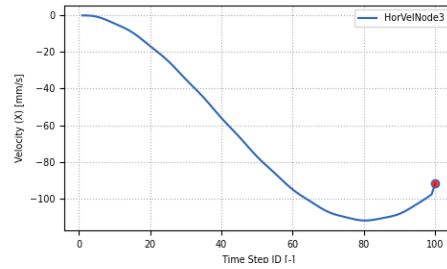
(d) Vertical displacement of Node 6

Figure 3.54: Simulation 3: $k=0.12$

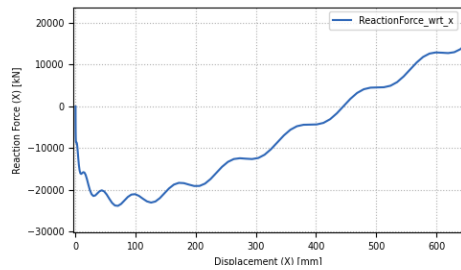
Multi-support excitation, Transformation method, $k=0.12$



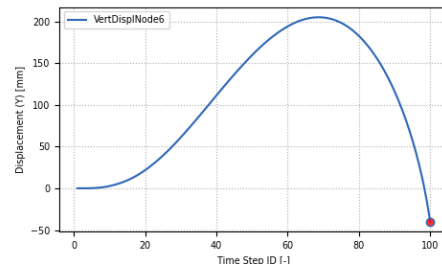
(a) Horizontal displacement of Node 3



(b) Horizontal velocity of Node 3



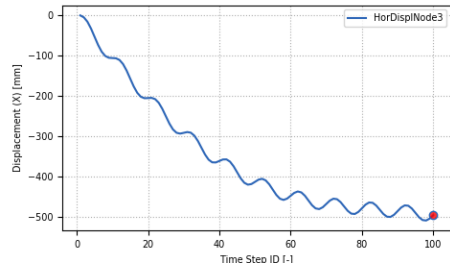
(c) Reaction force vs Displacement of Node 3



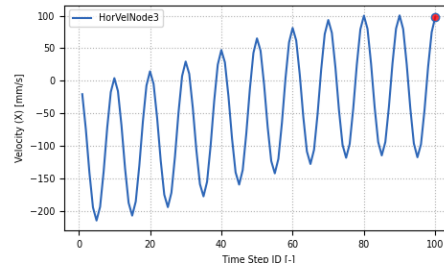
(d) Vertical displacement of Node 6

Figure 3.55: Simulation 3: $k=0.12$

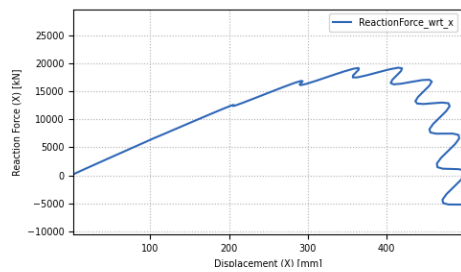
Uniform excitation, Penalty method, $k=0.10$



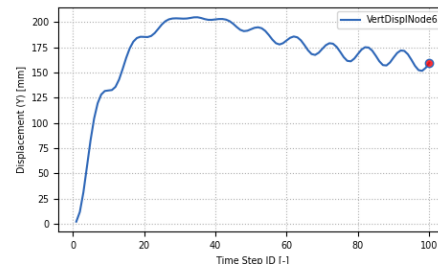
(a) Horizontal displacement of Node 3



(b) Horizontal velocity of Node 3



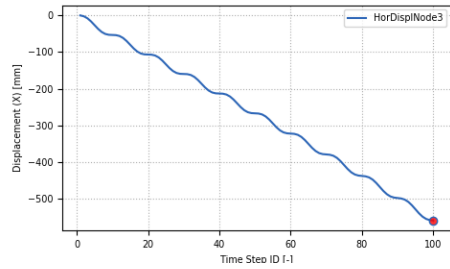
(c) Reaction force vs Displacement of Node 3



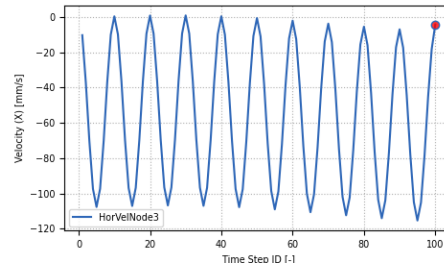
(d) Vertical displacement of Node 6

Figure 3.56: Simulation 3: $k=0.10$

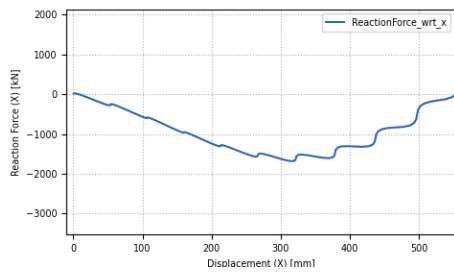
Uniform excitation, Transformation method, $k=0.10$



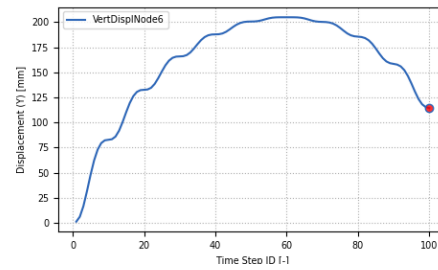
(a) Horizontal displacement of Node 3



(b) Horizontal velocity of Node 3



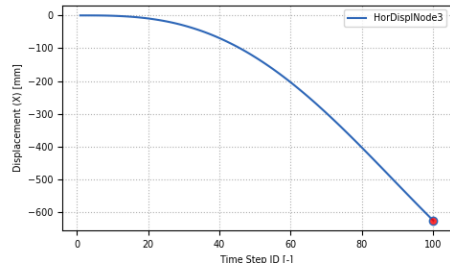
(c) Reaction force vs Displacement of Node 3



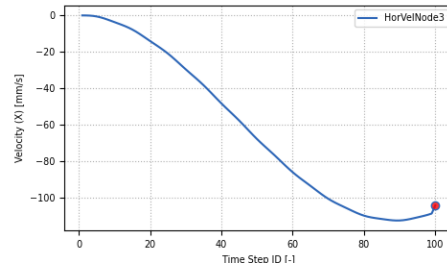
(d) Vertical displacement of Node 6

Figure 3.57: Simulation 3: $k=0.10$

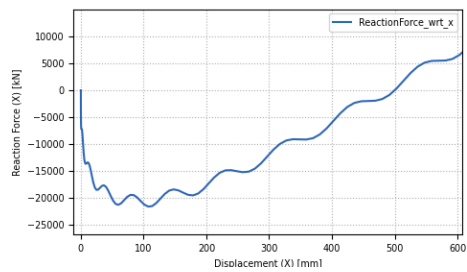
Multi-support excitation, Penalty method, $k=0.10$



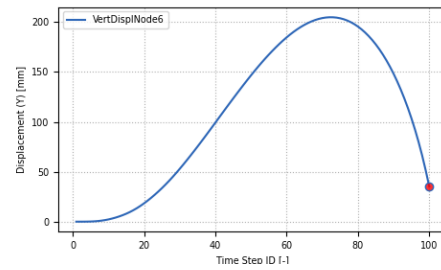
(a) Horizontal displacement of Node 3



(b) Horizontal velocity of Node 3



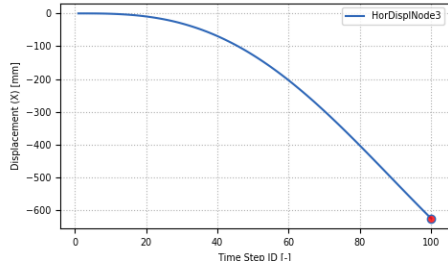
(c) Reaction force vs Displacement of Node 3



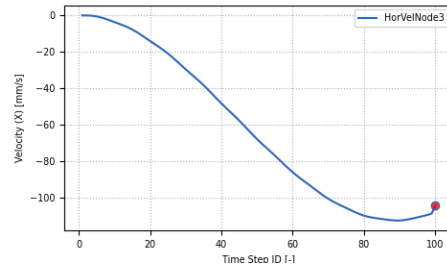
(d) Vertical displacement of Node 6

Figure 3.58: Simulation 3: $k=0.10$

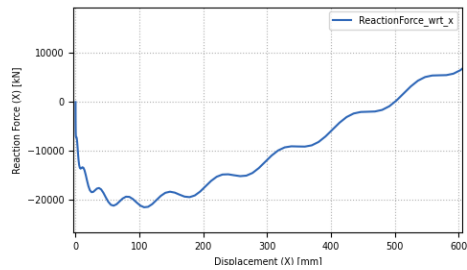
Multi-support excitation, Transformation method, $k=0.10$



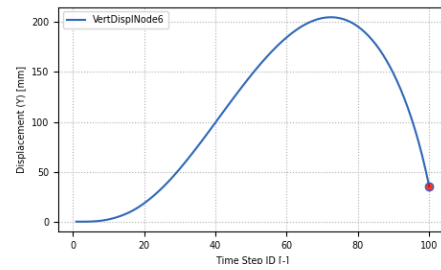
(a) Horizontal displacement of Node 3



(b) Horizontal velocity of Node 3



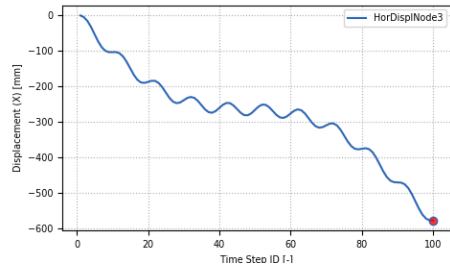
(c) Reaction force vs Displacement of Node 3



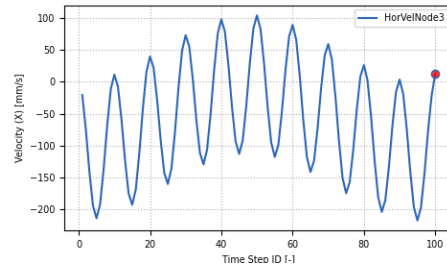
(d) Vertical displacement of Node 6

Figure 3.59: Simulation 3: $k=0.10$

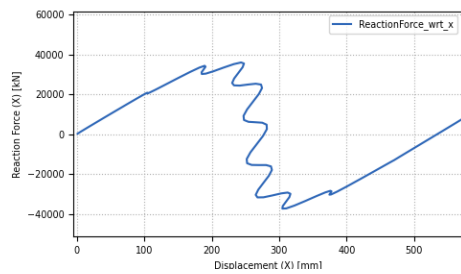
Uniform excitation, Penalty method, $k=0.32$



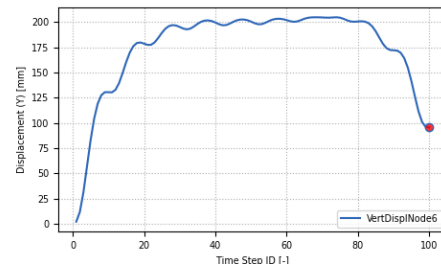
(a) Horizontal displacement of Node 3



(b) Horizontal velocity of Node 3



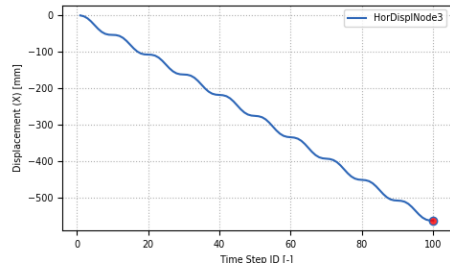
(c) Reaction force vs Displacement of Node 3



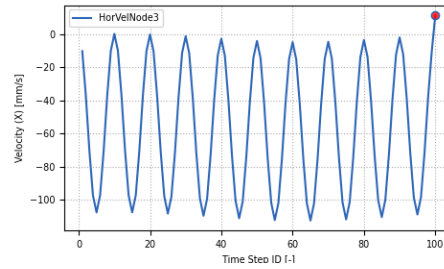
(d) Vertical displacement of Node 6

Figure 3.60: Simulation 3: $k=0.32$

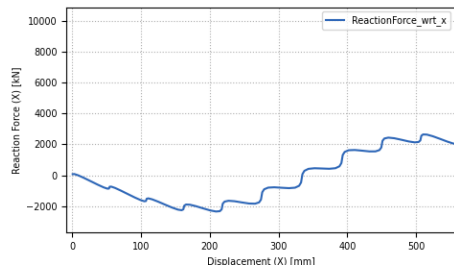
Uniform excitation, Transformation method, $k=0.32$



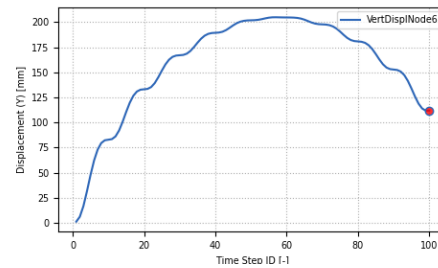
(a) Horizontal displacement of Node 3



(b) Horizontal velocity of Node 3



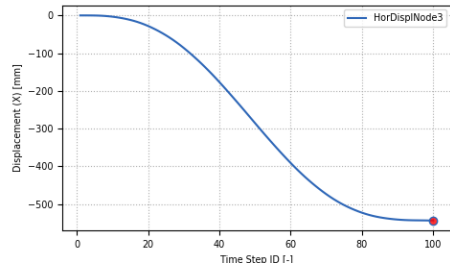
(c) Reaction force vs Displacement of Node 3



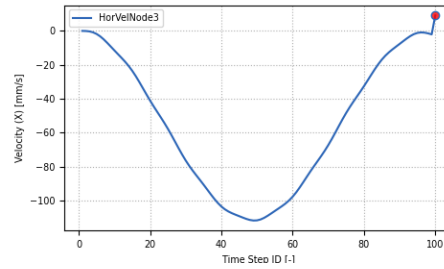
(d) Vertical displacement of Node 6

Figure 3.61: Simulation 3: $k=0.32$

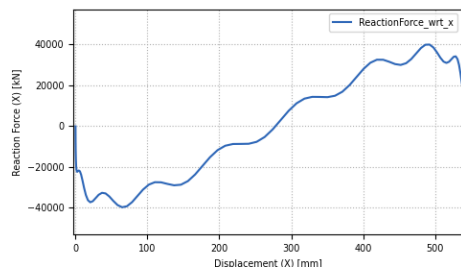
Multi-support excitation, Penalty method, $k=0.32$



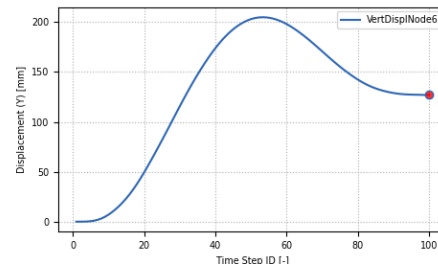
(a) Horizontal displacement of Node 3



(b) Horizontal velocity of Node 3



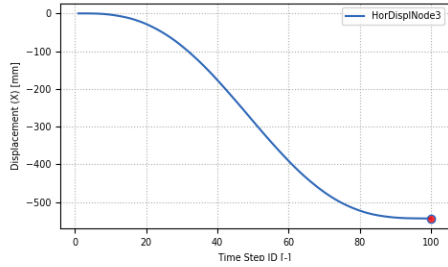
(c) Reaction force vs Displacement of Node 3



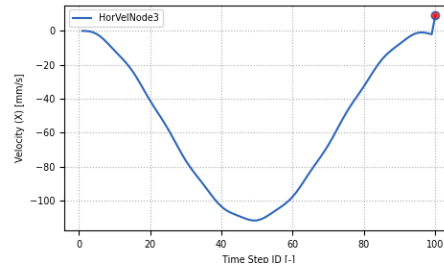
(d) Vertical displacement of Node 6

Figure 3.62: Simulation 3: $k=0.32$

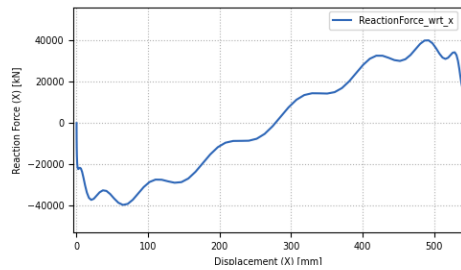
Multi-support excitation, Transformation method, $k=0.32$



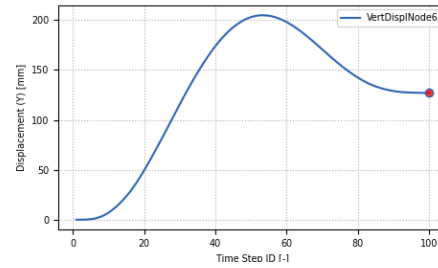
(a) Horizontal displacement of Node 3



(b) Horizontal velocity of Node 3



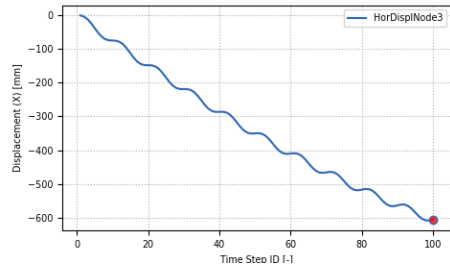
(c) Reaction force vs Displacement of Node 3



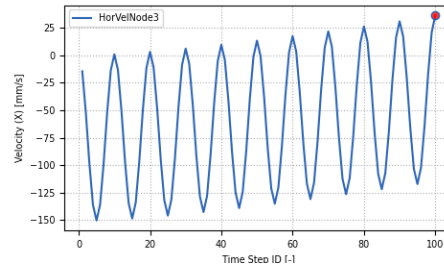
(d) Vertical displacement of Node 6

Figure 3.63: Simulation 3: $k=0.32$

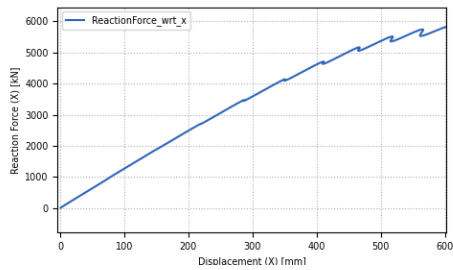
Uniform excitation, Penalty method, $k=0.02$



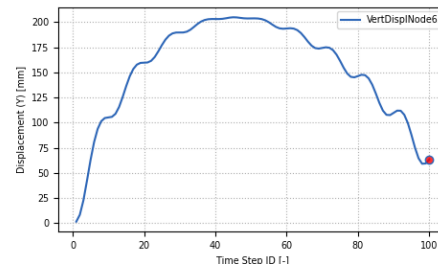
(a) Horizontal displacement of Node 3



(b) Horizontal velocity of Node 3



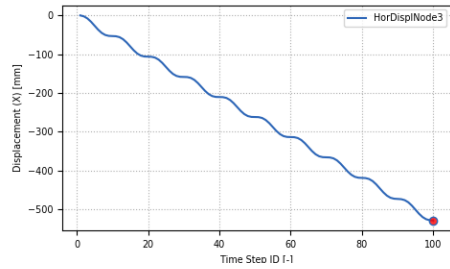
(c) Reaction force vs Displacement of Node 3



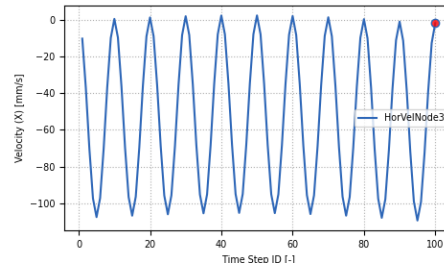
(d) Vertical displacement of Node 6

Figure 3.64: Simulation 3: $k=0.02$

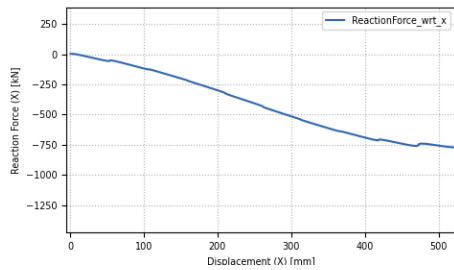
Uniform excitation, Transformation method, $k=0.02$



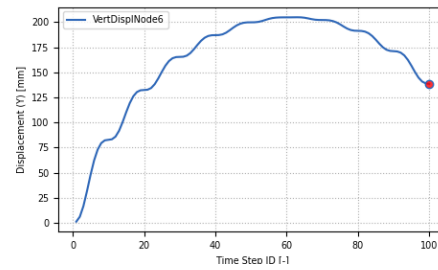
(a) Horizontal displacement of Node 3



(b) Horizontal velocity of Node 3



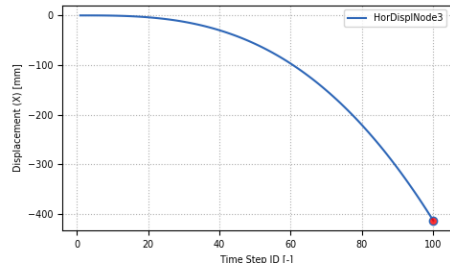
(c) Reaction force vs Displacement of Node 3



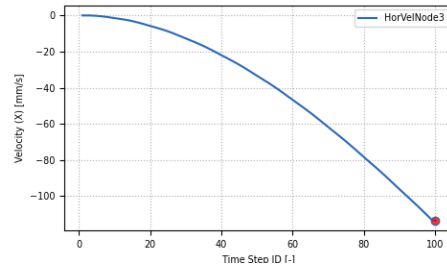
(d) Vertical displacement of Node 6

Figure 3.65: Simulation 3: $k=0.02$

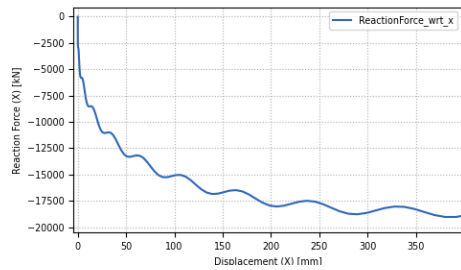
Multi-support excitation, Penalty method, $k=0.02$



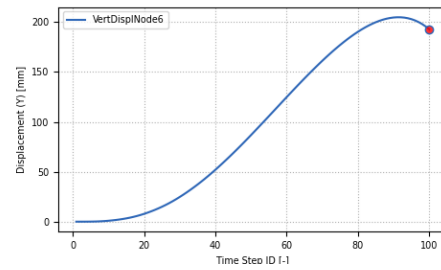
(a) Horizontal displacement of Node 3



(b) Horizontal velocity of Node 3



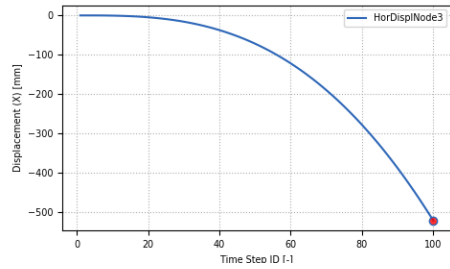
(c) Reaction force vs Displacement of Node 3



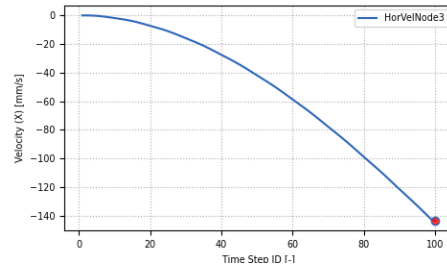
(d) Vertical displacement of Node 6

Figure 3.66: Simulation 3: $k=0.02$

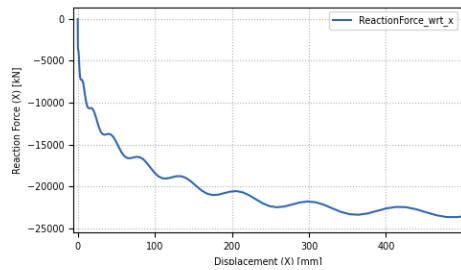
Multi-support excitation, Transformation method, $k=0.02$



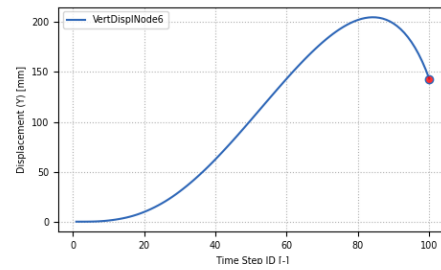
(a) Horizontal displacement of Node 3



(b) Horizontal velocity of Node 3



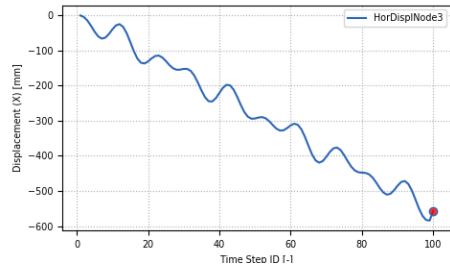
(c) Reaction force vs Displacement of Node 3



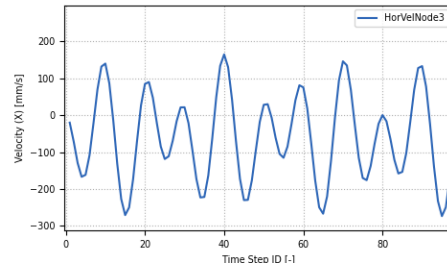
(d) Vertical displacement of Node 6

Figure 3.67: Simulation 3: $k=0.02$

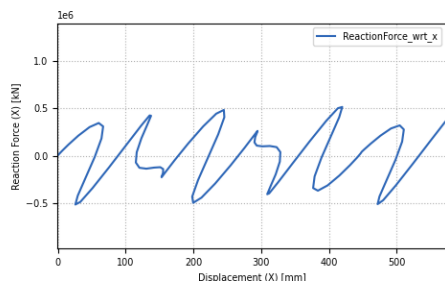
Uniform excitation, Penalty method, $k=0.22$



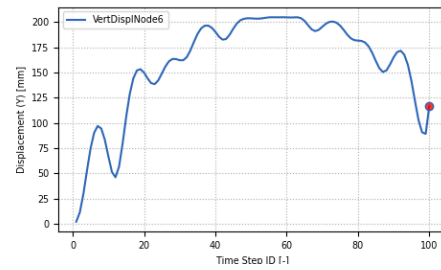
(a) Horizontal displacement of Node 3



(b) Horizontal velocity of Node 3



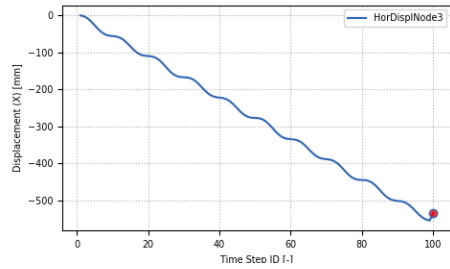
(c) Reaction force vs Displacement of Node 3



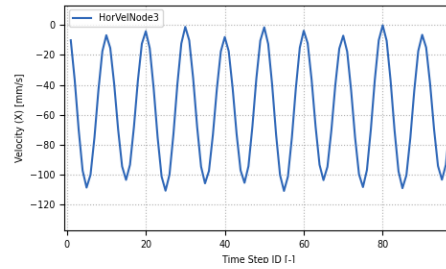
(d) Vertical displacement of Node 6

Figure 3.68: Simulation 3: $k=0.22$

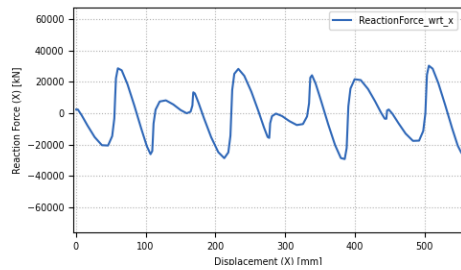
Uniform excitation, Transformation method, $k=0.22$



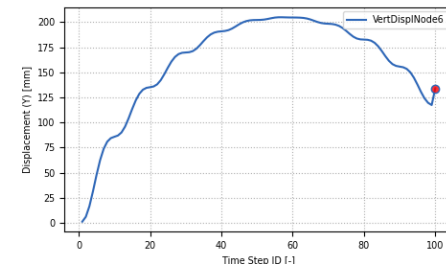
(a) Horizontal displacement of Node 3



(b) Horizontal velocity of Node 3



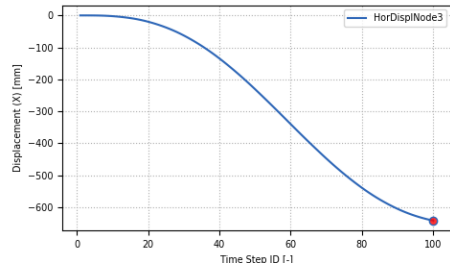
(c) Reaction force vs Displacement of Node 3



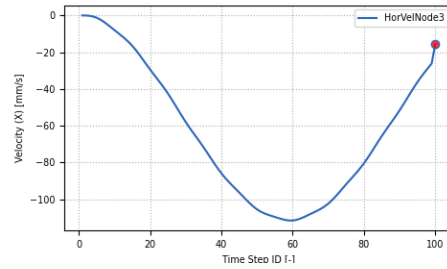
(d) Vertical displacement of Node 6

Figure 3.69: Simulation 3: $k=0.22$

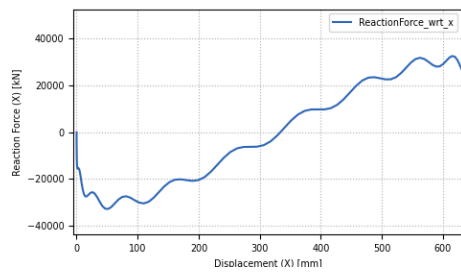
Multi-support excitation, Penalty method, $k=0.22$



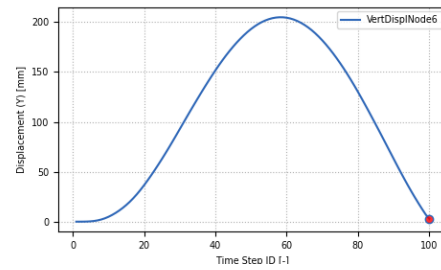
(a) Horizontal displacement of Node 3



(b) Horizontal velocity of Node 3



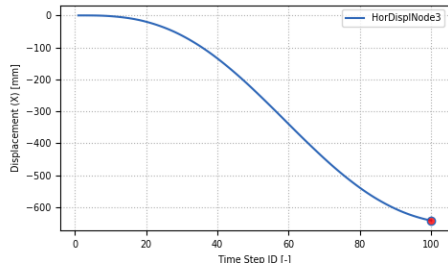
(c) Reaction force vs Displacement of Node 3



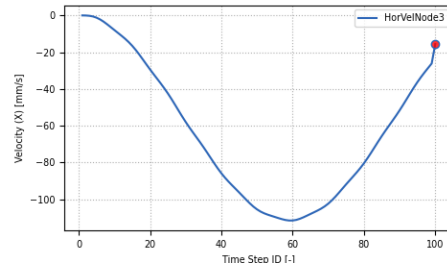
(d) Vertical displacement of Node 6

Figure 3.70: Simulation 3: $k=0.22$

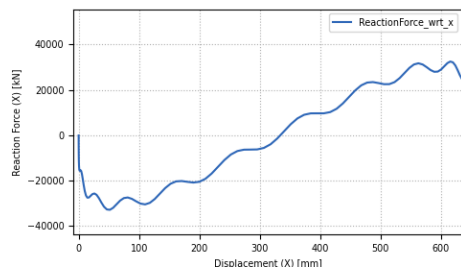
Multi-support excitation, Transformation method, $k=0.22$



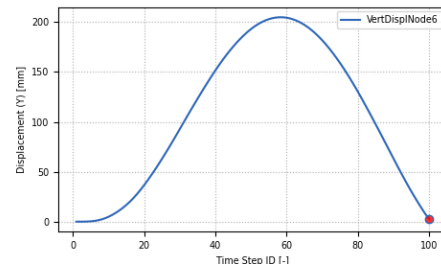
(a) Horizontal displacement of Node 3



(b) Horizontal velocity of Node 3



(c) Reaction force vs Displacement of Node 3

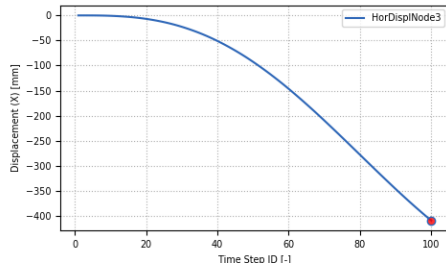


(d) Vertical displacement of Node 6

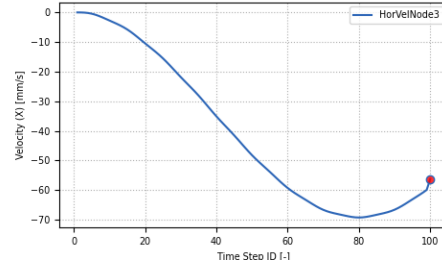
Figure 3.71: Simulation 3: $k=0.22$

3.2.4 $\theta_0 = 55^\circ$

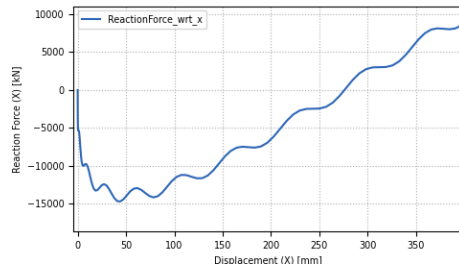
Multi-support excitation, Transformation method, $k=0.12$



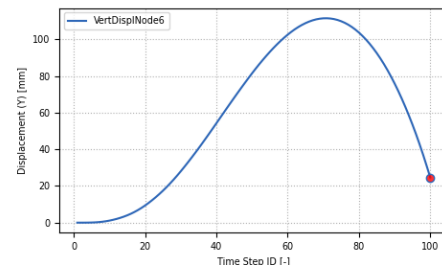
(a) Horizontal displacement of Node 3



(b) Horizontal velocity of Node 3



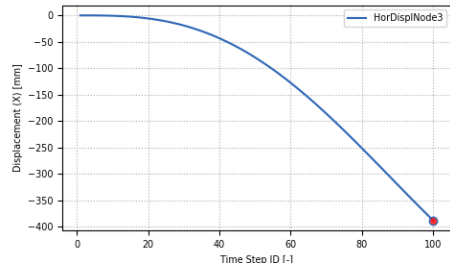
(c) Reaction force vs Displacement of Node 3



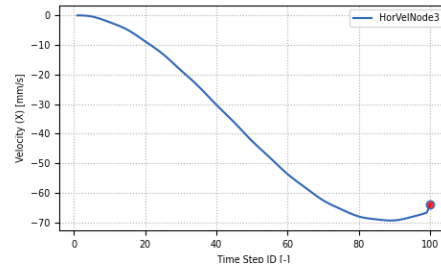
(d) Vertical displacement of Node 6

Figure 3.72: Simulation 4: $k=0.12$

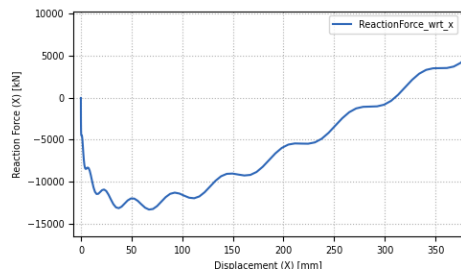
Multi-support excitation, Transformation method, $k=0.10$



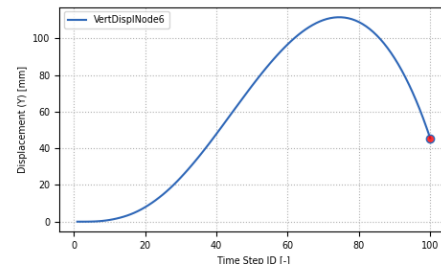
(a) Horizontal displacement of Node 3



(b) Horizontal velocity of Node 3



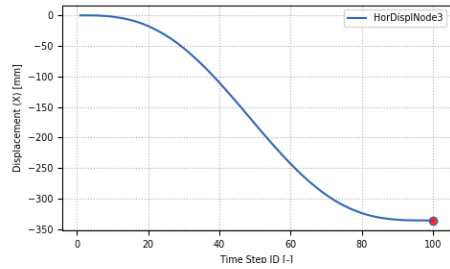
(c) Reaction force vs Displacement of Node 3



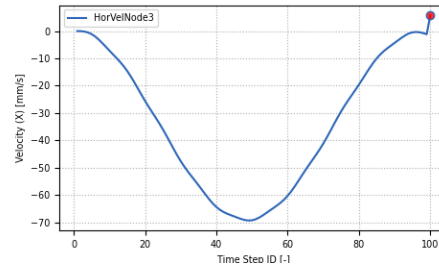
(d) Vertical displacement of Node 6

Figure 3.73: Simulation 4: $k=0.10$

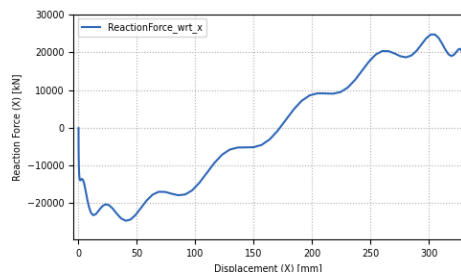
Multi-support excitation, Transformation method, $k=0.32$



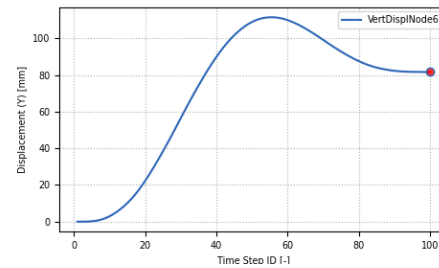
(a) Horizontal displacement of Node 3



(b) Horizontal velocity of Node 3



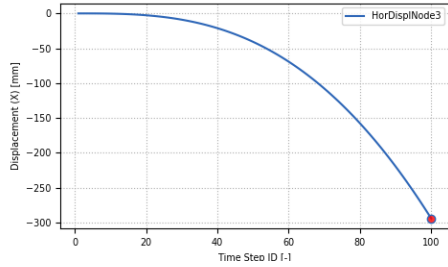
(c) Reaction force vs Displacement of Node 3



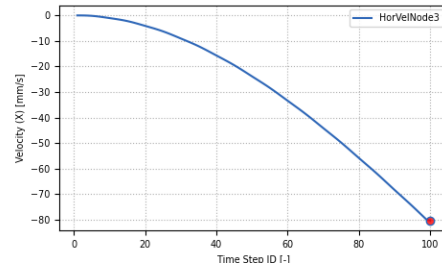
(d) Vertical displacement of Node 6

Figure 3.74: Simulation 4: $k=0.32$

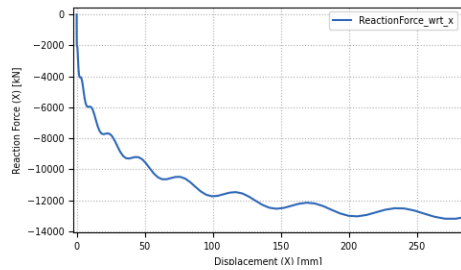
Multi-support excitation, Transformation method, $k=0.02$



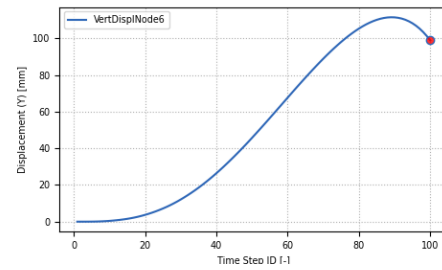
(a) Horizontal displacement of Node 3



(b) Horizontal velocity of Node 3



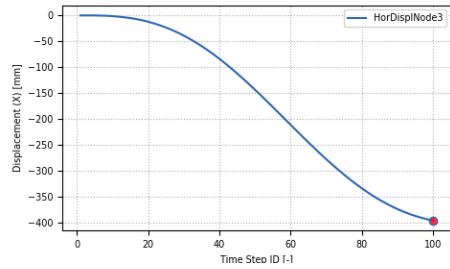
(c) Reaction force vs Displacement of Node 3



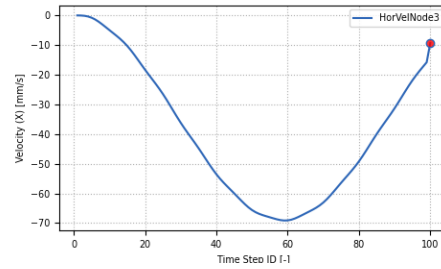
(d) Vertical displacement of Node 6

Figure 3.75: Simulation 4: $k=0.02$

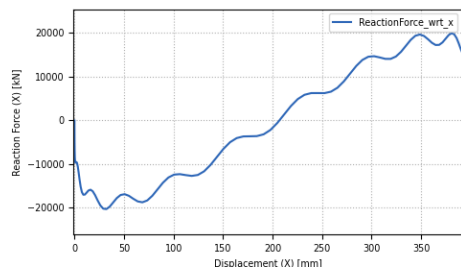
Multi-support excitation, Transformation method, $k=0.22$



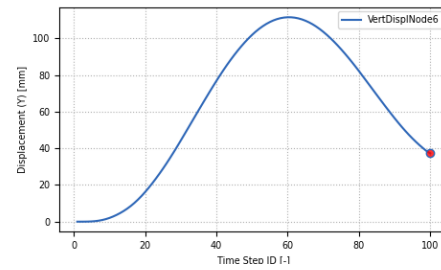
(a) Horizontal displacement of Node 3



(b) Horizontal velocity of Node 3



(c) Reaction force vs Displacement of Node 3

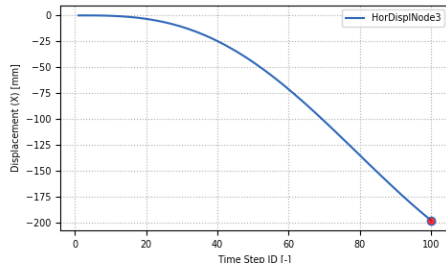


(d) Vertical displacement of Node 6

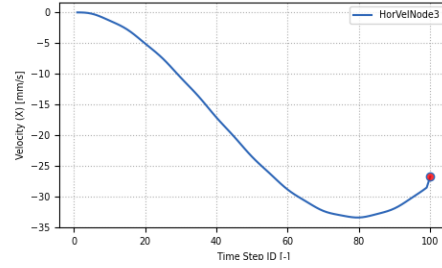
Figure 3.76: Simulation 4: $k=0.22$

3.2.5 $\theta_0 = 37.5^\circ$

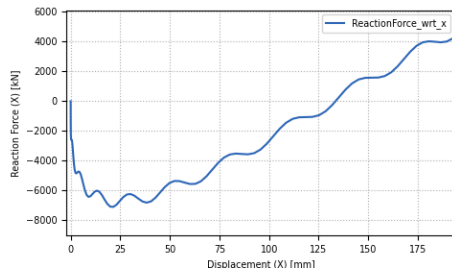
Multi-support excitation, Transformation method, $k=0.12$



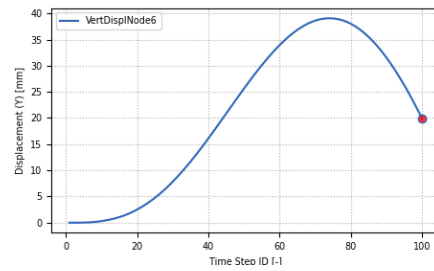
(a) Horizontal displacement of Node 3



(b) Horizontal velocity of Node 3



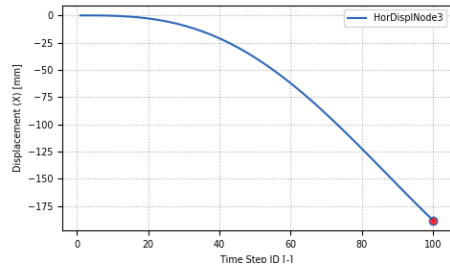
(c) Reaction force vs Displacement of Node 3



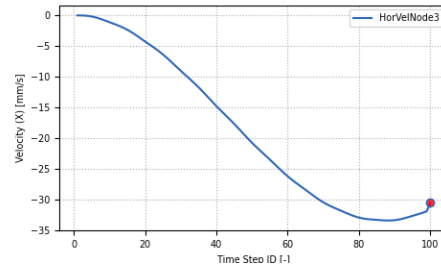
(d) Vertical displacement of Node 6

Figure 3.77: Simulation 5: $k=0.12$

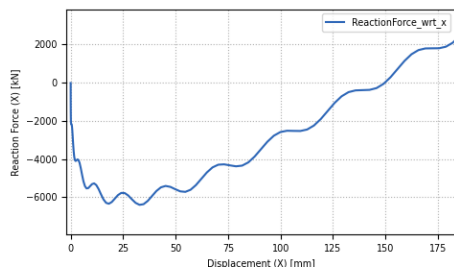
Multi-support excitation, Transformation method, $k=0.10$



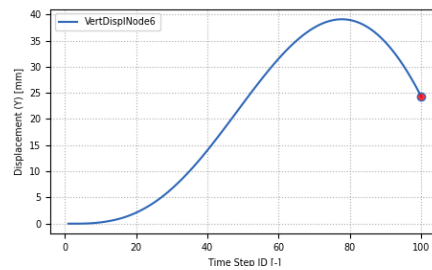
(a) Horizontal displacement of Node 3



(b) Horizontal velocity of Node 3



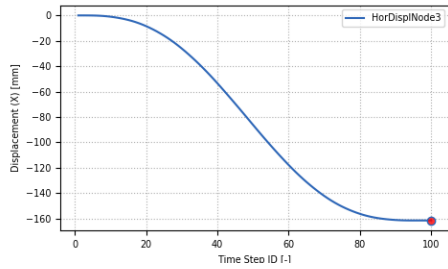
(c) Reaction force vs Displacement of Node 3



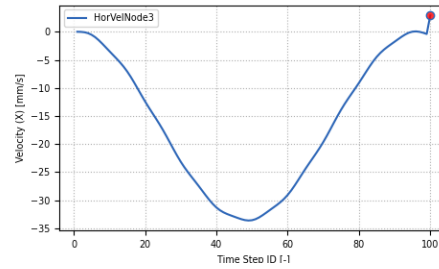
(d) Vertical displacement of Node 6

Figure 3.78: Simulation 5: $k=0.10$

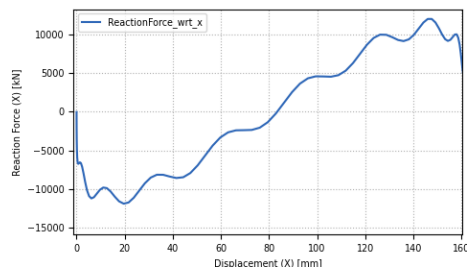
Multi-support excitation, Transformation method, $k=0.32$



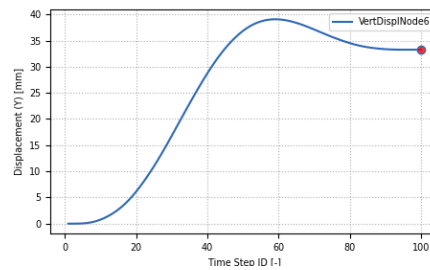
(a) Horizontal displacement of Node 3



(b) Horizontal velocity of Node 3



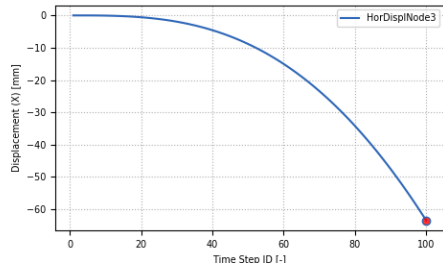
(c) Reaction force vs Displacement of Node 3



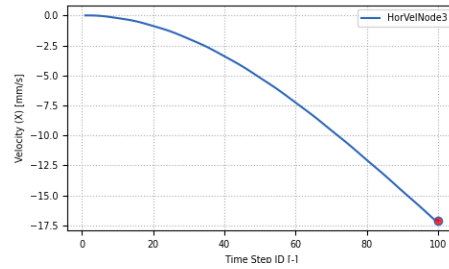
(d) Vertical displacement of Node 6

Figure 3.79: Simulation 5: $k=0.32$

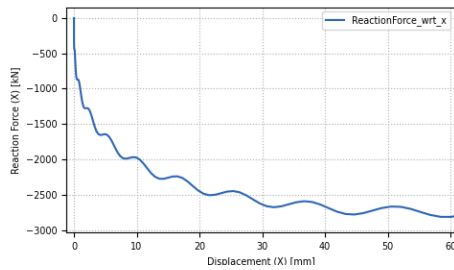
Multi-support excitation, Transformation method, $k=0.02$



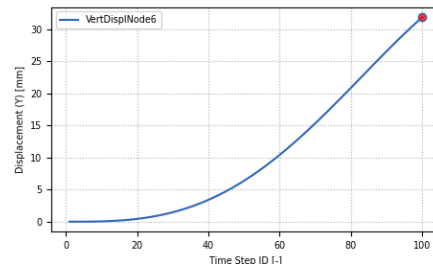
(a) Horizontal displacement of Node 3



(b) Horizontal velocity of Node 3



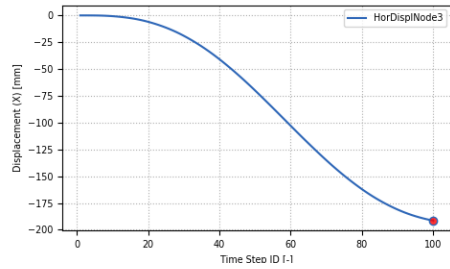
(c) Reaction force vs Displacement of Node 3



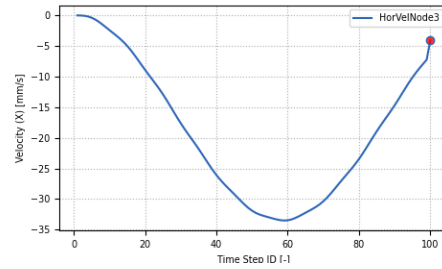
(d) Vertical displacement of Node 6

Figure 3.80: Simulation 5: $k=0.02$

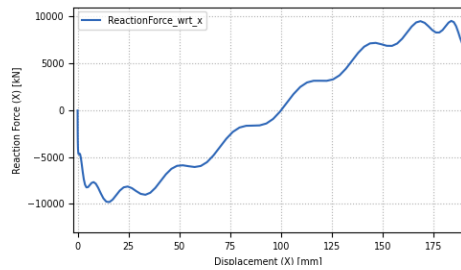
Multi-support excitation, Transformation method, $k=0.22$



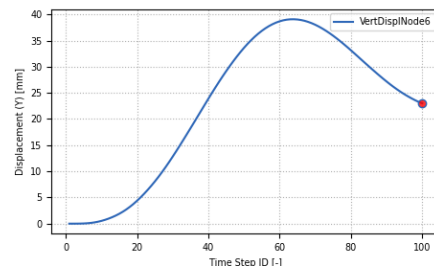
(a) Horizontal displacement of Node 3



(b) Horizontal velocity of Node 3



(c) Reaction force vs Displacement of Node 3



(d) Vertical displacement of Node 6

Figure 3.81: Simulation 5: $k=0.22$

3.3 Conclusions

After performing the above-mentioned parametric analysis ([section 3.2](#)), in order to proceed with the investigation, it is necessary to individuate the best combination of *design parameters* (k, θ_0).

Before making the decision, several considerations were taken into account, including the preference for the "Transformation method" over the "Penalty method" and the "Multi-support excitation" over the "Uniform excitation". These choices were made because, for this particular problem, they are better suited to the task at hand (for example, the Transformation method offers greater numerical stability, especially in the case of non-linear behaviour of the damper). This also helps to explain the reduced number of simulations in the last two cases, as only these two parameters were considered.

The couple ($k = 0.12, \theta_0 = 45^\circ$) is the one with whom the investigation will continue.

The selection of this pair is based on the observation of the behaviour depicted in the previous graphs. One of the reasons was the behaviour of the vertical displacement at the node, which in some cases tended toward a horizontal asymptote. Furthermore, it was decided not to proceed with excessively large angles because, given that the length of the hinged bars (" L_b ") depends on them, such angles would have imposed considerably greater stress on the flappers, as node 6 would have experienced larger vertical displacements.

Chapter 4

Study of a steel frame with a tristable brace

Building on the comprehensive analysis presented in Chapter 3, this chapter extends the investigation by integrating a tristable brace into a steel frame structure. In Chapter 3, the groundwork was established through the development of a robust numerical model and the extraction of the optimal combination of design parameters. This critical step provided the necessary basis for further exploration of more complex structural systems.

As discussed in Section 1.3.3 of Chapter 1, a tristable brace can be derived by composing two bistable elements, whereby one element is the mirror image of the other. The only distinction between the two lies in their initial angles, with one of the angles being defined as $(\pi - \theta_0)$. This mirroring process enables the creation of a tristable system that offers a symmetric response under both tensile and compressive loads, a feature particularly advantageous for seismic applications.

In the present chapter, the derived tristable element is subsequently incorporated into a steel frame. The focus is on evaluating the dynamic response of the frame, analysing its energy dissipation capabilities, and assessing its potential to enhance seismic resilience. By coupling the advanced modelling techniques developed in Chapter 3 with the practical considerations of steel frame design, this chapter aims to demonstrate how the integration of a

tristable brace can lead to significant improvements in structural performance under dynamic loading conditions, comparing the latter to the steel frame response in absence of the tristable brace.

4.1 Development of the numerical model with OpenSees

Considering what was discussed in Chapter 3.3, and keeping in mind the information presented at the beginning of this chapter (4), the study proceeds with the development of the tristable brace element.

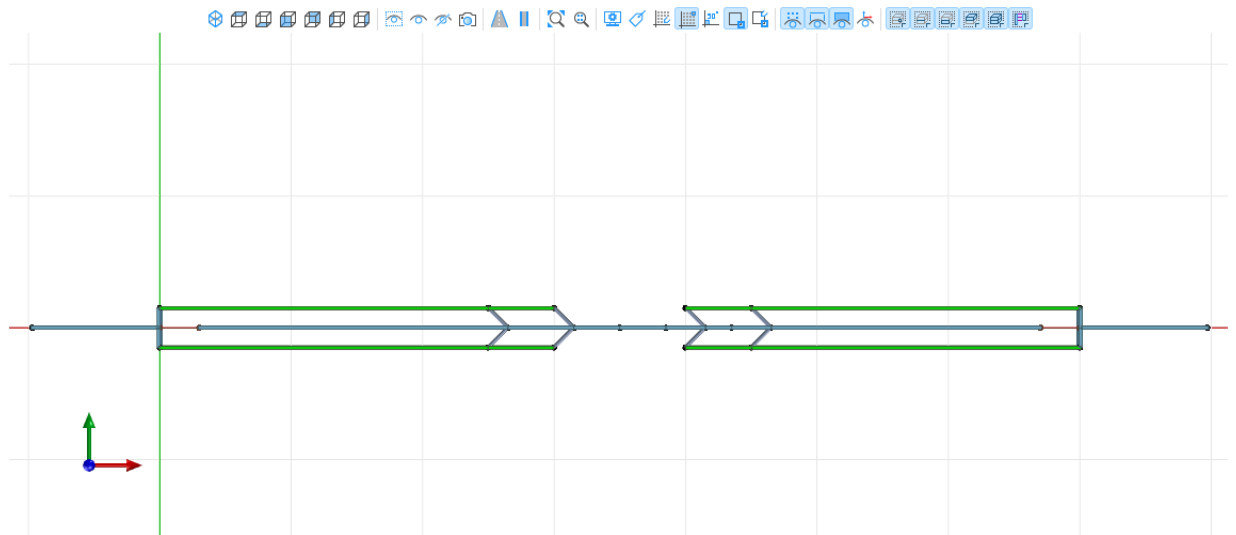


Figure 4.1: Tristable element

Once the tristable brace element is completed, the following step is the construction of the steel portal frame with the following dimensions:

- $H = 4\text{m}$
- $L = 8\text{m}$

Once this step is also completed, it is possible to proceed with the integration of the tristable brace element within the steel portal frame, as depicted in [Figure 1.6](#).

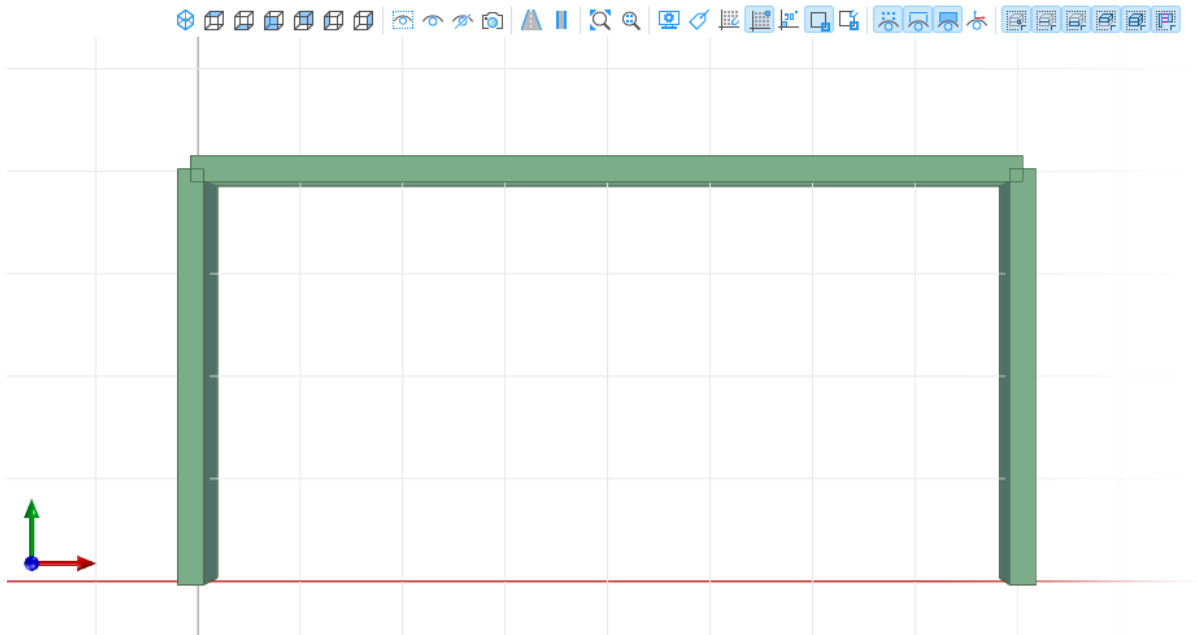


Figure 4.2: Steel portal frame

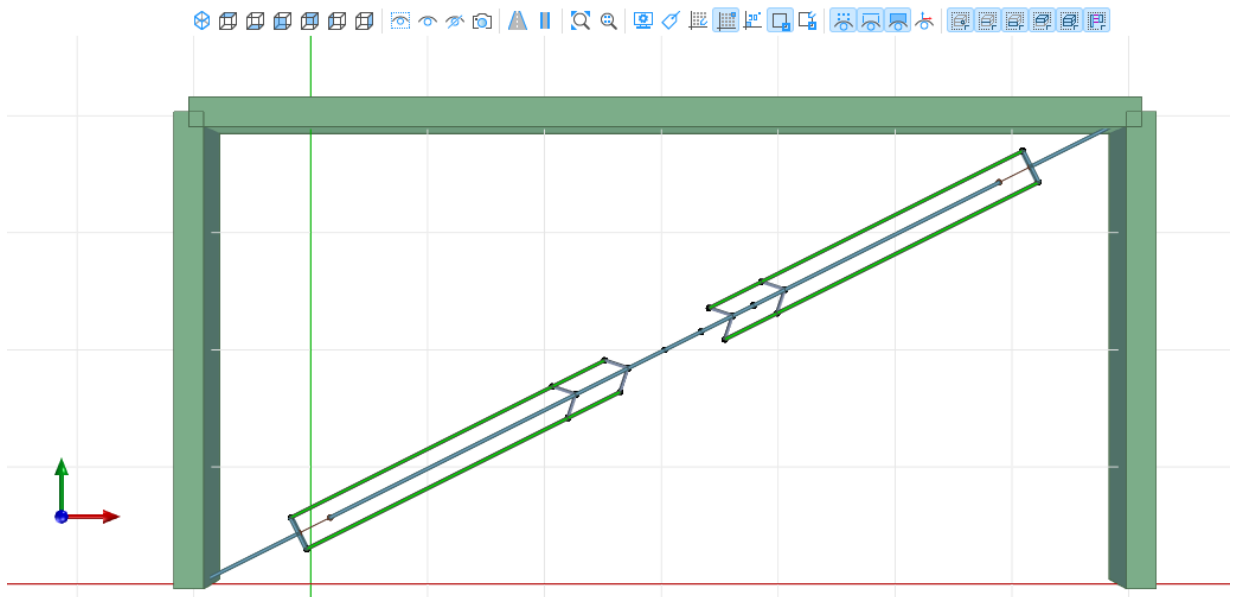


Figure 4.3: Steel portal frame with the tristable brace element

4.2 Selection and scaling of GROUND MOTION

After a sinusoidal time-series has been used in Chapter 3.2 for the study of the bistable element, this section utilizes a real accelerogram, specifically that of Calitri, which is presented below.

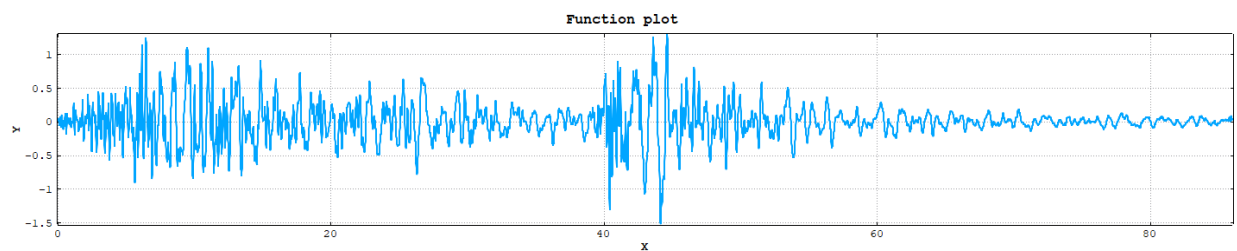


Figure 4.4: Accelerogram from Calitri

4.3 Time-history analysis and response

Time-history analysis is a dynamic analysis method used to study the response of a structure under the influence of time-varying loads, such as an earthquake. In this analysis, the ground motion is applied as a series of data points over time, and the structural response is evaluated at each time step. This method provides a more detailed understanding of the structure's behaviour during transient events like earthquakes.

Once the Ground Motion is selected, it is possible to proceed with the time-history analysis.

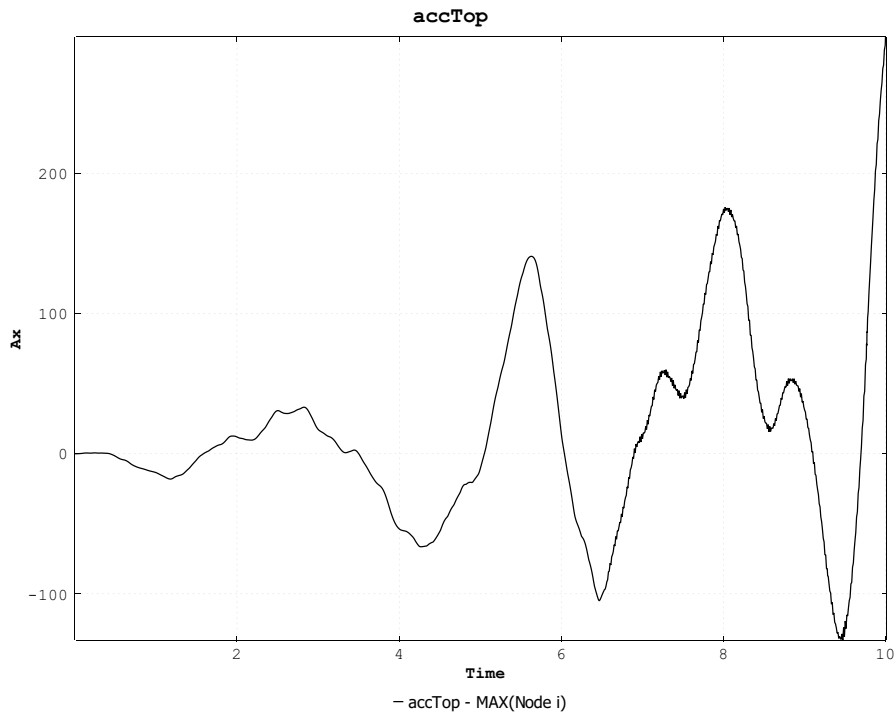
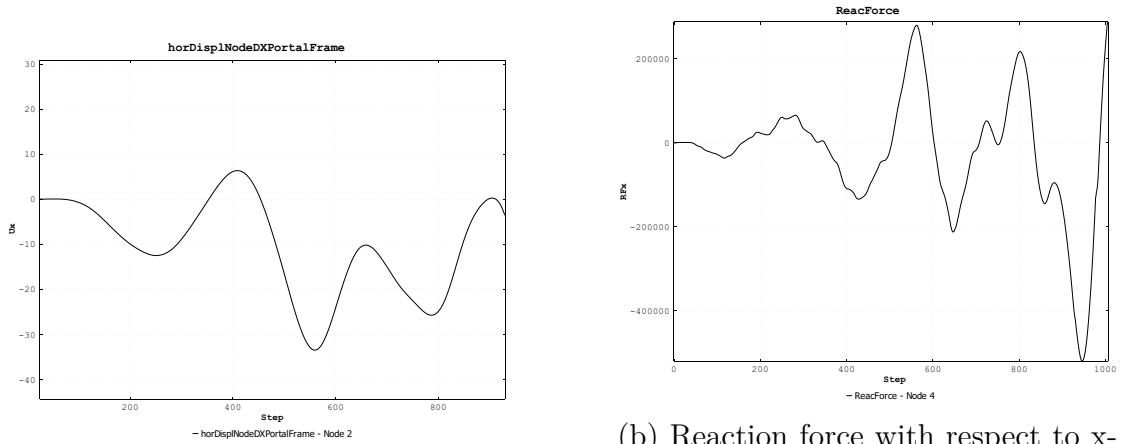


Figure 4.5: Top nodes acceleration



(a) Horizontal displacement of portal frame's upper-right node

(b) Reaction force with respect to x-direction in portal frame's bottom-left node

Figure 4.7: Results

4.3. TIME-HISTORY ANALYSIS AND RESPONSE

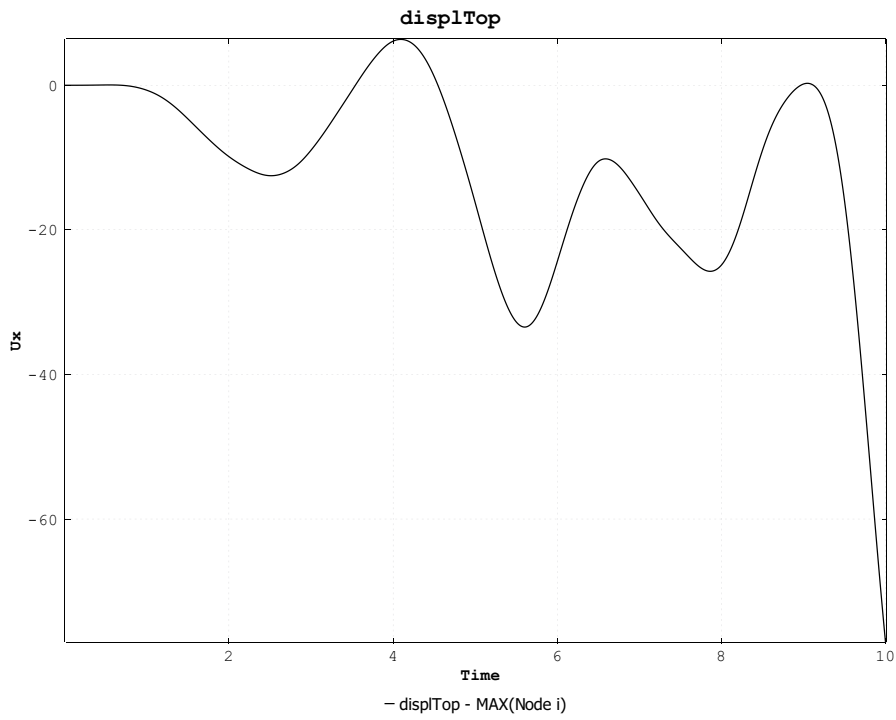
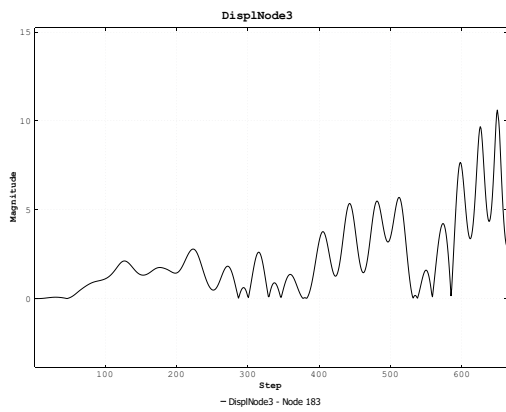
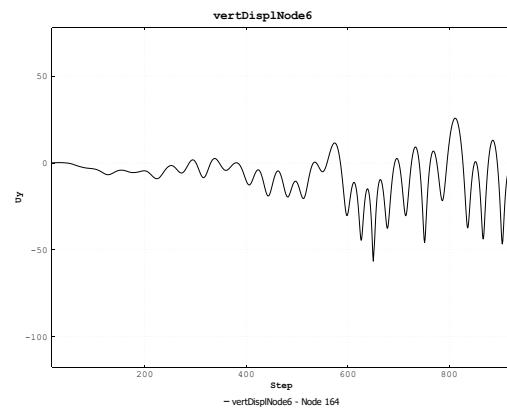


Figure 4.6: Top nodes displacement



(a) Horizontal displacement of node 3



(b) Vertical displacement of node 6

Figure 4.8: Results

4.4 Conclusions

Before drawing conclusions, it is advisable to analyse the results obtained by considering the steel portal frame without the tristable brace element. This step is essential to understand the influence of the tristable brace element on the overall performance of the structure. By comparing the results with and without the brace element, it becomes possible to evaluate the specific contribution of the brace in terms of stability, stiffness, and overall seismic performance.

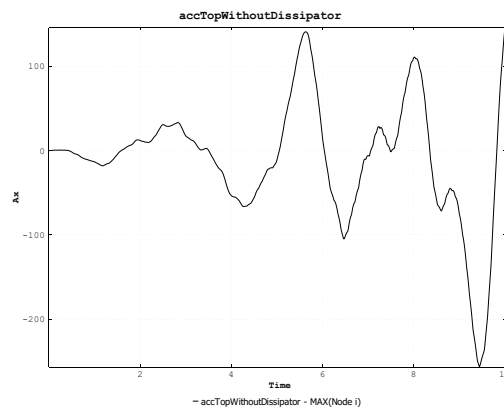


Figure 4.9: Top nodes acceleration without tristable brace

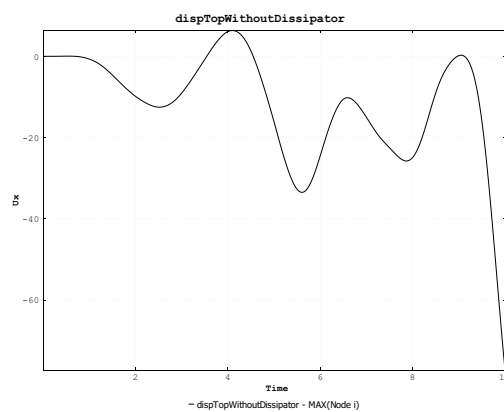
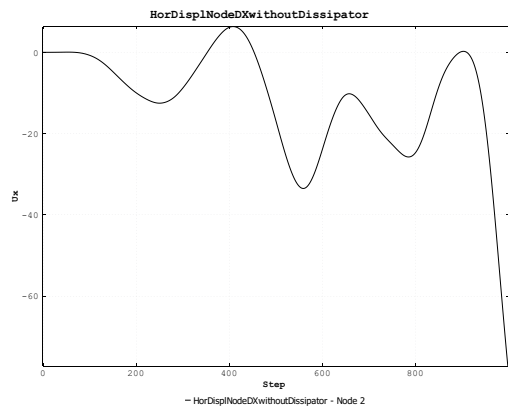
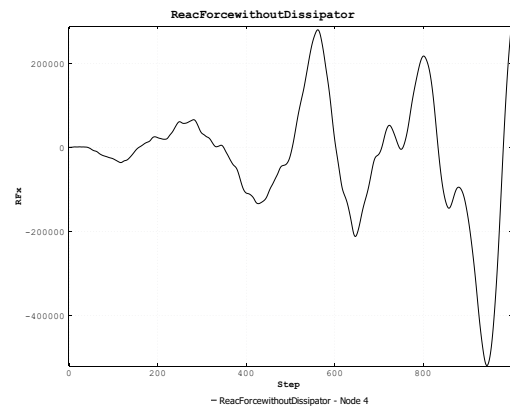


Figure 4.10: Top nodes displacement without tristable brace

4.4. CONCLUSIONS



(a) Horizontal displacement of portal frame's upper-right node without tristable brace



(b) Reaction force with respect to x-direction in portal frame's bottom-left node without tristable brace

Figure 4.11: Results

Chapter 5

Conclusions

This investigation definitively establishes the considerable potential of energy dissipation devices, specifically those leveraging bistable and tristable mechanics, in enhancing the seismic resistance of structural frameworks. The deployment of the tristable brace within a steel portal frame demonstrably yielded reduced acceleration at the top nodes and a pronounced decrease in displacement at the upper-right corner. These favourable outcomes provide strong evidence supporting the superior performance of the tristable arrangement, showcasing its ability not only to effectively absorb seismic energy but also to moderate the dynamic effects that contribute to structural degradation.

Through parametric analyses detailed in preceding sections, the ideal design parameters for both the bistable and, subsequently, the tristable components have been successfully defined. The reduction in acceleration and displacement observed throughout the experimental simulations underscores the viability of this innovative brace design as a superior alternative to conventional bracing methods in areas prone to seismic activity.

While the outcomes are encouraging, the research also pinpoints areas ripe for further development. One prominent direction for future study is the integration of enhanced damping features. By incorporating extra damping elements – whether through upgraded viscous dampers or alternate dissipators – the stress experienced by key structural members could be further mitigated. Such enhancements would not only improve energy absorption efficiency but also potentially prolong the lifespan and increase the resilience

of the structure.

In essence, this investigation validates the practical application of multi-stable energy dissipation devices within the domain of seismic protection. The significant gains in dynamic performance associated with the tristable brace, combined with opportunities for enhanced stress reduction through supplemental damping technologies, create a compelling foundation for ongoing research initiatives. Further explorations along these lines could culminate in the creation of more durable, efficient, and resilient seismic protection systems, capable of effectively addressing the changing requirements of structural engineering practice.

Bibliography

- [1] EG Karpov, Didem Ozevin, M Mahamid, and LA Danso. «On the comprehensive stability analysis of axially loaded bistable and tristable metastructures». In: *International Journal of Solids and Structures* 199 (2020), pp. 158–168.
- [2] Larry A Danso and Eduard G Karpov. «Cusp singularity-based bistability criterion for geometrically nonlinear structures». In: *Extreme Mechanics Letters* 13 (2017), pp. 135–140.
- [3] Ahmad Rafsanjani, Abdolhamid Akbarzadeh, and Damiano Pasini. «Snapping mechanical metamaterials under tension». In: *arXiv preprint arXiv:1612.05987* (2016).
- [4] Eduard G Karpov, Larry A Danso, and John T Klein. «Negative extensibility metamaterials: Occurrence and design-space topology». In: *Physical Review E* 96.2 (2017), p. 023002.
- [5] John T Klein and Eduard G Karpov. «Negative extensibility metamaterials: phase diagram calculation». In: *Computational Mechanics* 62 (2018), pp. 669–683.
- [6] John T Klein and Eduard G Karpov. «Bistability in thermomechanical metamaterials structured as three-dimensional composite tetrahedra». In: *Extreme Mechanics Letters* 29 (2019), p. 100459.
- [7] SH Strogatz. «Nonlinear dynamics and chaos Addison-Wesley». In: *Reading, MA* (1994).
- [8] Yi-Ze Wang, Feng-Ming Li, Wen-Hu Huang, Xiaoai Jiang, Yue-Sheng Wang, and Kikuo Kishimoto. «Wave band gaps in two-dimensional piezoelectric/piezomagnetic phononic crystals». In: *International Journal of Solids and Structures* 45.14-15 (2008), pp. 4203–4210.
- [9] Peter Timothy Saunders. *An introduction to catastrophe theory*. Cambridge University Press, 1980.

- [10] Ryan L Harne and Kon-Well Wang. *Harnessing bistable structural dynamics: for vibration control, energy harvesting and sensing*. John Wiley & Sons, 2017.
- [11] Chang-Yull Lee, Jin-Young Jung, and Se-Min Jeong. «Active vibration suppression of stiffened composite panels with piezoelectric materials under blast loads». In: *Applied Sciences* 10.1 (2020), p. 387.
- [12] Hao Deng, Lin Cheng, Xuan Liang, Devlin Hayduke, and Albert C To. «Topology optimization for energy dissipation design of lattice structures through snap-through behavior». In: *Computer Methods in Applied Mechanics and Engineering* 358 (2020), p. 112641.
- [13] Yun-Che Wang and Roderic Lakes. «Negative stiffness-induced extreme viscoelastic mechanical properties: stability and dynamics». In: *Philosophical Magazine* 84.35 (2004), pp. 3785–3801.
- [14] Zachary G Nicolaou, Feng Jiang, and Adilson E Motter. «Metamaterials with negative compressibility highlight evolving interpretations and opportunities». In: *Nature communications* 15.1 (2024), p. 8573.
- [15] Tobias Frenzel, Claudio Findeisen, Muamer Kadic, Peter Gumbsch, and Martin Wegener. «Tailored Buckling Microlattices as Reusable Light-Weight Shock Absorbers.» In: *Advanced materials (Deerfield Beach, Fla.)* 28.28 (2016), pp. 5865–5870.
- [16] Sicong Shan, Sung H Kang, Jordan R Raney, Pai Wang, Lichen Fang, Francisco Candido, Jennifer A Lewis, and Katia Bertoldi. «Multistable architected materials for trapping elastic strain energy». In: *Adv. Mater* 27.29 (2015), pp. 4296–4301.
- [17] Bastiaan Florijn, Corentin Coulais, and Martin van Hecke. «Programmable mechanical metamaterials». In: *Physical review letters* 113.17 (2014), p. 175503.
- [18] Kai A James and Haim Waisman. «Layout design of a bi-stable cardiovascular stent using topology optimization». In: *Computer Methods in Applied Mechanics and Engineering* 305 (2016), pp. 869–890.
- [19] Konstantin Kappe, Jan P Wahl, Florian Gutmann, Silviya M Boyadzhieva, Klaus Hoschke, and Sarah CL Fischer. «Design and manufacturing of a metal-based mechanical metamaterial with tunable damping properties». In: *Materials* 15.16 (2022), p. 5644.
- [20] Igor V Belykh, Russell Jeter, and Vladimir N Belykh. «Bistable gaits and wobbling induced by pedestrian-bridge interactions». In: *Chaos: An Interdisciplinary Journal of Nonlinear Science* 26.11 (2016).

- [21] Sen Yan, Lingling Wu, Yongzheng Wen, Jingbo Sun, and Ji Zhou. «Snap-through instability in mechanical metamaterials». In: *Responsive Materials* (2025), e20240035.
- [22] Qionsong Wang, Qiang Bao, Zixing Lu, Zhenyu Yang, et al. «A bistable mechanical metamaterial based on snap-through mechanism». In: *Zixing and Yang, Zhenyu, A Bistable Mechanical Metamaterial Based on Snap-Through Mechanism* ().
- [23] Tugberk Guner, Oreste S Bursi, and Silvano Erlicher. «Optimization and performance of metafoundations for seismic isolation of small modular reactors». In: *Computer-Aided Civil and Infrastructure Engineering* 38.12 (2023), pp. 1558–1582.
- [24] N Menga, F Bottiglione, and G Carbone. «Nonlinear viscoelastic isolation for seismic vibration mitigation». In: *Mechanical Systems and Signal Processing* 157 (2021), p. 107626.
- [25] Soheila Sadeghi Eshkevari, Soheil Sadeghi Eshkevari, Debarshi Sen, and Shamim N Pakzad. «RL-Controller: a reinforcement learning framework for active structural control». In: *arXiv preprint arXiv:2103.07616* (2021).
- [26] Pei-Ching Chen and Kai-Yi Chien. «Machine-learning based optimal seismic control of structure with active mass damper». In: *Applied Sciences* 10.15 (2020), p. 5342.